الجـــمـــهـــوريـــــة الجـــزائـــريـــة الديـــمـــقـــراطـــيـــة الـــشـــعـــبـــيـــة

PEOPLE'S DEMOCRATIC REPUBLIC OF ALGERIA

وزارة التـــعـــلـــيـــم العــــــالي والبــــحـــث العـــــلــــمــــي

MINISTRY OF HIGHER EDUCATION AND SCIENTIFIC RESEARCH

جـــــــــــــامعة سعيدة – د. الطاهر مولاي –

University of Saida - Dr. MOULAY TAHAR
Faculty of Mathematics, Computing and Telecommunications

A Dissertation Submitted to the Department of Telecommunications in Partial Fulfilment of the Requirements for Degree of Master of Systems of Telecommunications

Presented by:
Miss. DEGDOUG Amel Ferdous & DOUALI Afia

High-Performance MIMO Slot Microstrip Antenna for Terahertz Applications: Design and Optimization

Defended on June 14, 2026, in front of the jury composed of:

Mr. DAMOU Mehdi	Pr.	President
Miss. NOURI Keltouma	Pr.	Supervisor
Mr. BOUBAKER.H	Dr.	Examiner
BECHAREF Kada	Dr.	Co-Supervisor

2025 / 2026

Acknowledgments

First and foremost, we express our deepest gratitude to God, the Almighty, for granting us the strength, patience, and perseverance to overcome every difficulty encountered throughout this journey. Without His guidance, this work would not have been possible.

We would like to convey our sincere and heartfelt appreciation to our supervisor, **Professor NOURI Keltouma**, for her unwavering support, precious guidance, and constant encouragement. Her dedication, kindness, and commitment have been a true source of inspiration, and her valuable advice has profoundly shaped this work.

Our warmest thanks also go to our co-supervisor **Dr. BECHAREF Kada**, whose support, thoughtful suggestions, and encouragement greatly contributed to improving the quality of this project. His involvement has been sincerely appreciated.

We are deeply grateful to **Dr. SAIDI Amaria** for her continuous encouragement, generosity, and readiness to help. Her support meant a great deal to us throughout the realization of this work.

It is a great honor for us to express our sincere gratitude to **Pr. DAMOU Mehdi** for accepting to chair the jury of our defense. His presence represents a privilege that we truly value.

We would also like to extend our heartfelt thanks to **Dr. BOUBAKER Hichem** for kindly agreeing to examine this work. We are very grateful for his time, consideration, and valuable remarks.

We extend our sincere thanks to **Pr. CHETIOUI Mohammed** for his kind availability and for providing valuable insights that helped clarify key details in our work.

Finally, we would like to express our sincere appreciation to all the professors of the Telecommunications Department at Dr. Moulay Tahar University of Saida. Their dedication, passion for teaching, and the knowledge they have shared with us have been a cornerstone of our academic journey and a source of lasting inspiration.

We also extend our gratitude to everyone who supported us, directly or indirectly, in achieving this work.

Thank you from the bottom of our hearts.

Dedication

*To my father, **ABD Kader**, whose sacrifices, strength, and belief in me have supported all that I have achieved.*

*To my mother, **DEGDOUG Aicha,** whose love, prayers, and tenderness have carried me through every difficulty.*

*To my sister, **Assia**, for her support, encouragement, and the light she brings into my life. To my brothers **Hocine and Nouh,** whose presence and strength have given me confidence and courage.*

I dedicate this work to you with all my love, respect, and gratitude.

DEGDOUG AMEL FERDOUS

*To my dear father **ABDELKARIM**, whose support, sacrifices, and strength have been my foundation throughout every stage of my life.*

*To my beloved mother **Douali Attaouia**, who has always been a symbol of unconditional love, care, patience, and endless prayers.*

*To my sisters **Fouzia, Houaria, Khadidja, and Hayet**, for their love, encouragement, and constant support.*

*To my brothers **Mohamed and Yasser,** for their guidance, confidence, and continuous encouragement.*

To the sons and daughters of my brothers, who bring joy, happiness, and warmth to our family.

I dedicate this work to all of you with love, gratitude, and deep appreciation.

Douali Afia

What felt like a mountain is now just a step on the journey

Abstract

This final-year project focuses on the design, simulation, and optimization of microstrip patch antennas operating in the terahertz (THz) frequency band (0.1–0.95 THz) for future 6G wireless communication applications, with a target resonance frequency around 0.3 THz.

The proposed antenna is designed and simulated on a polyimide substrate using Electroless Nickel Immersion Gold (ENIG) as a cost-effective alternative to pure gold. A 2×2 MIMO antenna configuration is implemented to improve radiation performance, particularly gain and reflection coefficient (S_{11}), while enhancing data transmission speed and link reliability. Several antenna configurations were modeled, analyzed, and manually optimized using ANSYS HFSS through the introduction of slots and geometrical modifications to improve bandwidth, and radiation characteristics. Furthermore, Machine Learning-based optimization techniques were applied to automatically optimize the antenna design parameters and enhance the overall performance of the 2×2 MIMO antenna system. The obtained results demonstrate that the optimized antenna achieves good performance within the THz band, especially near the resonance frequency of 0.3 THz, making it a suitable candidate for high-data-rate 6G wireless communication systems.

Keywords: Terahertz (THz), microstrip Patch Antenna, MIMO, 6G Communications, machine Learning, optimization, ANSYS HFSS, ENIG, gain, bandwidth, return Loss, isolation, resonance Frequency.

Résumé

Ce projet de fin d'études porte sur la conception, la simulation et l'optimisation d'antennes patch micro-ruban fonctionnant dans la bande de fréquences térahertz (THz) (0,1–0,95 THz) pour les futures applications des communications sans fil 6G, avec une fréquence de résonance cible autour de 0,3 THz.

L'antenne proposée a été conçue et simulée sur un substrat de polyimide en utilisant l'ENIG (dépôt autocatalytique de nickel sous immersion d'or**)** comme alternative économique à l'or pur.Une configuration d'antenne MIMO 2×2 est mise en œuvre afin d'améliorer les performances de rayonnement, notamment le gain et le coefficient de réflexion (S_{11}), tout en augmentant la vitesse de transmission des données et la fiabilité de la liaison. Plusieurs configurations d’antennes ont été modélisées, analysées et optimisées manuellement à l’aide du logiciel ANSYS HFSS grâce à l’introduction de fentes et de modifications géométriques afin d’améliorer l’adaptation d’impédance, la bande passante et les caractéristiques de rayonnement. En outre, des techniques d’optimisation basées sur l’apprentissage automatique (Machine Learning) ont été appliquées afin d’optimiser automatiquement les paramètres de conception de l’antenne et d’améliorer les performances globales du système d’antenne MIMO 2×2. Les résultats obtenus démontrent que l’antenne optimisée présente de bonnes performances dans la bande THz, en particulier autour de la fréquence de résonance de 0,3 THz, ce qui en fait une candidate appropriée pour les systèmes de communication sans fil 6G à très haut débit.

Mots-clés : Térahertz (THz), antenne patch micro-ruban, MIMO, communications 6G, apprentissage automatique, optimisation, ANSYS HFSS, ENIG, gain, bande passante, perte de retour, isolation, fréquence de résonance.

ملخص

ركز مشروع التخرج هذا على تصميم ومحاكاة وتحسين هوائيات الرقعة الميكروية العاملة في نطاق التيراهرتز (THz) (0.1–0.95 تيراهرتز) من أجل تطبيقات الاتصالات اللاسلكية المستقبلية للجيل السادس(6G) ، مع استهداف تردد رنين يقارب0.3تيراهرتز.

تم تصميم ومحاكاة الهوائي الهوائي المقترح على ركيزة من مادة البوليمايد باستخدام مادة الذهب بالغمر الكيميائي بالنيكل (ENIG)كبديل اقتصادي للذهب النقي. كما تم اعتماد بنية هوائي MIMO 2×2 لتحسين أداء الإشعاع، خاصة الكسب ومعامل الانعكاس(S_{11}) ، مع تعزيز سرعة نقل البيانات وموثوقية الاتصال. تم تصميم وتحليل وتحسين عدة تكوينات للهوائيات يدويًا باستخدام برنامج ANSYS HFSS من خلال إدخال فتحات وتعديلات هندسية بهدف تحسين معامل الانعكاس وعرض الحزمة وخصائص الإشعاع. بالإضافة إلى ذلك، تم تطبيق تقنيات تحسين معتمدة على التعلم الآلي (Machine Learning) لتحسين معاملات تصميم الهوائي تلقائيًا وتعزيز الأداء العام لنظام هوائي MIMO 2×2. أظهرت النتائج المتحصل عليها أن الهوائي المحسن يحقق أداءً جيدًا ضمن نطاق التيراهرتز، وخاصة بالقرب من تردد الرنين0.3تيراهرتز، مما يجعله مرشحًا مناسبًا لأنظمة الاتصالات اللاسلكية 6 Gذات معدلات نقل البيانات العالية جدًا.

الكلمات المفتاحية: التيراهرتز(THz) ، هوائي الرقعة الميكروية، MIMO، اتصالات الجيل السادس6G، التعلم الآلي، التحسين، ANSYS HFSS، ENIG، الكسب، عرض الحزمة، فقدان العودة، العزل، تردد الرنين.

Table of contents

Chapter II: Advanced Antenna Architectures and Terahertz Technologies

Chapter III: Machine Learning in THz Patch Antenna Design

Chapter IV: Design, Simulation and Optimization

List of Figures

List of Tables

List of Abbreviation

5G	Fifth Generation Wireless Networks
6G	Sixth Generation Wireless Networks
AI	Artificial Intelligence
AM	Amplitude Modulation
ANN	Artificial Neural Network
ANSYS HFSS	Analysis of Systems High-Frequency Structure Simulator
Au	Gold (Metallization Layer)
BE	Beam Efficiency
BW	Bandwidth
BWFN	Beam Width First Null
CatBoost	Categorical Boosting
CCL	Channel Capacity Loss
Cu	Copper (Primary Conductor)
dB	Decibel
DC	Direct Current
DG	Diversity Gain
DGS	Defected Ground Structure
DL	Deep Learning
DUT	Device Under Test
ECC	Envelope Correlation Coefficient
EM	Electromagnetic
ENIG	Electroless Nickel Immersion Gold
ET	Extra Trees
EVS	Explained Variance Score
FM	Frequency Modulation

FNBW	First-Null Beamwidth
FSS	Frequency Selective Surface
GHz	Gigahertz
GPR	Gaussian Process Regression
GPS	Global Positioning System
HPBW	Half-Power Beamwidth
IEEE	Institute of Electrical and Electronics Engineers
IoT	Internet of Things
KHz	Kilohertz
KNN	K-Nearest Neighbors
LTE	Long-Term Evolution
MAE	Mean Absolute Error
MC	Mutual Coupling
MEG	Mean Effective Gain
MIMO	Multiple-Input Multiple-Output
ML	Machine Learning
mm-Wave	Millimeter Wave
MSE	Mean Squared Error
Ni	Nickel (Diffusion Barrier)
PCB	Printed Circuit Board
PDS	Parasitic Decoupling Structure
PFE	Projet de Fin d'Études (Graduation Project)
PIFA	Planar Inverted-F Antenna
R^2	Coefficient of Determination (R-Squared)
RF	Radio Frequency / Random Forest
RFID	Radio Frequency Identification

RL	Return Loss
RMSE	Root Mean Square Error
S-parameters	Scattering Parameters (S_{11}, S_{12}, S_{21}, S_{22})
Sr	Steradian (Solid Angle Unit)
sub-THz	Sub-Terahertz spectrum
TARC	Total Active Reflection Coefficient
THz	Terahertz
UMTS	Universal Mobile Telecommunications System
VNA	Vector Network Analyzer
VSWR	Voltage Standing Wave Ratio
WiMax	Worldwide Interoperability for Microwave Access
XGBoost	Extreme Gradient Boosting

General Introduction

The continuous growth of wireless communication systems and the exponential increase in data traffic have created an urgent need for innovative technologies capable of meeting the stringent requirements of next-generation networks. Applications such as ultra-high-definition video streaming, virtual and augmented reality, autonomous systems, the Internet of Things (IoT) demand extremely high data rates, ultra-low latency, and enhanced reliability. In this context, current microwave and millimeter-wave frequency bands are becoming increasingly congested, motivating the exploration of new spectral regions, particularly the terahertz (THz) band, typically ranging from 0.1 THz to 10 THz **[1]**- **[2]**.

The THz spectrum has emerged as a key enabler for beyond-5G and sixth generation (6G) wireless communication systems due to its ability to provide ultra-wide bandwidths **[1]**. However, despite its promising potential, THz communication faces several critical challenges, including severe free-space path loss, atmospheric absorption, hardware limitations, and sensitivity to environmental conditions **[2]**. These challenges necessitate the development of highly efficient and optimized antenna systems capable of operating effectively at such high frequencies.

Antennas are essential components in any wireless communication system, acting as the interface between guided and radiated electromagnetic waves. Among the various antenna technologies, microstrip patch antennas have been widely adopted due to their compact size, low profile, lightweight structure, ease of fabrication, and compatibility with modern integrated circuits **[3]**-**[4]**. Nevertheless, at THz frequencies, conventional antenna design techniques encounter significant limitations related to material properties, fabrication tolerances, and electromagnetic behavior, which require advanced modeling and optimization approaches.

To overcome these limitations and improve system performance, advanced antenna architectures such as Multiple-Input Multiple-Output (MIMO) systems have been extensively investigated. MIMO technology exploits spatial diversity and multiplexing techniques to significantly enhance channel capacity, spectral efficiency, and link reliability without increasing transmission power or bandwidth **[5]**. The integration of MIMO with THz communication systems represent a promising solution for achieving ultra-high data rates and robust communication links in future wireless networks **[6]**.

In addition to architectural advancements, the application of artificial intelligence and machine learning techniques has recently gained considerable attention in the field of antenna design and optimization. Traditional design approaches often rely on iterative parametric sweeps and numerical optimization methods, which are computationally intensive and time-consuming, particularly for complex structures operating at THz frequencies. Machine learning algorithms, such as regression models, neural networks, and optimization heuristics, provide powerful tools for modeling nonlinear relationships between antenna parameters and performance metrics, enabling faster convergence and improved design efficiency **[7]**.

In this work, the focus is placed on the design and optimization of THz microstrip patch antennas integrated within MIMO systems. Special emphasis is given to the use of machine learning algorithms to enhance antenna performance in terms of gain, bandwidth, return loss, and radiation efficiency. Furthermore, full-wave electromagnetic simulations are carried out using ANSYS HFSS, a widely recognized tool for high-frequency structure analysis, to validate the proposed designs and evaluate their performance under realistic conditions.

Outline of this work

The outline of this thesis is summarized as follows:

Chapter 1: Antenna Theory and Fundamental Concepts

This chapter establishes the theoretical foundation for antenna analysis and design. It covers electromagnetic radiation principles, antenna field regions (reactive near-field, Fresnel, and Fraunhofer zones), and essential performance parameters including radiation patterns, directivity, gain, efficiency, bandwidth, and polarization. These fundamentals provide the necessary basis for understanding microstrip patch antenna operation at terahertz frequencies.

Chapter 2: Advanced Antenna Architectures and MIMO and Terahertz Technologies

This chapter presents planar antenna configurations with emphasis on microstrip patch antennas, their feeding techniques, and design trade-offs. Advanced systems including smart antennas, metamaterial-integrated structures, phased arrays, and reconfigurable antennas are discussed. MIMO technology spatial multiplexing, diversity techniques, and key performance metrics is covered. Finally, Terahertz technology is introduced as a critical enabler for 6G networks, addressing spectral characteristics, propagation challenges, and THz antenna design requirements.

Chapter 3: Machine Learning in THz Patch Antenna Design

This chapter addresses computational challenges in conventional antenna design and presents machine learning as an efficient optimization approach. It surveys supervised learning algorithms including Random Forest, Extra Trees, XGBoost, CatBoost, KNN, and Gaussian

Process Regression for THz antenna applications. The focus is on surrogate modeling to replace time-intensive full-wave simulations, enabling rapid performance prediction and design optimization for 6G microstrip patch antennas.

Chapter 4: Design, Simulation and Optimization

This chapter focuses on antenna simulation, modeling, and performance validation using ANSYS HFSS. It presents the design and optimization of THz microstrip patch antennas and 2×2 MIMO configurations, validating predicted results from machine learning algorithms through full-wave electromagnetic simulations.

Bibliography of general introduction

[1]. T. S. Rappaport, Y. Xing, G. R. MacCartney Jr., A. F. Molisch, E. Mellios, and J. Zhang, "Wireless communications and applications above 100 GHz: Opportunities and challenges for 6G and beyond," *IEEE Access*, vol. 7, pp. 78729–78757, 2019.

[2]. I. F. Akyildiz, J. M. Jornet, and C. Han, "Terahertz band: Next frontier for wireless communications," *Physical Communication*, vol. 12, pp. 16–32, ISSN: 1874-4907, Sept. 2014.

[3]. C. A. Balanis, Antenna Theory: Analysis and Design, *4th ed. Hoboken, NJ, USA: Wiley*, 2016, ISBN: 978-1-118-64206-1.

[4]. D. M. Pozar, Microwave Engineering, *4th ed. Hoboken, NJ, USA: Wiley,* ISBN: 978-0-470-63155-3, 2012.

[5]. S. Sun, T. S. Rappaport, R. W. Heath Jr., A. Nix, and S. Rangan, "MIMO for millimeter-wave wireless communications: Beamforming, spatial multiplexing, or both?" *IEEE Communications Magazine*, vol. 52, no. 12, pp. 110–121, ISSN: 0163-6804, Dec. 2014.

[6]. K. Huang and Z. Wang, "Terahertz terabit wireless communication," *IEEE Microwave Magazine*, vol. 12, no. 4, pp. 108–116, ISSN: 1527-334, Jun. 2011.

[7]. S. Haykin, "Neural Networks and Learning Machines", *3rd ed. New York, NY, USA*: Pearson, ISBN: 978-0-13-147139-9, 2009.

Problem Statement

The design of compact microstrip patch antennas for 6G applications is challenged by three fundamental issues: high computational cost, increased design complexity, and limited real-time capability when using conventional optimization methods. Classical optimization algorithms rely on extensive full-wave electromagnetic simulations, rendering the design process time-consuming and inefficient for highly nonlinear and multi-dimensional problems. Additionally, 6G communication will rely heavily on MIMO antenna systems, where multiple antenna elements must be carefully arranged to ensure low mutual coupling, high isolation, and stable radiation performance, further increasing design complexity. These limitations highlight the necessity for intelligent and predictive optimization approaches capable of reducing simulation effort, improving accuracy, and enabling rapid optimization of miniaturized antennas and MIMO configurations for future 6G wireless systems.

Objectives

The primary objective of this final-year project is to select the most suitable antenna and MIMO topology by developing an efficient methodology for predicting and optimizing compact microstrip patch antenna parameters. This is achieved by integrating classical and modern optimization algorithms with Machine Learning techniques for 6G wireless applications. The work analyzes 6G requirements, including frequencies above 100 GHz, massive connectivity, and ultra-low latency, and their impact on antenna design. It focuses on the design and miniaturization of microstrip patch antennas for compact devices, addressing the trade-off between size and performance. Optimization is carried out using Machine Learning (ML)-based optimization techniques, including Random Forest, XGBoost, and CatBoost. These algorithms are employed to model and optimize antenna performance parameters efficiently. Additionally, Artificial Neural Networks (ANNs) are developed to rapidly predict key performance metrics such as return loss, bandwidth, gain, and radiation efficiency, thereby reducing dependence on computationally expensive full-wave simulations. Finally, a comparative analysis between different ML optimization algorithms and ANN-based predictive models is conducted to propose an efficient and robust hybrid design methodology. Validated using Ansys HFSS simulations.

Chapter I: Antenna Theory and Fundamental Concepts

I.1. Introduction

This chapter provides a detailed overview of the fundamental principles of antenna theory required for the analysis and design of modern antenna systems. It describes the antenna radiation mechanism and explains the different electromagnetic field regions, including the near-field and far-field zones. Furthermore, the chapter introduces the main performance parameters used to characterize antenna behavior, such as radiation pattern, gain, directivity, bandwidth, and polarization. These theoretical concepts establish a solid foundation for understanding antenna performance and serve as the basis for the design, prediction, and optimization of compact microstrip patch antennas presented in the subsequent chapters.

I.2. Overview of the History of Communications

Communication systems have evolved significantly over time, from primitive methods to modern wireless technologies. In pre-modern civilization, communication relied on simple techniques such as smoke signals, flags (optical), and drums (acoustic), which were early forms of long-distance signaling. The era of electronic communication began in 1844 with the invention of the telegraph by Samuel Morse, introducing digital communication through Morse code **[1]**.

In 1864, James Clerk Maxwell established the theoretical foundation of electromagnetic waves through Maxwell's equations. This was followed by the first successful transatlantic telegraph cable in 1866**,** enabling long-distance wired communication. The invention of the telephone in 1876 by Alexander Graham Bell marked the beginning of analog communication over long distances **[1]**.

Wireless communication emerged with the first antenna in 1887**,** demonstrated by Heinrich Hertz, and the first practical radio system in 1897 by Guglielmo Marconi. Marconi later achieved the first transatlantic radio transmission in 1901**.** By1920, the first broadcast radio station was established **[1]**.

During World War II, major advancements in radar and antenna technologies (such as horn and array antennas) were developed. In the 1950s**,** television broadcasting became widespread. The 1960**s** saw the rise of satellite communications and optical fiber systems. Finally, in the 1980s, wireless communication expanded rapidly with the introduction of cellular networks **[1]**.

Pre-modern civilization (up to 2 million years ago)	
	Optical communications: Smoke signals, flags
	Acoustical communications: Drums
1844	Telegraph—The beginning of electronic communication *Samuel Morse*
1864	Maxwell's equations—Principles of radio waves and the electromagnetic spectrum *James Clerk Maxwell*
1866	First lasting transatlantic telegraph cable
1876	Telephone—Wireline analog communication over long distance *Alexander Bell*
1887	First Antenna *Heinrich Hertz*
1897	First practical wireless (radio) systems *Guglielmo Marconi*
1901	First transatlantic radio *Guglielmo Marconi*
1920	First broadcast radio station
World War II	Development of radar; horn, reflector, and array antennas
1950s	Broadcast television in wide use
1960s	Satellite communications and fiber optics
1980s	Wireless reinvented with widespread use of cellular telephones

Electromagnetics Pioneer — Antenna Pioneer — Wireless Pioneer

James Clerk Maxwell — *Heinrich Hertz* — *Guglielmo Marconi*

Table I.1: Timeline of significant events in the history of antennas and communications **[1].**

I.3. What is an antenna and what is it used?

I.3.1. What is an antenna?

An antenna is defined by Webster 's Dictionary as -a usually metallic device (as a rod or wire) for radiating or receiving radio waves. The IEEE Standard Definitions of Terms for Antennas (IEEE Std 145–1983) defines the antenna or aerial as -a means for radiating or receiving radio waves **[2].** In other words, the antenna is the transitional structure between free-space and a guiding device. The guiding device or transmission line may take the form of a coaxial line or a hollow pipe (waveguide), and it is used to transport electromagnetic energy from the transmitting source to the antenna or from the antenna to the receiver. In the former case, we have a transmitting antenna and in the latter a receiving antenna (see **Figure. I.1**) **[3].**

This dual functionality enables the same antenna structure to operate effectively in both transmission and reception modes, eliminating the need for separate antennas in two-way communication systems as shown in **Figure I.1 [4].**

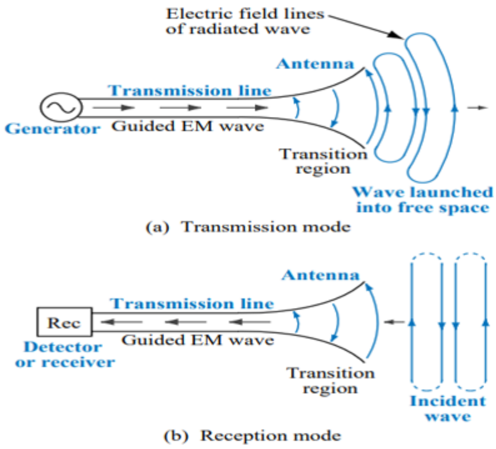

Figure I.1: Antenna as a) Transmission Mode b) Receiving Mode **[5]**.

An antenna is basically a transducer. It converts radio frequency (RF) signal into an electromagnetic (EM) wave of the same frequency. It forms a part of transmitter as well as the receiver circuits **[3].**

Definition of antenna

An antenna can be defined in the following different ways **[6]-[7]:**

1. An antenna may be a piece of conducting material in the form of a wire, rod or any other shape with excitation.

2. An antenna is a source or radiator of electromagnetic waves.

3. An antenna is a sensor of electromagnetic waves.

4. An antenna is a transducer.

5. An antenna is an impedance matching device.

6. An antenna is a coupler between a generator and space or vice versa.

An antenna can also be termed an aerial. The plural form is either antennae or antennas**.**

I.3.2. Need of Antenna

Antennas are essential components in modern wireless communication systems, serving as the critical interface for converting electrical signals into electromagnetic waves and vice versa. Devices such as televisions, radios, cell phones, and satellite systems all depend on antennas to establish wireless connectivity. These antennas vary in design based on operating frequency, specific application requirements, and signal characteristics. The effectiveness of wireless systems is heavily influenced by key antenna parameters including gain, bandwidth, and polarization, making proper antenna design crucial for optimal performance in transmitting and receiving electromagnetic signals **[4].**

I.4. Basic introduction to electromagnetic field:

- **A Wave** can be defined as a motion (such as oscillation) that propagates through matter or free space.
- **An Electric field** exists in the presence of a charged body.
- **A magnetic field** is a force produced by a moving electric charge that exists around a magnet or in free space.
- **Time-varying fields or waves** are usually due to accelerated charges or time-varying current. Time-varying current →Electromagnetic fields (or waves)
- **Electromagnetic (EM) radiation** is an electromagnetic wave that travels away from some source (like antenna, sun, radio tower.... etc.). A traveling electric field has associated magnetic field with it. Both these fields are perpendicular to each other (see **Figure. I.2**), and both are also perpendicular to the direction of wave propagation **[8].**

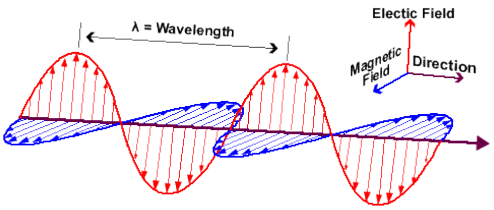

Figure I.2: Free space electromagnetic wave **[8].**

I.4.1. Electromagnetic waves spectrum:

The electromagnetic (EM) spectrum is a continuous range of electromagnetic radiation, extending from very short wavelengths ($<300 \times 10^{-9}$ m), corresponding to high energy, to very long wavelengths (cm, m, km), corresponding to low energy. Energy is inversely related to wavelength (and directly proportional to frequency) (see **Figure I.3**). Electromagnetic waves are characterized by:

- **Wavelength (λ)** is the distance traveled by the energy during one cycle from crest to crest, usually expressed in metric units (meters, centimeters, etc.).
- **Frequency** is the number of cycles repeated during unit time (usually 1 second).
  This is given in hertz (cycles per second). A kilohertz (kHz) is 1000 cycles per second.

Note: As frequency increases, wavelength becomes smaller. EM waves can be generated in different frequency bands: radio, microwave, infrared, visible, ultraviolet, x-rays, gamma rays (see **Figure I.3**) **[8]**.

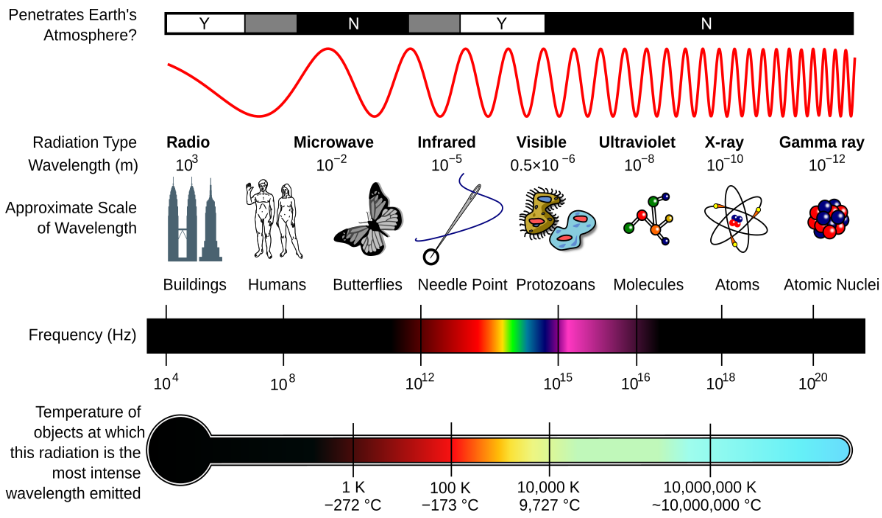

Figure I.3*:* Electromagnetic Spectrum **[8].**

I.4.2. Radio frequency (RF)

Radio frequency (RF) refers to any electromagnetic wave frequency in the range extending from below 3 kHz to about 300 GHz, including those used for communication signals such as radio and television broadcasting, cellular networks, satellite transmissions, and radar systems. RF waves occupy the lowest frequency range and the longest wavelengths within the electromagnetic spectrum.

Radio propagation: is the behavior of radio waves when they are transmitted or propagated from one point on the earth to another, or into various parts of the atmosphere.

Such a slight waves, radio waves are affected by the phenomena of reflection, refraction, diffraction, absorption, polarization and scattering **[8].**

I.4.3. The electrical properties of the transmission medium

Transmission media can be classified as guided or unguided. Guided media, such as twisted pair, coaxial cable, and optical fiber, provide a physical path for signal propagation, while unguided media use antennas to transmit signals through air, vacuum, or water.

Key properties of transmission media include:

- **Permittivity (ε):** Measures a material's resistance to forming an electric field, describing how electric flux is generated per unit charge. It is given by $\varepsilon = \varepsilon_0 \varepsilon_r$, where ε_0 is the vacuum permittivity (8.854×10^{-12} F/m) and ε_r is the relative permittivity of the medium.

- **Permeability (μ):** Also called magnetic permeability, it relates magnetic induction to magnetic field intensity. It is given by $\mu = \mu_0 \mu_r$, where μ_0 is the permeability of free space ($4\pi\times10^{-7}$ H/m) and μ_r is the relative permeability.
- **Conductivity (σ):** Indicates a material's ability to conduct electric current; perfect dielectrics have $\sigma \approx 0$**[8].**

I.5. Antenna Field Regions

The electromagnetic space surrounding an antenna is divided into three principal regions as shown in **Figure I.4,** each characterized by distinct field behaviors and boundary criteria:

Reactive Near-Field Region

- Closest to the antenna, dominated by stored (reactive) energy.
- Outer boundary typically defined as:

$$R < 0.62\sqrt{\frac{D^3}{\lambda}} \quad \textbf{(Eq I.1)}$$

Where: D is the largest antenna dimension and λ isthe wavelength.

- Fields are primarily inductive and capacitive, with minimal radiation.

Radiating Near-Field (Fresnel) Region

- Lies between the reactive near field and the far field.
- Radiation predominates, but the angular distribution of fields still depends on distance.
- Boundaries:

$$0.62\sqrt{\frac{D^3}{\lambda}} \leq R < \frac{2D^2}{\lambda} \quad \textbf{(Eq I. 2)}$$

- The field pattern varies with radial distance, and radial components may be significant.
- Sometimes referred to as the Fresnel region by analogy to optics.
- This region may not exist if the antenna dimension is small compared to the wavelength.

Far-Field (Fraunhofer) Region

- Begins at:

$$R \geq \frac{2D^2}{\lambda} \quad \textbf{(Eq I. 3)}$$

Fields are essentially transverse, with electric and magnetic components orthogonal and in phase.

- Angular distribution of radiation is independent of distance.

- Radiation pattern is well defined, typically with one or more major lobes and few minor lobes.
- For certain antennas (e.g., multibeam reflectors), stricter criteria may be required due to phase sensitivity **[9].**

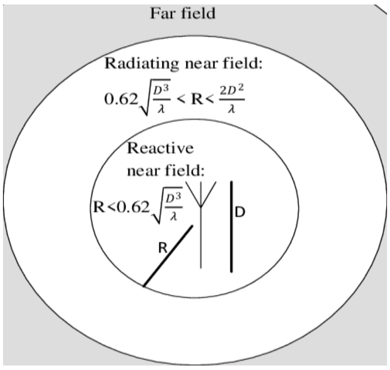

Figure I.4: The different regions of the antenna field **[10]**.

Far-field patterns stabilize at $R = \frac{2D^2}{\lambda}$, accurately representing the antenna's true behavior **[9].**

I.6. Characteristics of Antenna

In wireless communications, each application highlights certain characteristics of antennas. In general, an antenna used in one type of application cannot be used in another. An antenna can be characterized by:

I.6.1. Radiation Patterns

Radiation patterns are mathematical functions or graphical representations of the radiation properties of an antenna as a function of spatial coordinates **(**see **Figure I.5).**

- The radiation pattern is represented as a function of the directional coordinates.
- **Field Pattern:** A trace of the electric (or magnetic) field strength at a constant radius.
- **Power Pattern:** A graph of the spatial variation of the power density along a constant radius and usually plotted on a logarithmic scale or, more commonly, in decibels (dB) **[3].**

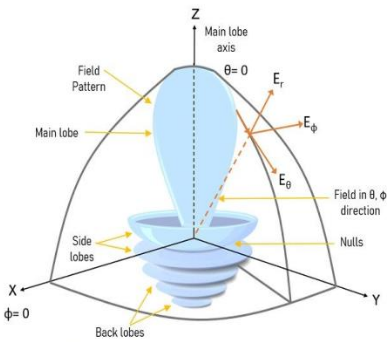

Figure I.5: Three-dimensional radiation pattern as a function of spatial coordinates **[12]**.

I.6.1.1. Normalized Patterns

The field and power patterns are normalized with respect to their maximum value, yielding normalized field and power patterns [11], [13].

Normalized field pattern: $E_n(\theta,\phi) = \frac{E(\theta,\phi)}{[E(\theta,\phi)]_{max}}$ (dimensionless) **(Eq I. 4)**

The normalized power pattern, P_n, is obtained by normalizing the radiation intensity, P, or the time averaged Poynting vector, $P(r,\theta,\phi)$, with respect to their maximum values [11], [13].

Normalized power pattern:

$$P_n(\theta,\phi) = \frac{P(\theta,\phi)}{P(\theta,\phi)]_{max}} = \frac{P(r,\theta,\phi)}{[P(r,\theta,\phi)]_{max}} \text{(dimensionless)}$$ **(Eq I. 5)**

where:

$P(r,\theta,\phi)$ = Poynting vector, $[P(\theta,\phi)]_{max}$ = maximum value of $P(\theta,\phi) W/m^2$

I.6.1.2. Radiation Pattern Lobes

A radiation pattern lobe is a portion of the radiation pattern bounded by regions of relatively low radiation intensity. Each lobe represents a direction in which the antenna radiates a significant amount of energy **(see Figure I.6).**

- **Major or Main lobe:** Radiation lobe containing the direction of maximum radiation.
- **Minor lobe:** Any lobe except a major lobe.
- **Side lobes:** Radiation lobes in any direction other than the intended main lobe.
- **Back lobes:** Radiation lobe whose axis makes an angle of approximately 180° with respect to the beam of an antenna.
- **Nulls:** Points of zero or minimum radiation **[3].**

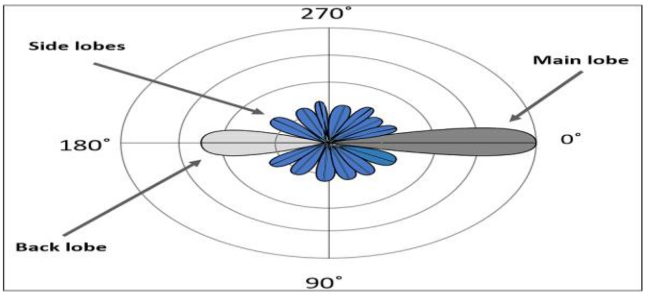

Figure I.6: Radiation lobes of an antenna pattern **[13]**.

I.6.1.3. Principal Planes

- **E-plane or Elevation Plane:** The plane containing the electric field vector and the direction of maximum radiation.

- **H-plane or Azimuth Plane:** The plane containing the magnetic-field vector and the direction of maximum radiation (**Figure I.7**) **[3].**

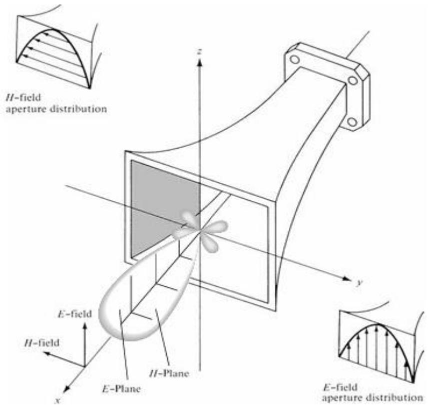

Figure I.7: Principal E-and H-plane patterns for a pyramidal horn antenna **[3].**

I.6.1.4. Isotropic, Directional, and Omnidirectional Patterns

a) Isotropic Antenna: An isotropic antenna is a fictitious antenna and is defined as an antenna which radiates uniformly in all directions. An isotropic antenna is a hypothetical lossless antenna, with which the practical antennas are compared. Thus, an isotropic antenna is used as reference antenna.

b) Directional Antenna: Antennas which directs its energy in one particular direction is said to be directional antennas. These antennas are having very high gain and directivity to cover large wireless distance. Examples are paraboloid reflector antenna, Yagi-Uda antenna, Log periodic antenna, etc.

c) Omnidirectional Antenna: Omnidirectional antennas are those antennas which will cover equally well in azimuth direction and having some angle in elevation direction. Basically, most of the wire antennas have omnidirectional radiation pattern. Examples are Whip antenna (monopole antenna), Dipoles antennas, etc **[14].**

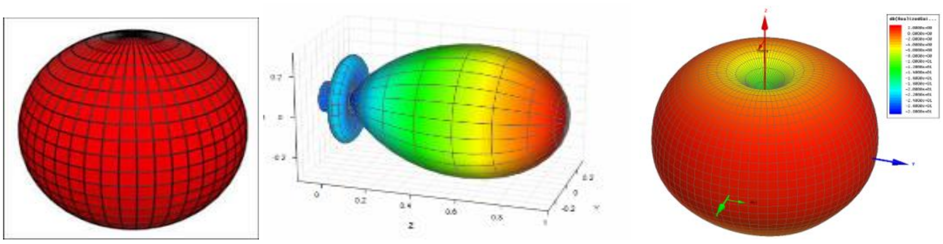

Figure I.8*:* Isotropic, Directional, and Omnidirectional Patterns (a) Isotropic Antenna **[15] (b)** Directional Antenna **[19**] **(c)** Omnidirectional Antenna **[20**].

I.6.1.5. Isotropic Radiation and Power Distribution

The isotropic radiator is a fundamental reference model in antenna theory, used to evaluate both gain and directivity. It represents a fictitious, ideal point source that radiates power uniformly in all directions, regardless of the observation angle. Although such an antenna cannot exist in practice, it remains essential for comparing the performance of real antennas. When an isotropic radiator is supplied with a power P_a, the power radiated per unit solid angle is expressed as:

$$P(\theta, \phi) = \frac{P_a}{4\pi} \ (W/sr) \qquad \textbf{(Eq I. 6)}$$

This quantity, measured in watts or watts per steradian, is particularly useful because it does not depend on the distance from the source.

The corresponding surface power density at a distance**r** is given by:

$$P(r, \theta, \phi) = \frac{P_a}{4\pi r^2} [\mathrm{W/m^2}] \qquad \textbf{(Eq I. 7)}$$

This formula describes how the radiated power spreads uniformly over the surface of a sphere centered on the source. The isotropic radiation pattern therefore appears as a perfect sphere in three dimensions. By providing an ideal benchmark, the isotropic radiator plays a central role in defining antenna gain, directivity, and other key parameters in electromagnetic radiation analysis **[3].**

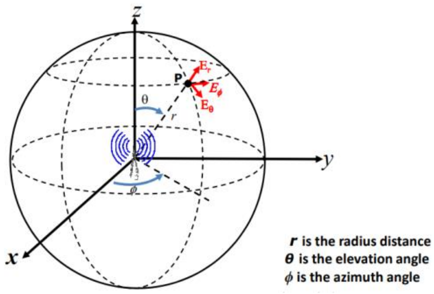

Figure I.9: The isotropic radiation pattern antenna in Spherical Coordinates **[18]**.

I.6.1.6. Radiation Pattern Parameters

I.6.1.6.a. Beamwidth (HPBW)

Beamwidth is the angular width of the main lobe where most radiated power is concentrated, defined using the half-power points, where the radiation intensity drops –3 dB from the peak. The angular distance between these two points is the half-power beamwidth (HPBW), as shown in **Figure I.10**. Both horizontal and vertical beamwidths are usually measured **[19].**

I.6.1.6.b. First-null beamwidth (FNBW or BWFN (BeamWidth First Null))

As shown in **Figure I.10, FNBW** or **BWFN** is the angle between two vectors, originating at the pattern's origin and tangent to the main beam at its base. Often, the approximation FNBW ≈ 2·HPBW is used **[20].**

The HPBW is the best parameter to describe the antenna resolution properties. In radar technology as well as in radioastronomy, the antenna resolution capability is of primary importance **[20]**.

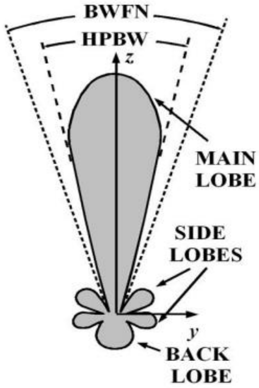

Figure I.10: 3D radiation pattern with HPBW, FNBW **[21]**.

I.6.2. Poynting Vector and Power Density

The instantaneous Poynting vector is defined as:

$$\mathbf{P}(r,\theta,\phi,t) = \mathbf{E}(r,\theta,\phi,t) \times \mathbf{H}(r,\theta,\phi,t) \quad \textbf{(Eq I. 8)}$$

which can also be expressed as:

$$\mathbf{P}(r,\theta,\phi) = \Re\{\mathbf{E}(r,\theta,\phi)e^{j\omega t}\} \times \Re\{\mathbf{H}(r,\theta,\phi)e^{j\omega t}\}[\mathrm{W/m^2}] \quad \textbf{(Eq I. 9)}$$

The average Poynting vector is given by:

$$\mathbf{P}(r,\theta,\phi) = \frac{1}{2}\Re\{\mathbf{E}(r,\theta,\phi) \times \mathbf{H}^*(r,\theta,\phi)\}[\mathrm{W/m^2}] \quad \textbf{(Eq I. 10)}$$

Note:

- Time-domain expressions: $\mathbf{E}(r,\theta,\phi,t), \mathbf{H}(r,\theta,\phi,t)$
- Phasor-domain expressions: $\mathbf{E}(r,\theta,\phi), \mathbf{H}(r,\theta,\phi)$

The Poynting vector is a real vector. Its magnitude represents the instantaneous or average power density of the electromagnetic wave, while its direction indicates the direction of power flow at a given point **[22].**

I.6.3. Radiation Power Density and Steradian

I.6.3.1. Radiation Power Density

Radiation power density describes how the electromagnetic power radiated by an antenna is distributed in space. In the far-field region, this distribution depends only on the angular direction $(\theta, \phi)$and not on the radial distance r. To analyze the total radiated power, the concept of solid angle is introduced, which allows the power flow to be evaluated over a spherical surface surrounding the antenna.

The radiation intensity is expressed as:

$$\boldsymbol{P}(\boldsymbol{\theta},\boldsymbol{\phi}) = r^2\, \boldsymbol{P}(\boldsymbol{r},\boldsymbol{\theta},\boldsymbol{\phi})(\mathrm{W/sr}) \qquad \textbf{(Eq I. 11)}$$

Note that $P(\theta,\phi)$ is a function of direction only and becomes independent of distance in the far-field region.

I.6.3.2. Steradian

The steradian (sr) is the unit used to measure the solid angle. The solid angle $\Omega$is defined as the ratio of a portion of a spherical surface area S to the square of the radius $r$of the sphere (see **Figure I.11) [22**].

$$\Omega = \frac{\mathrm{S}}{\mathrm{r}^2}(\mathrm{sr}) \qquad \textbf{(Eq I. 12)}$$

The solid angle subtended by a complete spherical surface is therefore:

$$\Omega = \frac{4\pi\mathrm{r}^2}{\mathrm{r}^2} = 4\pi(\mathrm{sr}) \qquad \textbf{(Eq II. 13)}$$

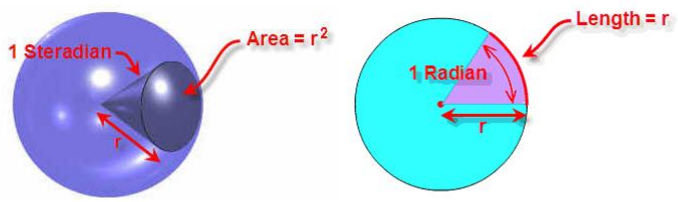

Figure I.11: Geometrical representation of the radian and steradian **[22**].

The differential surface element in spherical coordinates is given by:

$$ds = r^2 \sin\theta \, d\theta \, d\phi \, \hat{n} \qquad \textbf{(Eq I. 14)}$$

where $r$is the radius of the sphere, $\theta$is the polar angle, $\phi$is the azimuthal angle, and $\hat{n}$is the unit vector normal to the surface.

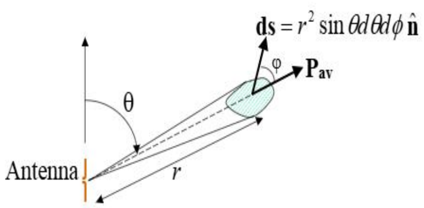

Figure I.12: Antenna radiation over a differential surface element **[22**].

I.6.3.3. Total Radiated Power using Radiation Intensity

The total radiated power is obtained by integrating the radiation power density over a closed surface surrounding the antenna:

$$P_{\mathrm{rad}} = \iint_S \boldsymbol{P}(\boldsymbol{r},\boldsymbol{\theta},\boldsymbol{\phi}) \cdot d\boldsymbol{s} = \frac{1}{2}\iint_S \mathrm{Re}[\mathbf{E}\times\mathbf{H}^*]\cdot d\boldsymbol{s}\ (\mathrm{W}) \qquad \textbf{(Eq I. 15)}$$

where:

The integration is performed over a closed surface enclosing the antenna, and the surface must be sufficiently far from the antenna to satisfy far-field conditions.

I.7. Directivity

In the 1983 IEEE standard, the term directivity replaced the earlier term directive gain, which was deprecated. This change aligns with common use among antenna engineers and international standards. Directivity is the ratio of the radiation intensity in a given direction to the average radiation intensity over all directions. The average intensity is the total radiated power divided by 4π. If no direction is specified, the direction of maximum radiation is implied. Mathematically, using $P_0 = P_{\text{rad}}/4\pi$, it is expressed as **[3]**:

$$D(\theta, \phi) = \frac{P(\theta,\phi)}{P_0} = \frac{4\pi P(\theta,\phi)}{P_{rad}} \qquad \textbf{(Eq I. 16)}$$

If the direction is not specified, it implies the direction of maximum radiation intensity (maximum directivity) expressed as:

$$D_{max} = \frac{P_{max}}{P_0} = \frac{4\pi P_{max}}{P_{rad}} \qquad \textbf{(Eq I. 17)}$$

Where: $D(\theta, \phi)$ = directivity (dimensionless), D_{max} = maximum directivity (dimensionless), $P(\theta,\phi)$ = radiation intensity (W/ Steradian), P_{max} = maximum radiation intensity (W/Steradian), P_0 = radiation intensity of isotropic source (W/Steradian),

P_{rad} = total radiated power (W).

Directivity can also be expressed in decibels dB, mathematically, it is expressed as:

$$D_{dB}(\theta,\phi) = 10 \cdot \log_{10}[D(\theta,\phi)] \qquad \textbf{(Eq I. 18)}$$

If no direction is specified, the maximum directivity in dB is given by:

$$D_{max(dB)} = 10\log_{10}[D_{max}] \qquad \textbf{(Eq I. 19)}$$

I.8. Antenna Efficiency

The total antenna efficiency e_0 is used to take into account losses at the input terminals and within the structure of the antenna.

e_0 is due to the combination of number of efficiencies. In general, the overall efficiency can be written as:

$$e_0 = e_r e_c e_d \qquad \textbf{(Eq I. 20)}$$

Where:

e_0= total efficiency (dimensionless)

e_r= reflection (mismatch) efficiency = $(1-|\Gamma|^2)$(dimensionless)

e_c= conduction efficiency (dimensionless), e_d= dielectric efficiency (dimensionless)

$\Gamma$is the voltage reflection coefficient at the input terminals of the antenna:

$$\Gamma = \frac{Z_{in} - Z_0}{Z_{in} + Z_0} \qquad \textbf{(Eq I. 21)}$$

where:

Z_{in} = antenna input impedance, Z_0 = characteristic impedance of the transmission line.

Usually,e_c and e_d are very difficult to compute, but they can be determined experimentally. Even by measurements they cannot be separated, and it is usually more convenient to write it as:

$$e_0 = e_r e_{cd} = e_{cd}(1-|\Gamma|^2) \qquad \textbf{(Eq I. 22)}$$

where $e_{cd} = e_c e_d$= antenna radiation efficiency, which is used to relate the gain and directivity **[3]**.

I.9. Gain

Gain is an important parameter in antenna performance, as it accounts for both directionality and efficiency, unlike directivity, which describes only the directional characteristics of the radiation pattern. The gain in a given direction is defined as the ratio of the radiation intensity in that direction to the radiation intensity that would be obtained if the accepted input power were radiated isotropically **[3].** For an isotropic radiator, this leads to:

$$G(\theta,\phi) = \frac{4\pi P(\theta,\phi)}{P_{\text{in}}} \qquad \textbf{(Eq I. 23)}$$

In practice, gain is often expressed relative to a reference antenna, typically a dipole or a lossless isotropic source, with both antennas excited by the same input power. When the direction is not specified, gain refers to the maximum radiation direction.

The total radiated power P_{rad} is related to the input power $P_{\text{in}}$by:

$$P_{\text{rad}} = e_{\text{cd}} P_{\text{in}} \qquad \textbf{(Eq I. 24)}$$

where $e_{\text{cd}}$is the radiation efficiency. According to IEEE standards, antenna gain does not include impedance or polarization mismatch losses **[3].** The gain is therefore related to the directivity by:

$$G(\theta,\phi) = e_{\text{cd}} D(\theta,\phi) \qquad \textbf{(Eq I. 25)}$$

The maximum value of the gain is related to the maximum directivity is given by:

$$\text{G} = e_{\text{cd}} D_{max} \qquad \textbf{(Eq I. 26)}$$

The absolute gain G_{abs} accounts for reflection or mismatch losses that occur when the antenna element is connected to the transmission line:

$$G_{abs} = e_r G(\theta,\phi) = (1-|\Gamma|^2)G(\theta,\phi) = e_r e_{cd} D(\theta,\phi) = e_o D(\theta,\phi) \quad \textbf{(Eq I. 27)}$$

where $e_r = (1-|\Gamma|^2)$: reflection (mismatch) efficiency, e_o: overall efficiency.

If the antenna is perfectly matched to the transmission line, meaning the input impedance Z_{in} equals the characteristic impedance $Z_c(|\Gamma|=0)$, then the two gains are identical:

$$G_{abs} = G \quad \textbf{(Eq I. 28)}$$

For maximum values:

$$G_{abs} = e_o D_0 \quad \textbf{(Eq I. 29)}$$

I.10. Beam Efficiency

Beam efficiency (BE) is a parameter used to assess antenna performance by quantifying the fraction of radiated power contained within the main beam. For an antenna whose main lobe is directed along the z-axis ($\theta = 0$), beam efficiency is defined as:

$$BE = \frac{\text{Power transmitted (or received) within cone angle } \theta_1}{\text{Total power transmitted (or received) by the antenna}} \text{(dimensionless).} \quad \textbf{(Eq I. 30)}$$

$$BE = \frac{\int_0^{2\pi}\int_0^{\theta_1} U(\theta,\phi)\sin\,\theta\, d\theta\, d\phi}{\int_0^{2\pi}\int_0^{\pi} U(\theta,\phi)\sin\,\theta\, d\theta\, d\phi} \quad \textbf{(Eq I. 31)}$$

Where: θ_1 is the cone half-angle, typically chosen at the first null of the radiation pattern. Beam efficiency therefore represents the fraction of total radiated power contained in the main lobe. High beam efficiency values (above 90%) are required in applications such as radar, radiometry, and radio astronomy to minimize side lobe radiation **[3].**

I.11. Effective Area and Gain Relationship

The effective area A_e of an antenna is related to its physical size and shape. It quantifies how efficiently an antenna captures or radiates energy in a given direction.

The relationship between antenna gain and effective area is given by:

$$G_{\max} = \frac{4\pi A_e}{\lambda^2} = \frac{4\pi f^2 A_e}{c^2} \quad \textbf{(Eq I. 32)}$$

Where: $G_{\max}$= maximum antenna gain (dimensionless), A_e= effective area (m²), λ= carrier wavelength (m), f= carrier frequency (Hz), c= speed of light (approximately 3×10^8m/s)

Table I.2 presents common antenna types with their corresponding gain and effective area formulas. It shows how antenna geometry and wavelength affect radiation performance, where larger effective areas generally result in higher gain.

Antenna Type	Effective Area, meter^2	Power Gain relative to Isotropic Antenna
Isotropic	$\lambda^2/4\pi$	1
Infinitesimal dipole or loop	$1.5\lambda^2/4\pi$	1.5
Half-wave dipole	$1.64\lambda^2/4\pi$	1.64
Horn, mouth area A	$0.81A$	$10A/\lambda^2$
Parabolic, face area A	$0.56A$	$7A/\lambda^2$
Two crossed, perpendicular dipoles	$1.15\lambda^2/4\pi$	1.15

Table I.2: Antenna Types with gain and effective area formula **[23]**.

The relationship between antenna gain and effective area is fundamental to antenna selection and system design. Proper evaluation of these parameters ensures optimal signal coverage, efficiency, and reliable communication performance **[23]**.

I.12. Input Impedance

The input impedance Z_{in} of an antenna is the ratio of voltage to current at its terminals and represents the impedance seen by an incident electromagnetic (EM) wave. It is frequency-dependent and expressed as:

$$Z_{\text{in}} = R_{\text{in}} + jX_{\text{in}} \quad \textbf{(Eq I.33)}$$

- R_{in} (resistance): the real part of the input impedance, representing the power radiated by the antenna and any ohmic losses.
- X_{in} (reactance): the imaginary part, representing stored energy in the antennas near field (inductive or capacitive) that does not radiate.

To achieve efficient radiation, the antenna must match the transmission line impedance (typically $50\,\Omega$) to free space ($\sim 377\,\Omega$). Any mismatch in R_{in} or X_{in} reduces radiation efficiency, so Z_{in} should be as close as possible to the line impedance across the operating bandwidth (see **Figure I.13) [24].**

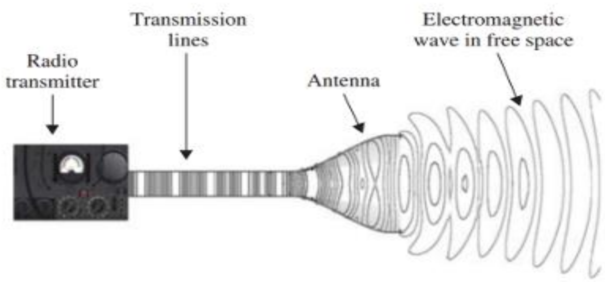

Figure I.13: illustrating the basic concept of input impedance and transmission line matching for the efficient radiation of an EM wave **[24]**.

I.13. Reflection Coefficient and Return Loss

To ensure efficient radiation, an antenna's impedance input must be matched to the characteristic impedance of the transmission line (typically 50 Ω). Any mismatch causes part of the signal to be reflected back toward the source, reducing transmitted power.

The reflection coefficientΓquantifies this effect and is defined as**:**

$$S_{11} = \Gamma = \frac{Z_{in} - Z_0}{Z_{in} + Z_0} \qquad \textbf{(Eq I.34)}$$

where:

Z_{in} is the antenna input impedance and Z_0 is the transmission line impedance.

When $Z_{in} = Z_0$, $\Gamma = 0$, meaning no reflection occurs and all power is transferred. The return loss (RL**)** expresses the reflection coefficient in logarithmic form:

$$\text{RL} = -20\log_{10} |\Gamma| \text{ [dB]} \qquad \textbf{(Eq I.35)}$$

A well-designed antenna typically has $\text{RL} < -10$ dB, indicating that at least 90% of the power is delivered to the antenna **[24].**

I.14. S-Parameters

S-parameters, or scattering parameters, describe the behavior of an N-port network through a scattering matrix. Each element of the matrix relates the voltage of an incident wave to that of a reflected wave at a given port.

S-parameters can be used to calculate the reflection coefficient at each port, allowing evaluation of the transmission efficiency of the network. They are easily measured using modern network analyzers.

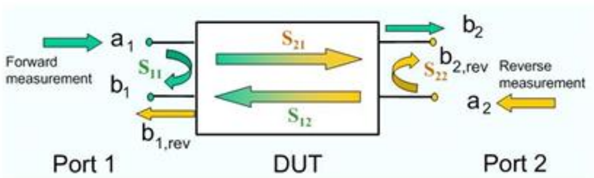

Figure I.14: The basic principle of S-parameters for a two-port network **[24].**

As shown in **Figure I.14,** S_{11} and S_{22} represent the reflection coefficients at ports 1 and 2, respectively, with all other ports terminated in matched loads. Similarly, $S_{21}$and S_{12}denote the transmission coefficients from port 1 to 2 and from port 2 to 1, respectively, under the same matched-load conditions **[24**].

In this setup, the Device Under Test (DUT) is simply the component, circuit, or antenna being measured. It is the physical system connected to the measurement equipment (such as a network analyzer). The DUT is the subject of the test, and the S-parameters describe how it behaves when signals are applied to its ports.

a_1: incident wave entering Port 1 of the DUT, b_1: reflected wave leaving Port 1 of the DUT

a_2: incident wave entering Port 2 of the DUT, b_2: reflected wave leaving Port 2 of the DUT

I.15. VSWR

The voltage standing wave ratio (VSWR) of a transmitting antenna is defined by:

$$\text{VSWR} = \frac{1+|\Gamma|}{1-|\Gamma|}\text{(dimensionless)} \quad \textbf{(Eq I. 36)}$$

Same as Γ, VSWR is also a common parameter used to characterize the matching property of a transmitting antenna. Possible values of VSWR are from 1 to ∞.

VSWR = 1 ⇒ perfectly matched. VSWR = ∞⇒ completely unmatched **[22**].

I.16. Bandwidth of an Antenna

The bandwidth of an antenna is defined as the range of usable frequencies within which the performance of the antenna with respect to some characteristics conforms to a specified standard **[25**]. The parameter most commonly taken into account here is the impedance match (i.e. VSWR< 1.5), but other parameters like gain or side lobe suppression may serve as a bandwidth criterion **[25].**

$$\text{BW}=\frac{f_U}{f_L} \quad \textbf{(Eq I. 37)}$$

Where:

f_U is the highest or upper usable frequency and f_L is the lowest usable frequency. An antenna is said to be broadband when BW is equal or greater than 2**[25**].

Note that when $|\Gamma| = \rho = 20\log(0.3162) = -10\text{dB}$.

$$\text{VSWR} = \frac{1+|\Gamma|}{1-|\Gamma|} = \frac{1+0.3162}{1-0.3162} = 1.93 \approx 2 \quad \textbf{(Eq I. 38)}$$

Hence the impedance bandwidth can also be specified by the frequency range within which VSWR ≤ 2 **[18**].

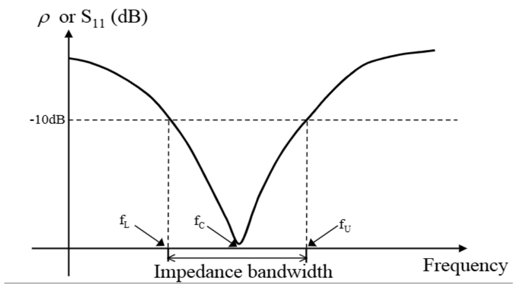

Figure I.15 :S11 vs. Frequency Bandwidth **[25]**.

There exists also a different definition of bandwidth which is valid only for narrowband antennas:

$$BW \text{ in } (\%) = \frac{f_U - f_L}{f_c} . 100 \qquad \textbf{(Eq I.39)}$$

where: f_c is the center frequency.

I.17. Polarization

Antenna polarization is defined by the trajectory traced by the tip of the electric-field vector **E**, with three common types: **linear, circular, and elliptical [22]**.

(a) Linear polarization: A plane wave is linearly polarized at a fixed observation point if the tip of the electric field vector **E** at that point moves along the same straight line at every instant of time (**Figure I.16)**.

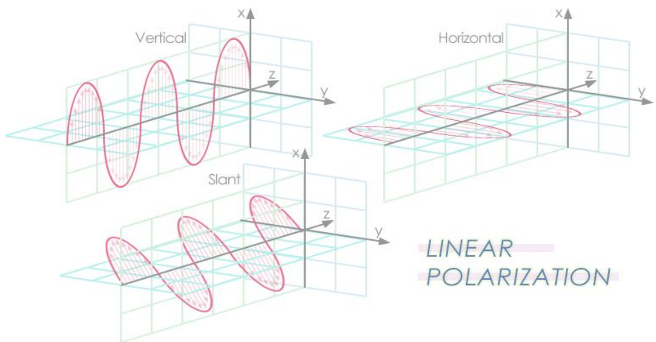

Figure I.16: Linear polarization types of electromagnetic waves vertical, horizontal, and slant showing electric field orientation relative to the direction of propagation **[26**].

(b) Circular Polarization: At a fixed observation point, a plane wave is circularly polarized if the tip of the electric-field vector **E** traces a circle over time. It can be right-handed (rotating clockwise) or left-handed (rotating counterclockwise) (**Figure I.17)**.

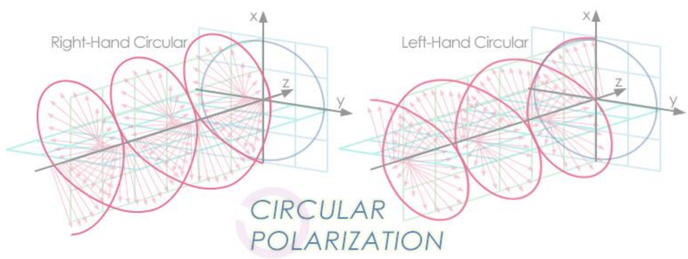

Figure I.17: Right-hand and left-hand circular polarization illustrated by electric field rotation in the XY-plane along the Z-axis direction of wave propagation **[26]**.

(c) Elliptical Polarization: At a fixed observation point, a plane wave is elliptically polarized if the tip of the electric-field vector **E** traces an ellipse over time. It can be right-handed (rotating clockwise) or left-handed (rotating counter clockwise) (**Figure I.18)**.

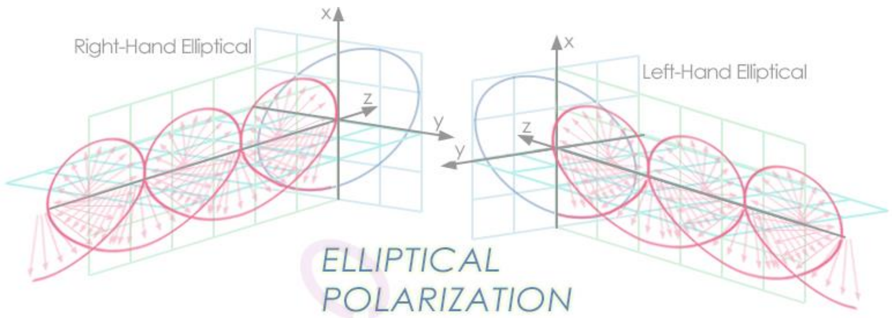

Figure I.18: Right-hand and left-hand elliptical polarization showing electric field rotation in the XY-plane along the Z-axis direction of wave propagation **[26]**.

I.18. Conclusion

This chapter has provided the essential theoretical background of antenna fundamentals, covering their historical evolution, definitions, electromagnetic principles, field regions, and key performance parameters such as radiation patterns, gain, directivity, and efficiency. These concepts form the scientific basis for analyzing how antennas operate and how their characteristics determine communication quality.

By establishing this foundation, the chapter prepares the ground for the following sections, where different antenna types will be examined in detail, with particular emphasis on microstrip patch antennas. Subsequent chapters will also address their optimization and integration into advanced wireless systems, highlighting their critical role in meeting the stringent requirements of upcoming 6G technologies**.**

Bibliography of chapter I

[1]. W. L. Stutzman and G. A. Thiele, “Antenna Theory and Design*”,* 3rd ed. Hoboken, NJ, USA: John Wiley & Sons, pp. 3–4, ISBN: 978-0-470-57664-9, 2012.

[2]. IEEE Standard Definitions of Terms for Antennas, *IEEE Std* 145-1983, New York, NY, USA: IEEE, pp. 1–31, June 22, 1983.

[3]. C. A. Balanis, “Antenna Theory: Analysis and Design”, 3rd ed. Hoboken, NJ, USA: John Wiley & Sons, Inc., pp. 1–67, ISBN: 0-471-66782-X, 2005.

[4]. M. Odiamenhi, H. Jahanbakhsh Basherlou, C. H. See, N. Ojaroudi Parchin, K. Goh, and H. Yu, "Advancements and Challenges in Antenna Design and Rectifying Circuits for Radio Frequency Energy Harvesting," *Sensors*, vol. 24, no. 21, Art. no. 6804, ISSN: 1424-8220, Oct. 2024.

[5].https://em.groups.et.byu.net/embook/figs/figs9.html

[6]. A. K. Banale, K. A. Fante, S. S. Kumar, and A. Sampath, "Designs and materials of flexible wearable microstrip patch antennas: a systematic review," *Discover Appl. Sci.*, vol. 7, no. 477, pp. 1, ISSN: 3008-3101, May 2025.

[7]. K. D. Prasad, “Antennas and Wave Propagation”, *New Delhi, India: Satya Prakashan*, p. 1, 2001.

[8]. J. N. Shehab, "Antenna Theory and Design," *Lecture notes,* Dept. of Communication Engineering, College of Engineering, University of Diyala, 3rd year class, pp. 1–4, 2014.

[9]. C. A. Balanis, “Antenna Theory: Analysis and Design”, *4th ed. Hoboken, NJ, USA: Wiley,* pp. 60–64, ISBN: 978-1-118-64206-1, 2016.

[10].https://www.researchgate.net/figure/llustration-of-antenna-field-regions59_fig2_333375934

[11]. A. R. Harish and M. Sachidananda, “Antennas and Wave Propagation”, *New Delhi, India; New York, NY,* USA: Oxford University Press, pp. 34–36, ISBN: 978-0-19-568666-1, 2007.

[12].https://electronicsdesk.com/radiation-pattern-of-antenna.html

[13]. Tutorialspoint, "Antenna Theory: Types of Antennas," [Online]. Available: https://www.tutorialspoint.com/antenna_theory/antenna_theory_types_of_antennas.htm. [Accessed: Jun. 25, 2026].

[14]. P. Dhande, "Antennas and its applications," *DRDO Science Spectrum*, Defence Scientific Information & Documentation Centre (DESIDOC), pp. 74, Mar. 2009.

[15].https://www.researchgate.net/figure/Figure-1-23-Radiation-patterns-isotropic-antenna44_fig12_361995399

[16].https://forums.ni.com/t5/LabVIEW/Antenna-Radiation-Pattern-in-3D/td-p/2886874

[17]. Maarten Baert's website. [Online]. Available: https://www.maartenbaert.be/search.php

[18]. R. Medina-Sanchez, "Antenna Theory Fundamentals," *presented at the Radio Frequency Spectrum Management Workshop,* University of Puerto Rico at Mayagüez, Mayagüez, PR, May 25, 2016.

[19]. A. A. Kishk, "Fundamentals of Antennas," *Center of Electromagnetic System Research (CEDAR)*, Department of Electrical Engineering, University of Mississippi, pp. 5, 2009.

[20]. N. K. Nikolova, "Fundamental Antenna Parameters," in *Lecture Notes: Antennas*, Dept. of Electrical and Computer Engineering, McMaster University, Hamilton, ON, Canada, pp. 63–64, 2018.

[21].

S. Joardar, "Basics of Antennas," *presentation, Giant Metrewave Radio Telescope, National Centre for Radio Astrophysics,* Tata Institute of Fundamental Research, Pune, India, pp. 10–11, 2005.

[22]. H. T. Hui, "Antennas," *lecture notes,Dept. of Elect. and Comput. Eng*., National University of Singapore, Singapore, 2010.

[23]. I. Eid, "Wireless and Mobile Networks," *Faculty of Information Technology,* Computer Systems Engineering Department, course material, Mar. 5, 2014.

[24]. S. Paine, "Basic Antenna Design Handbook," *Dept. of Elect. Eng., University of Cape Town,* Cape Town, South Africa, pp. 5–8, Mar. 29, 2017.

[25]. M. Reckeweg, "Antenna basics," *white paper, Rohde & Schwarz, Munich, Germany*, White Paper 8, GEP_WP01, pp. 19, Nov. 2014.

[26].https://jemengineering.com/blog-intro-to-antenna-polarization/

Chapter II: Advanced Antenna Architectures and Terahertz Technologies

II.1. Introduction

This chapter presents the fundamental concepts and classifications of antennas, with a particular focus on planar antennas. The structural characteristics, advantages, limitations, and feeding techniques of microstrip antennas are discussed in detail. In addition, several other planar antenna types such as PIFA, slot antennas, and printed monopole and dipole antennas are introduced.

Furthermore, the chapter explores advanced antenna technologies, including smart antennas, metamaterial-based antennas, phased array antennas, MIMO systems, and reconfigurable antennas, which are essential for improving the performance of modern wireless networks. Finally, the chapter provides an overview of terahertz (THz) technology, its role in future 6G communication systems, its applications, and the main challenges associated with THz antenna design.

II.2. Microstrip Patch Antennas

Planar antennas are extensively employed in modern wireless communication systems due to their compact size, low profile, and compatibility with planar fabrication technologies. These antennas are typically realized using printed circuit board (PCB) techniques, where the radiating element is etched or printed on a dielectric substrate **[1]**.

The most common type is the microstrip patch antenna, which is also utilized in this study. The following section presents its structure, various types, advantages, limitations, applications and feeding techniques.

II.2.1. Structure of a Microstrip Antenna

Patch antennas are made up of three layers which are a rectangular ground plane at the bottom, a dielectric substrate in the middle, and the patch on the top. Both of the ground and the patch layers are made of conductors such as copper or gold **[2]**. These metals are preferred because of their low resistivity, resistance to oxidation, good solderability, and strong adhesion to dielectric substrates **[3].**

Both of the dielectric material and the ground plane having the same dimensions as shown in **Figure II.1** **[2]**. The radiating patch and feed line are etched on the same dielectric substrate, allowing compact integration with microwave circuits **[3].**

The patch can be designed in various geometrical shapes depending on the required antenna characteristics. However, rectangular, square, and circular patches are most commonly used due to their simple analysis, predictable performance, and ease of fabrication. Despite differences in geometry, their radiation behavior is similar, as they operate in a manner analogous to a radiating dipole.

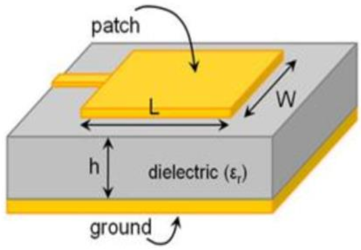

Figure II.1: Microstrip Antenna **[4].**

Microstrip patch antennas radiate mainly due to fringing fields at the edges of the patch and the ground plane. While low-permittivity thick substrates improve bandwidth and efficiency, high-permittivity substrates are preferred for antenna miniaturization, making a design trade-off necessary, particularly at high-frequency and THz applications. The typical range for dielectric constant of the substrate being used is **$2.2 \leq \varepsilon_r \leq 12$ [3].**

II.2.2. Types of Microstrip Patch Antenna

Microstrip patch antennas can be designed in various geometrical shapes, each offering specific characteristics and applications. Common types include **(Figure II.1) [3]**:

- **Square:** Square-shaped radiating patch; widely used due to ease of design and broad applicability.
- **Rectangular:** Rectangular patch; dominant in communication systems because of tuning flexibility.
- **Dipole:** Dipole-like patch; provides broadband performance, suitable for wider frequency coverage.
- **Circular:** Circular patch; enables circular polarization, commonly applied in satellite and mobile communication.
- **Elliptical:** Elliptical patch; produces distinct radiation patterns, useful for specialized applications.
- **Triangular:** Triangular patch; less common but advantageous in certain compact designs.
- **Disc Sector:** Disc-sector patch; offers directional radiation, suitable for applications requiring specific angles.
- **Circular Ring:** Ring-shaped patch; allows variation in radiation characteristics, adaptable to different system needs.

Figure II.2: The most common shapes of patch antennas **[5]**.

The choice of substrate material is a critical factor in microstrip antenna performance, as it must withstand environmental conditions such as temperature and humidity. The substrate thickness h strongly affects the resonant frequency f_r and bandwidth (BW). Increasing h generally enhances bandwidth; however, excessive thickness can degrade resonance and reduce antenna efficiency **[3]**.

II.2.3. Advantages and Limitations of microstrip antennas

Microstrip antennas have several advantages compared to conventional microwave antennas, and therefore many applications cover the broad frequency range from 100MHz – 100GHz. **[6]**.

Advantages:

- They are light in weight.
- They occupy low volume.
- They are of low-profile planer configuration.
- They can be made conformal to planar and non-planar surfaces.
- Their ease of mass production leads to a low fabrication cost.
- They are easy to implement on the device.
- They allow both linear polarization and circular polarization with simple feed.
- They can be made compact for use in personal mobile communication.
- They allow for dual- and triple-frequency operations.
- They act as an efficient radiator.
- They have low scattering cross section.
- They are mechanically robust when mounted on rigid surfaces.
- They are resistant to shock and vibration.
- They are well compatible for embedded antennas in handheld wireless devices.

However, these antennas also have some limitations as compared to conventional ones.
These are:

- They have narrow bandwidth.
- The efficiency is low.
- They have low gain.
- They have low power handling capacity.
- They have low isolation between radiating elements and feed.
- Complex feed structure required for high performance arrays.
- Large ohmic loss in the feed structure of arrays.
- Extraneous radiation from feed and junctions.
- Excitation of surface waves **[3]- [7].**

The feed line can be easily fabricated at the same time on the substrate There are ways to minimize the effect of some of these limitations. For example, bandwidth can be increased to more than 60% by using special techniques; lower gain and lower power handling limitations can be overcome through an array configuration. Surface wave-associated limitations such as poor efficiency, increased mutual coupling, reduced gain and radiation pattern degradations can be overcome by the use of photonic bandgap structures **[6]**.

II.2.4. Application of microstrip antennas

Microstrip patch antennas are widely adopted due to their robust design, ease of manufacturing, and low cost. Their versatility makes them suitable for numerous modern technologies **[8]-[9]:**

- **Global Positioning Systems (GPS):** High-permittivity sintered substrates enable accurate positioning in vehicles, aircraft, and marine applications, supporting millions of GPS receivers.
- **Radar Systems:** Ideal for detecting moving targets, microstrip antennas can be mass-produced using photolithography, offering dual performance at lower cost compared to conventional antennas**.**
- **Rectenna Systems:** Used for wireless transmission of DC power over long distances, requiring high performance and reliable connectivity.
- **Mobile and Satellite Communications:** Their small size and ability to support linear or circular polarization make them essential in compact mobile devices and satellite links, where circularly polarized patterns are achieved with circular patch designs.

- **Medical Applications:** Compact size and tunable electrical performance make them suitable for tissue detection and tumor treatment, offering promising biomedical uses.
- **Radio Frequency Identification (RFID):** The RFID system is a transponder or tag and a reader or transceiver. It can be used in different fields such as mobile communication, manufacturing, logistics, transportation, car parking, animal tracking, and health care. The RFID system operates over a frequency range from 30 Hz to 5.8 GHz
- **Interoperability for Microwave Access (WiMax)**: Another name of IEEE 802.16 standard is WiMax. Microstrip patch antenna is used in WiMax because it produces three important resonant modes at 2.7 GHz, 3.3 GHz, and 5.3 GHz**.**

Figure II.3: Different applications of Microstrip Patch antenna in wireless applications **[10]**.

Antennas are fundamental to modern wireless systems, reducing reliance on costly wired infrastructure. Microstrip patch antennas, valued for their radiation mechanism and functional performance, are driving the expansion of applications across communication, radar, radiometry, and electronic support systems. Their versatility and demand for wide bandwidth ensure continued growth in both commercial and defense technologies **[9]**.

In light of their numerous applications, the performance of microstrip antennas strongly depends on the choice of feeding techniques, which will be discussed in the following section.

II.2.5. Feeding techniques

The main objective of the feed line is to provide an input signal to excite the antenna. Feeding methods for microstrip patch antennas are categorized into two main groups as shown in **Figure II.4 [8]**:

(a) Contacting Techniques

In the contacting technique, using connecting elements (like a coaxial probe, microstrip line), the RF power is directly fed to the patch of an antenna.

(b) Non-Contacting Techniques

In non-contacting techniques, various feed methods, i.e., proximity coupling, aperture coupling are used for power transfer**.**

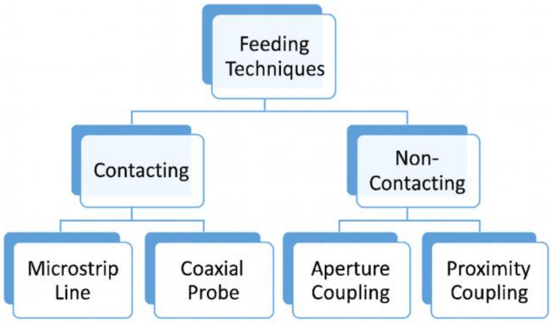

Figure II.4: classification of different feeding techniques **[8].**

II.2.6. Comparison of Feeding Techniques for Microstrip Patch Antennas

The feeding technique selection for microstrip antenna plays a very crucial role because various antenna quality parameters such as return loss, bandwidth, and efficiency of an antenna are directly affected by it **[8]**.

a) Microstrip Feedline:

This technique uses a metallic strip directly connected to the patch, both etched on the same substrate, forming a flat structure (see **FigureII.15**). It offers easy impedance matching and simple fabrication. However, it generates the highest spurious feed radiation among all techniques and provides a narrow bandwidth (typically 2%–5%) **[8]**.

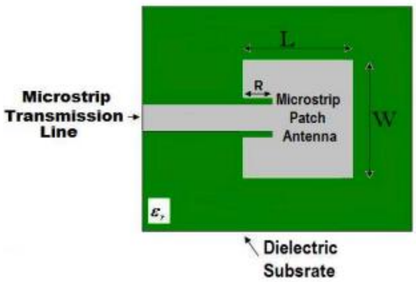

Figure II.5: Microstrip Feedline for microstrip antenna **[11].**

b) Coaxial Feed:

In this method, the inner conductor of the coaxial cable is connected to the radiating patch, while the outer conductor is attached to the ground plane (see **Figure II.6**). It offers simple impedance matching and produces lower spurious radiation compared to other techniques. The arrangement requires soldering and drilling, and the achievable bandwidth remains narrow, typically around 2%–5% **[8]**.

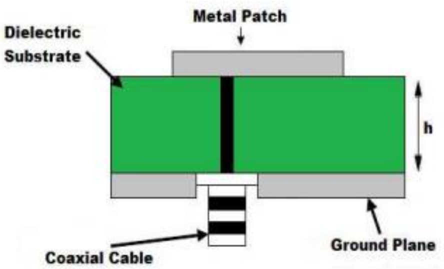

Figure II.6: Coaxial Feed for microstrip antenna **[11].**

c) Aperture Coupled Feed:

This method uses two sandwiched substrates to achieve electromagnetic coupling between the feed and the radiating patch **(**see **Figure II.7**). It offers easy impedance matching and produces moderate spurious radiation. However, the arrangement is complex due to strict alignment requirements, and the achievable bandwidth remains narrow, typically around 2%–5% **[8]**.

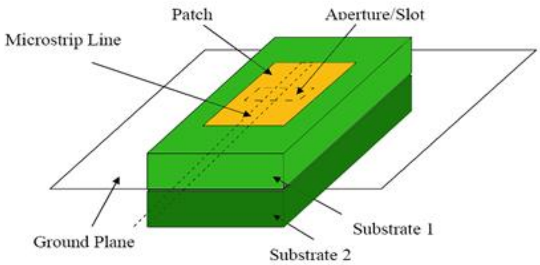

Figure II.7: Aperture Coupled Feed for microstrip antenna **[12].**

d) Proximity Coupled Feed:

The feed line is sandwiched between the two dielectric layers, and the radiating patch is kept on the top of the upper dielectric substrate **(**see **Figure II.8**). This method of feeding removes the spurious feed radiation and provides wider bandwidth (nearly 13%) **[8].**

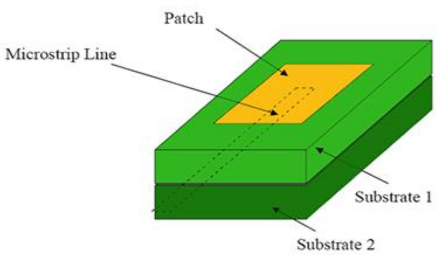

Figure II.8: Proximity Coupled Feed for microstrip antenna **[12].**

The choice of feeding method significantly influences antenna performance. A comparison of the most common techniques is presented in the following table:

Feeding Technique	Advantages	Disadvantages
Coaxial Feed	-Simple and easy impedance matching -It has lower spurious radiation	-It has large inductance for thick substrate -For it, soldering is needed
Microstrip Line	-It is monolithic -It is simple and easier to fabricate -Simple and easy impedance matching	-For thick substrate, it produces spurious radiation
Aperture Coupledfeed	-It does not have a deleterious effect on the bandwidth and efficiency due to the use of two dielectric layers. - It does not produce radiation from feed and other active devices	-It required a multi-layer design -It produces higher radiation from the back lobe.
Proximity CoupledFeed	-Easy impedance matching -Provide wider bandwidth	-Fabrication needed alignment -Less spurious fed radiation

Table II.1: Comparison of Feeding Techniques for Microstrip Patch Antennas **[8]**.

II.3. Types of Planar Antennas

II.3.1. Planar Inverted-F Antennas (PIFA)

Planar Inverted-F Antennas (PIFA) are compact antenna structures designed to achieve size reduction while maintaining acceptable radiation characteristics.

A typical PIFA consists of a top radiating plate connected to the ground plane through a shorting pin or plate, along with a feeding point (**Figure II.9)**. This configuration provides good impedance matching and reduced sensitivity to nearby objects, such as the user's hand or head, making PIFAs particularly suitable for portable and handheld devices. PIFAs are extensively used in mobile phones, tablets, and wearable devices and they can be easily modified to support multiband and broadband operation by adjusting the antenna geometry or introducing additional resonant paths **[13].**

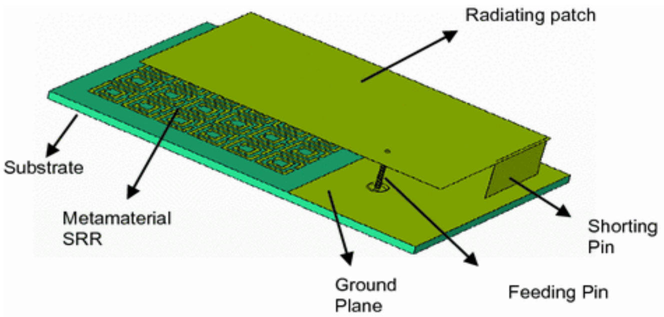

Figure II.9: Schematic of the PIFA Antenna **[14].**

II.3.2. Slot Antennas

Slot antennas are formed by cutting a narrow slot in a metallic surface or ground plane, and radiation occurs due to the electromagnetic fields around the slot. Unlike patch antennas, slot antennas radiate from the aperture rather than from a metallic conductor (**Figure II.10)**. They offer several advantages, including wider bandwidth, good polarization purity, and ease of integration with planar transmission lines such as microstrip or coplanar waveguides. Slot antennas are commonly used in microwave and millimeter-wave systems, radar applications, and compact wireless devices. Their radiation characteristics can be effectively controlled by modifying the slot shape, length, and feeding technique **[15].**

An example of this type of antenna is illustrated in the following Figure.

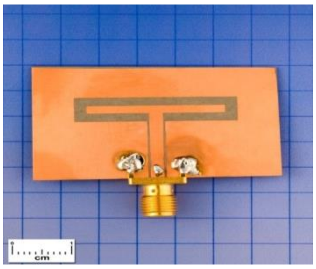

Figure II.10: Loaded Folded Slot Antenna, 4.7 GHz **[16].**

II.3.3. Printed Monopole and Dipole Antennas

Printed monopole and dipole antennas are planar implementations of traditional wire antennas, where the radiating elements are printed on a dielectric substrate (see **Figure II.11)**. These antennas exhibit radiation patterns similar to their wire counterparts while offering improved compatibility with planar circuits **[17].** Printed monopole antennas are particularly known for their wide impedance bandwidth and omnidirectional radiation characteristics, making them suitable for wideband and multiband wireless applications. Printed dipole antennas, on the other hand, provide balanced radiation and are often used in differential feeding systems. These antennas are widely employed in WLAN, Bluetooth, ultra-wideband (UWB), and Internet of Things (IoT) applications **[18].**

(a) (b)

Figure II.11: Fabricated antenna prototypes: (a) Monopole, (b) Dipole on FR-4 substrate **[19]-[20].**

II.3.4. Advanced Wireless Antennas

Advanced antennas have been developed to meet the increasing demand for higher data rates, better spectrum efficiency, and enhanced coverage in modern communication systems, including 4G, 5G, millimeter-wave systems, and beyond. These antennas employ sophisticated designs and technologies to improve system performance. The main types are detailed below :

II.3.4.1. Smart Antennas

Smart antennas combine antenna arrays with adaptive signal processing techniques to dynamically control the radiation pattern, steering the main beam toward desired users while placing nulls toward interferers. This capability improves the signal-to-noise ratio (SNR), reduces co-channel interference, and enhances overall system capacity. Smart antennas are extensively used in cellular base stations, emerging 5G networks, and other adaptive wireless systems. Key considerations in their design include array geometry, beamforming algorithms, real-time adaptation, and computational complexity. Through these features, smart antennas enable efficient spectrum utilization and more reliable communication in multi-user environments **[21].**

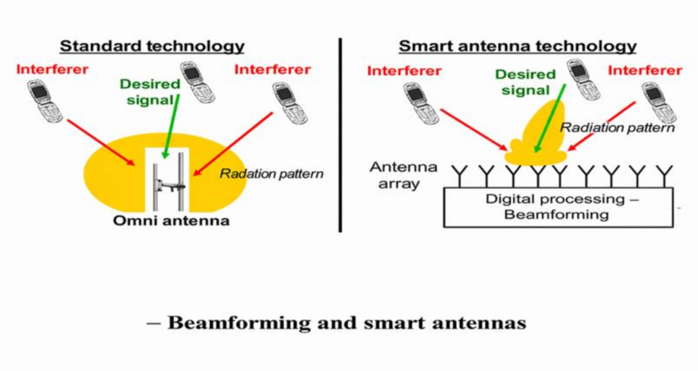

Figure II.12: Standard antenna and smart antenna with beamforming

II.3.4.2. Metamaterial Antenna

Metamaterials are artificially engineered materials with unique electromagnetic properties that are not found in natural materials. They enable improved control of electromagnetic wave propagation and have created new opportunities for enhancing antenna performance. In antenna systems, metamaterials are commonly used to improve radiation characteristics and increase antenna gain. However, achieving both high gain and compact antenna size remains a significant challenge **[22].**

II.3.4.2.1. Classification of materials

Metamaterials are fundamentally classified into several categories based on their permittivity and permeability values. Materials are grouped into four fundamental regions and are depicted in **Figure II.13** [22]-[23]:

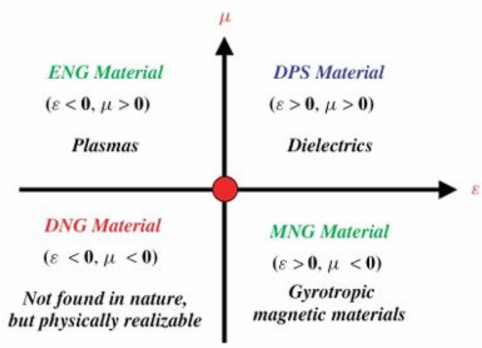

Figure II.13: Classification of physical environments depending on their effective values of permittivity (ε) and magnetic permeability (μ) **[22].**

Epsilon-Negative (ENG): characterized by negative permittivity ($\epsilon < 0$) and positive permeability ($\mu > 0$). In the microwave regime is typically achieved through periodic arrangements of thin metallic wires. This structure mimics plasma behavior at lower frequencies, where the effective permittivity

Mu-Negative (MNG): characterized by positive permittivity ($\epsilon > 0$) and negative permeability ($\mu < 0$), synthesized using resonant elements like Split-Ring Resonators (SRRs).

Double-Negative (DNG): characterized by negative permittivity and permeability ($\epsilon < 0$ and $\mu < 0$). They are known as left-handed materials; these properties are not found in naturally occurring substances. NG structures are typically man-made by combining electric and magnetic resonant elements, such as Split-Ring Resonators (SRRs) and thin metallic wire strips**.**

Double-Positive (DPS): known for isotropic dielectrics and right-hand materials, have both positive permeability and permittivity, being considered as conventional material (ϵ> 0 and μ> 0).

Several additional examples of metamaterial-based antennas are presented below:

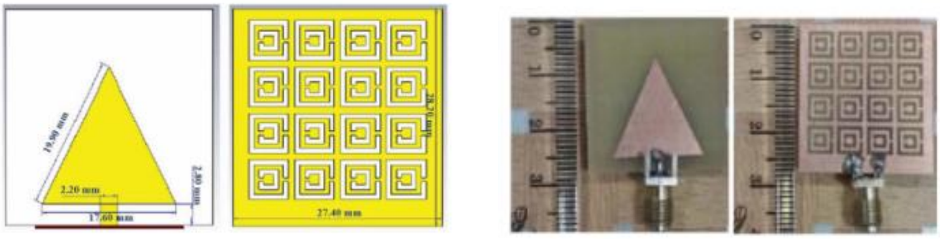

Figure II.14: Geometry and Fabricated triangular patch antenna with CSSR on the ground plane **[23].**

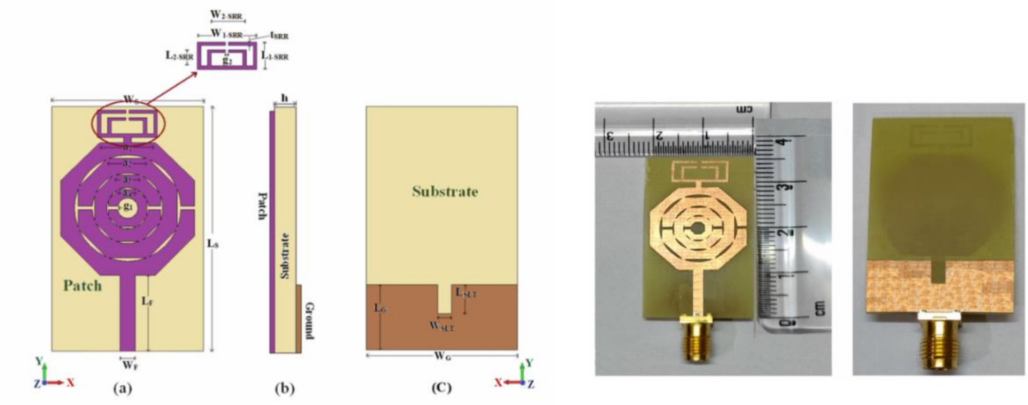

Figure II.15: Geometry and Fabricated Prototype of Metamaterial-Based SRR Antenna **[24].**

II.3.4.3. Phased Array Antennas

Phased array antennas consist of multiple radiating elements with individually controllable phase shifts, enabling electronic steering of the radiation beam without mechanical movement (see **Figure II.16)**. This allows rapid beam switching, high directivity, and adaptive coverage, which are essential in radar systems, satellite communications, and 5G, 6G millimeter-wave networks. Design challenges for phased arrays include precise phase control, element spacing optimization, sidelobe suppression, and maintaining impedance matching across all elements. Phased arrays are critical for systems requiring dynamic beamforming, high gain, and real-time directional control **[25].**

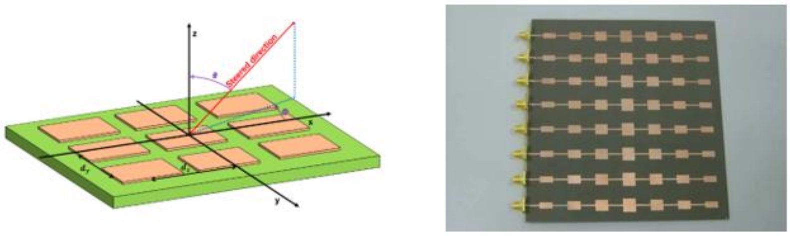

Figure II.16: Phased Array Antennas **[26]-[27].**

II.3.4.4. Reconfigurable Antennas

Reconfigurable antennas are antennas capable of dynamically altering their operating frequency, radiation pattern, polarization, or gain in response to changing system requirements or environmental conditions. According to Christodoulou and al [28], reconfiguration is achieved by *"deliberately changing its frequency, polarization, or radiation characteristics"* through techniques that redistribute surface currents and modify the effective electromagnetic aperture of the antenna. This electrical or structural modification allows a single antenna structure to perform multiple functions that would otherwise require several fixed antennas **[28].**

Reconfigurability can be implemented using various switching elements integrated into the radiating structure, such as PIN diodes (Positive-Intrinsic-Negative diodes), varactor diodes, RF-MEMS (Radio Frequency Micro-Electro-Mechanical Systems), optical switches, or tunable materials like ferrites and liquid crystals **[28].**

These antennas find applications in wireless and satellite communications, sensing, imaging, and space systems where adaptable RF front ends are required. Christodoulou and al **[28]** emphasize that reconfigurable antennas support modern agile systems including frequency-agile radios (capable of operating across multiple frequency bands), software-defined radios (adaptable via software control and FPGA/microcontroller automation), and cognitive radios (intelligent systems that sense the RF environment and autonomously adapt to congested or contested conditions). The authors note that such systems enable multiband and multistandard operation while improving spectrum utilization. Furthermore, reconfigurable antennas can significantly reduce hardware complexity, component count, and overall system cost compared to conventional architectures employing multiple fixed antennas **[28].**

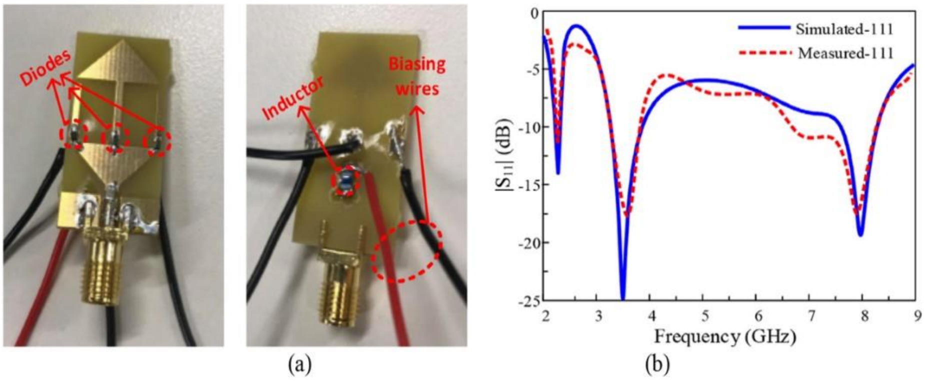

Figure II.17 :(a) Fabricated PIN Diode-Based Frequency-Reconfigurable Antenna Prototype (b)Simulated/Measured Reflection Coefficient $|S_{11}|$ **[29]**.

The switching elements modify the surface current distribution, resulting in multiple operating frequency bands. The measured $|S_{11}|$ results demonstrate good agreement with simulation, confirming the effectiveness of the reconfiguration mechanism **[29]**.

To address the extreme bandwidth demands of future 6G networks, we finally move to THz technology. In our work, this frequency band offers the massive spectrum resources necessary for terabit-per-second data rates.

II.3.4.5. Multiple-Input Multiple-Output (MIMO) Antennas

Multiple-Input Multiple-Output (MIMO) is a wireless communication technology that employs multiple antennas at both the transmitter and receiver ends to enable the simultaneous transmission and reception of multiple data signals over a single frequency channel **(Figure II.18).** This technique marks a significant departure from traditional Single-Input Single-Output (SISO) systems, which use only one antenna at each end and are limited by the capacity of a single channel. MIMO systems follow the high signal-to-noise ratio (SNR) condition and take advantage of multipath propagation by using spatial multiplexing. By utilizing multiple communication paths, MIMO systems can effectively multiply the capacity of a wireless channel without requiring additional power or frequency spectrum. This makes MIMO technology an indispensable component for 6G wireless communication, as it is essential for achieving ultra-high data rates (reaching terabits-per-second), low latency, expanded channel capacity, increased quality and spectral efficiency, reduced multiple fading, low cost, and compact size according to Shannon's capacity theorem**[30]-[31]-[32]-[33]-[34]-[35].**

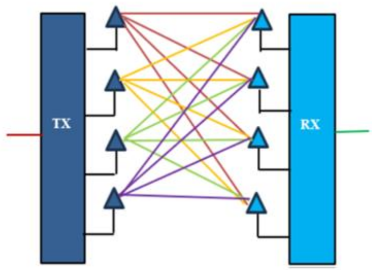

Figure II.18: MIMO communications concept with multiple transmit and receive antennas **[35].**

MIMO technology has different forms, including multi-user (MU-MIMO), single-user (SU-MIMO), and massive MIMO. It offers numerous advantages over single-input single-output (SISO) systems, in which the transmitter and receiver each have a single antenna. The next configuration is single-input multiple-output (SIMO), where the transmitter has a single antenna and the receiver has two antennas; this is known as receiver diversity. In the multiple-input single-output (MISO) system, the receiver has a single antenna while the transmitter has two antennas, a configuration referred to as transmitter diversity. Multi-user MIMO is more advantageous than single-user MIMO, and both multi-user and massive MIMO use multiple antennas at both ends. All four antenna configurations are shown in **Figure II.19 [35].**

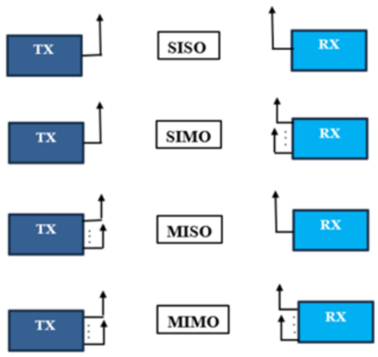

Figure II.19: Four different configurations of antenna **[35].**

II.3.4.5.1. Principle of MIMO Operation

The fundamental principle of MIMO operation involves exploiting the multipath propagation environment to transmit parallel data streams through different spatial paths **[21]-[30]-[36].** Instead of viewing multipath interference as a hindrance, MIMO uses it to increase network capacity through spatial multiplexing, which divides a high-rate data stream into multiple lower-rate streams transmitted simultaneously. To improve signal reliability, MIMO systems leverage spatial diversity (or diversity gain) by sending the same information through independent fading paths, thereby mitigating the effects of multipath fading. Furthermore, beamforming techniques are often integrated to shape the radiation pattern toward specific users, which minimizes interference and significantly enhances network coverage **[32]-[33]-[36].**

II.3.4.5.2. Different configurations of MIMO

MIMO antenna designs are in different configurations, some of which are shown in **Figure II.20**, such as 2×2, 3×3, 4×4, and 8×8. MIMO increase in connection speeds compared to the SISO antenna. MIMO antenna transmits high data throughout the same spectrum resources. Modern devices use 2×1 or 2×2 for low-frequency cellular bands, and 4×4 or 8×8 for mid- and high-frequency bands, but with different performance metrics for different configurations of MIMO **[35].**

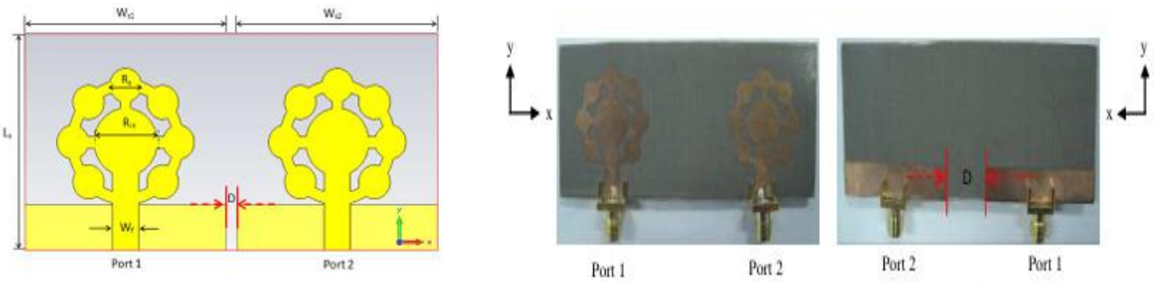

(a)

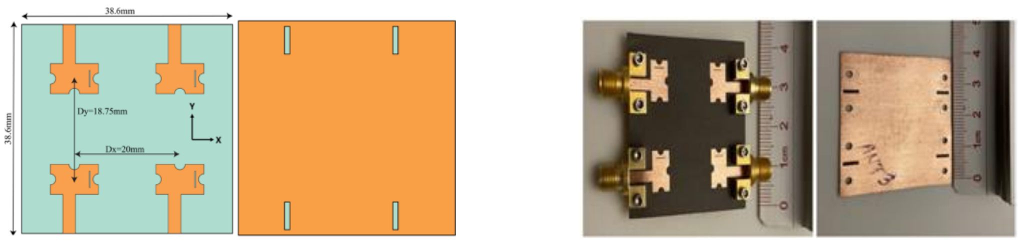

(b)

Figure II.20: The simulated and the fabricated geometry of the proposed MIMO **a)** UWB MIMO antenna from Front view and Back view, **b)** Dual-band MIMO antenna **[37] [38].**

II.3.4.5.3. MIMO Antenna Parameters

The performance of a MIMO antenna system is evaluated using several important parameters that describe the interaction and efficiency of the antenna elements **[31]- [32]- [34]-[35].**

a) Envelope correlation coefficient (ECC)

The envelope correlation coefficient (ECC) measures the correlation between antenna radiation patterns in a MIMO system. It measures antenna independence. For optimal performance, the ECC should be close to zero or < 0.5 in high-performance designs, signifying high diversity, whereas higher ECC values indicate considerable correlation and reduced system efficiency. Wireless communication requires ECC for high data speeds and reliable signal transmission in MIMO systems. To determine the ECC between any number of elements, one can use the radiation field pattern and S-parameters as:

$$ECC = \frac{|\mathbf{S}_{ii}^{*}\mathbf{S}_{ij} + \mathbf{S}_{ji}^{*}\mathbf{S}_{jj}|^2}{\left(1-|\mathbf{S}_{ii}|^2 - |\mathbf{S}_{ji}|^2\right)\left(1-|\mathbf{S}_{jj}|^2 - |\mathbf{S}_{ij}|^2\right)} \quad \textbf{(Eq II.1)}$$

$\mathbf{S}_{ii}, \mathbf{S}_{jj}$: Reflection coefficients of antennas $i$and j, $\mathbf{S}_{ij}, \mathbf{S}_{ji}$: Transmission (mutual coupling) coefficients between antennas

b) Diversity gain (DG)

Diversity Gain (DG) describes how employing multiple antennas or transmission paths in a communication system can improve signal quality and reliability. It measures how diversity techniques, such as spatial, frequency, or polarization diversity, enhance the received signal strength and reduce signal fading. Diversity gain represents the performance improvement obtained by mitigating multipath fading and improving signal reception, and it is typically expressed in decibels (dB). For efficient MIMO systems, the DG should be high (approximately 10 dB) within the operating frequency band. DG is also dependent on the S-parameters and can be calculated as:

$$DG = 10\sqrt{1 - ECC^2} \quad \textbf{(Eq II.2)}$$

c) Mean effective gain

Mean Effective Gain (MEG) is defined as the ratio of the power received by the MIMO antenna to the power received by an isotropic antenna. The MEG is calculated by using **Eq. (3)** and **Eq. (4)**, where i and j indicate antenna port.

For better diversity performance of a MIMO antenna with an equal power level, the range between value $MEGi$ values from -3 dB to -12 dB and the power ratio between the ports MEG_s=MEG_i−MEG_jshould be less than 3 dB. The results show good diversity performance.

$$MEG_i = 0.5[1-|S_{ii}|^2-|S_{ij}|^2] \quad \textbf{(Eq II.3)}$$

$$MEG_j = 0.5[1-|S_{ij}|^2-|S_{jj}|^2] \quad \textbf{(Eq II.4)}$$

Factor 0.5: Accounts for equal probability of incoming waves from all directions in a uniform multipath environment.

d) Channel Capacity Loss (CCL)

Channel Capacity Loss (CCL) is a key parameter for MIMO antenna efficiency. Measure the Channel Capacity Limit to see if a channel can transfer data uninterrupted. MIMO system channel capacity grows proportionally with antenna element count. Correlation between

MIMO channels causes capacity losses. MIMO channel capacity must be measured using the CCL or Channel Capacity Loss when there is a correlation. This can be determined using:

$$CCL = -\log_2 \det(P_R)$$

The receiver two-port correlation matrix can be determined by: **(Eq II.5)**

$$P_R = \begin{bmatrix} \rho_{ii} & \rho_{ij} \\ \rho_{ji} & \rho_{jj} \end{bmatrix}$$

Where:

$$\rho_{ii} = 1 - \left(|S_{ii}|^2 + |S_{ij}|^2\right) \quad \textbf{(Eq II.6)}$$

$$\rho_{jj} = 1 - \left(|S_{jj}|^2 + |S_{ji}|^2\right) \quad \textbf{(Eq II.7)}$$

$$\rho_{ij} = |S_{ii}^* S_{ij} + S_{ji}^* S_{jj}|^2 \quad \textbf{(Eq II.8)}$$

$$\rho_{ji} = |S_{jj}^* S_{ji} + S_{ij}^* S_{jj}|^2 \quad \textbf{(Eq II.9)}$$

The symbols (i) and (j) represent the coefficients corresponding to ports 1 and 2, respectively. According to CCL performance guidelines, the channel capacity loss should be maintained below 0.5 bps/Hz, with values under 0.4 bps/Hz typically regarded as optimal for efficient MIMO operation.

e) Total Active Reflection Coefficient (TARC)

The Total Active Reflection Coefficient (TARC) is the ratio of the total reflected power from the radiating elements to the total incident power on the patch. The TARC value for the MIMO antenna should be below -10 dB in the operating frequency bands to show its excellent performance. The relation between TARC and the S-parameter is described in Eq. **(Eq II.10). In** a MIMO system TARC value is less to prove good diversity performance and reflect higher transfer rates with better data quality.

$$TARC = \frac{\sqrt{\left(S_{ii}+S_{ij}e^{-j\theta}\right)^2+\left(S_{ji}+S_{jj}e^{-j\theta}\right)^2}}{\sqrt{N}} \quad \textbf{(Eq II.10)}$$

Where i and j are the port numbers, denotes the phase angle between two ports, and N is the number of radiating elements.

f) Transmission coefficient (S_{21})

In the context of Multiple-Input Multiple-Output (MIMO) antenna systems, the transmission coefficient, which is also known as isolation, is an essential performance statistic that must be considered. It provides a quantitative measure of the degree of reciprocal coupling or unwanted signal leakage that occurs between the elements of the antenna, with lower values (in decibels) which indicate improved isolation and decreased interference. In MIMO systems, high isolation is required to guarantee that signals sent or received by one antenna element do not adversely affect other elements. This helps to maintain the integrity of the signals and improves the overall performance of the system **[33]**.

II.3.4.5.4. Challenges and Optimization Methods in MIMO Antenna Design

The design of Multiple-Input Multiple-Output (MIMO) antennas for future 6G networks faces significant challenges, primarily centered on mutual coupling, where electromagnetic waves from one antenna interfere with another through near-field, surface wave, or free space interaction. This phenomenon is particularly problematic in compact mobile devices where limited space forces antennas into close proximity, leading to pattern correlation and degraded system efficiency. Additionally, the transition to Terahertz (THz) frequencies introduces extreme path loss and high energy attenuation, requiring antennas with high gain and radiation efficiency to maintain link stability.

To overcome these obstacles, researchers implement several advanced solution techniques tailored for high-frequency performance **(Figure II.21)** such us neutralization line and slots, line resonator, Defected Ground Structures (DGS) involve etching specific slots, such as "I"-shaped or circular patterns, into the ground plane to disrupt surface wave propagation; this technique has been utilized extensively by researchers such as Md Ashraful Haque et al **[36]**, demonstrating that modifying the return current distribution can significantly enhance impedance matching and bandwidth. Parasitic Decoupling Structures (PDS) and elements, integrated by Jamal Hossain Nirob et al. and Haque et al, create compensating coupling paths that cancel out unwanted interference **[30]-[34].** Physical decoupling walls made of materials like silicon, graphene, or polyimide act as electromagnetic barriers between elements were implemented and demonstrated by Md Ashraful Haque and his various research teams, which included co-authors such as Jamal Hossain Nirob, Isha Das, and Kamal Hossain Nahin **[31]-[33]-[36]**. Machine Learning (ML) Optimization has revolutionized the design cycle, with authors such as Uruj Jaleel and MohitShrivastav, Masuod Ghasemi, and Haque et al. using supervised regression algorithms like Extra Trees, Random Forest, and XGBoost (see **Figure II.22**) to predict antenna performance with up to 99% accuracy, thereby bypassing time-consuming and computationally intensive full-wave simulations **[36]-[39]- [40].**

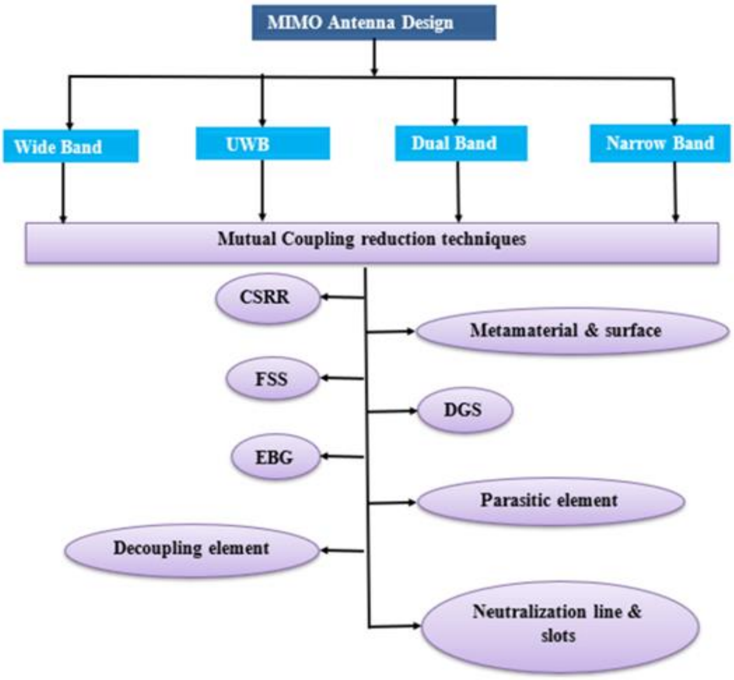

Figure II.21: Mutual coupling reduction techniques **[35].**

Additionally, Metamaterial and frequency selective surface (FSS) are important MC techniques used to reduce the size of MIMO, enhance isolation with high gain, envelope correlation coefficient (ECC), and wide bandwidth,Liton Chandra Paul et al., who designed a slotted metamaterial microstrip patch antenna. This research focused on creating specific triangular slots on the antenna's patch and ground plane to achieve significant bandwidth enhancement and notable size reduction **[36]**.

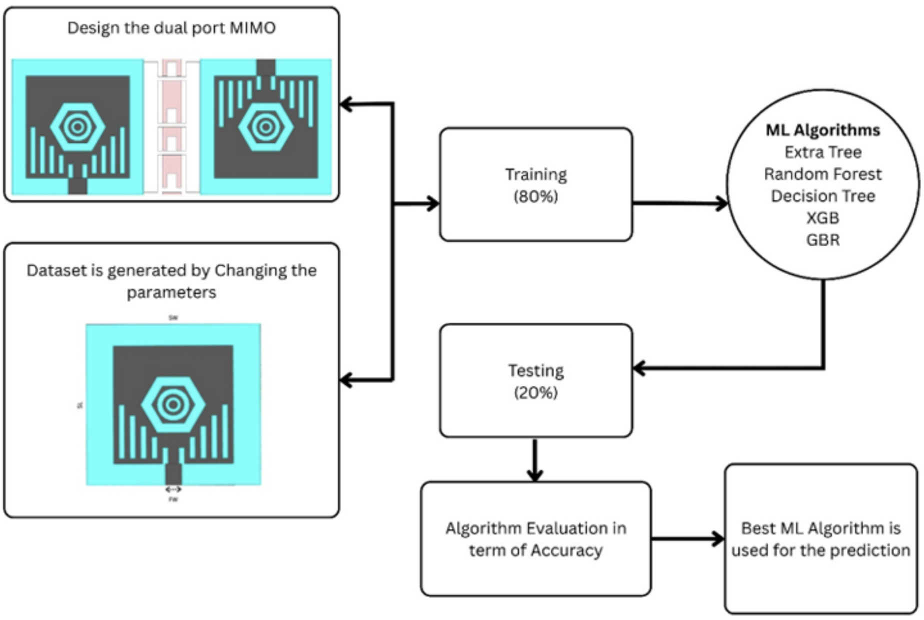

Figure II.22: Machine Learning Workflow for Dual Port MIMO Antenna Design [**34]**

II.4. Overview of Terahertz antennas for 6G Systems

II.4.1. What is the Terahertz (THz) Band?

The Terahertz (THz) band refers to the region of the electromagnetic spectrum spanning frequencies from 0.1 to 10 THz (10^{12} Hz) **[39]**, which corresponds to wavelengths ranging from 3 mm to 30 μm. This frequency range lies between the microwave and infrared regions of the electromagnetic spectrum. Because of this intermediate position, the THz band forms a bridge between conventional electronic technologies, typically used for microwave signal generation, and photonic technologies, commonly employed in infrared and optical systems. For this reason, this spectral region has historically been referred to as the "THz gap," reflecting the technological challenges associated with efficiently generating, detecting, and processing electromagnetic waves within this frequency range. While some standards, including those referenced by the IEEE, define the THz band more strictly as 0.3–10 THz, researchers also frequently consider the sub-THz region (100–300 GHz) due to its increasing importance for the development of future high-capacity wireless communication systems such as 6G networks. **FigureII.23** shows the position of the THz band within the electromagnetic spectrum **[41]- [42]-[43]- [44]-[45].**

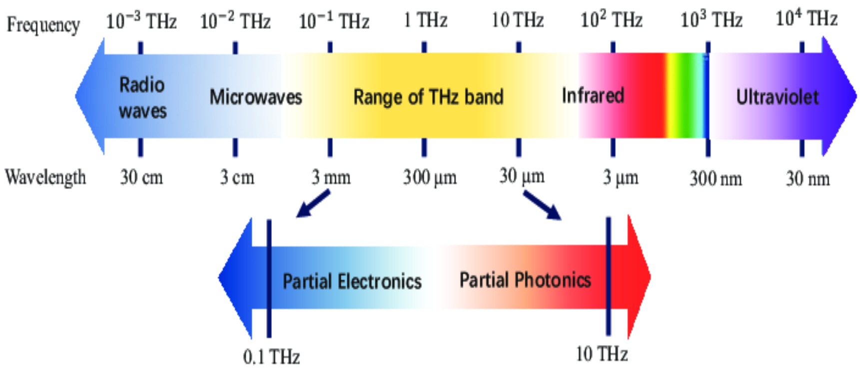

Figure II.23: The position of THz band between the microwave and far-infrared electromagnetic spectrum **[46].**

II.4.2. Advantages THz Communication

THz waves have the following excellent advantages **[47]**:

- **Low damage:**

  The energy of a single THz photon is much lower than that of X-rays, making it safe for biological tissues. Because it does not significantly harm organs, it can be applied in biomedical fields, for example scanning the human body to detect skin cancer and assist in medical diagnosis**.**

- **High spectral resolution:** Many molecules naturally resonate in the THz range, allowing material identification. This is useful for detecting viruses, explosives, and hazardous chemicals.
- **Visualization:** THz waves penetrate non-metallic materials (clothing, paper, plastics) while producing clear images due to their short wavelength. Applications include airport security scanners.
- **Wide bandwidth:** As one of the highest frequency ranges in electronics, THz enables extremely high data capacity and transmission speeds for future wireless communications**.**

II.4.3. Applications for THz Technology

The distinct properties of THz frequencies enable a broad range of applications across multiple sectors, particularly in enhancing 6G wireless communication technologies **(see Figure II.24**) **[41]- [42]- [48]**:

- **High-Speed Wireless Communications:** THz technology enables ultra-high-speed wireless transmission because of its extremely large available bandwidth. It supports data-intensive applications such as the Internet of Things (IoT), augmented reality, and smart connected devices. Due to rapid attenuation and short propagation distance, THz waves are particularly suitable for short-range, high-data-rate links while reducing long-range interference.
- **Network Densification:** THz waves are well suited for dense small-cell deployments in urban areas because their limited propagation and strong attenuation through obstacles reduce interference, allowing networks to handle high traffic and user density more efficiently**.**
- **Secure Communications:** The short range and highly directional nature of THz waves make interception difficult unless directly aligned with the transmission path, providing enhanced security and making them suitable for sensitive military and governmental communications**.**
- **Imaging and Sensing:** In security inspections, THz waves can detect weapons or other dangerous objects under clothing without the health risks associated with ionizing radiation such as X-rays. Additionally, THz imaging is being explored for its potential in medical diagnostics, where it could provide new noninvasive methods for imaging cancer or monitoring wound healing.

- **Spectroscopy and Materials Characterization:** THz waves interact with molecular vibrations, enabling spectroscopic analysis in chemistry and biology for material composition identification, impurity detection, biochemical process observation, and pharmaceutical quality control such as coating thickness and uniformity assessment**.**
- **Food Industry:** THz spectroscopy is applied for contaminant detection, moisture analysis, adulteration identification, and drying process monitoring. It provides non-destructive, real-time detection and is highly sensitive to water content in food products.
- **Scientific Research and Astronomy:** THz technology is used to observe molecular clouds, star-forming regions, and cold celestial bodies. It penetrates dust and gas that block visible light, identifies complex organic molecules in space, and probes quantum states in materials like superconductors and semiconductors at low temperatures.

Figure II.24: Terahertz technology applications **[48]**.

These applications show that THz systems can support both communication and sensing, which is important for future 6G networks **[48].**

II.4.4. Challenges in THz Antenna Design

Despite the promising capabilities of terahertz (THz) technology, the design of THz antennas faces several important challenges. The main issues encountered in THz antenna design include the following **[47]-[48]**and **[49]:**

- **High propagation loss:** THz waves are strongly absorbed by molecules in the atmosphere, which limit transmission distance and coverage**.**

- **Miniaturization and fabrication difficulty:** THz antennas operate at very high frequencies, their dimensions are extremely small, making precise fabrication challenging**.**
- **Surface wave effects in dielectric antennas:** Energy can be trapped in the substrate, reducing radiation efficiency and overall antenna performance.
- **Material limitations and packaging complexity:** Conventional materials often perform poorly at THz frequencies, and integrating antennas into systems is complicated by size and thermal issues.
- **Balancing many requirements:** A good THz antenna must achieve all of these at once**:** High efficiency with low loss, Wide bandwidth for high data rates, Small size for easy integration, Good thermal management, High gain with directional radiation, Low-cost production for mass use**.**

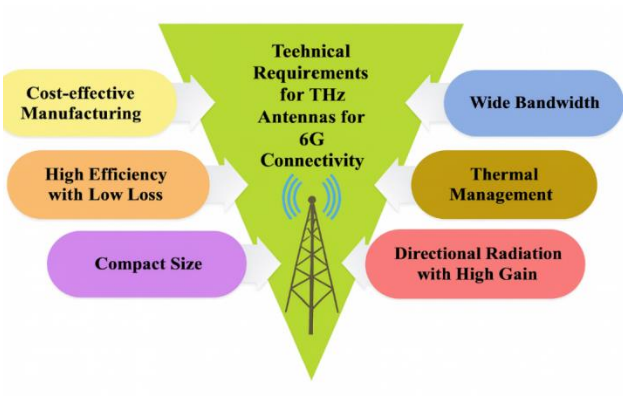

Figure II.25: Technical requirements for THz antennas **[48].**

II.5. Conclusion

The motivation for this work stems from the challenges of designing antennas for 6G systems. Operating at high-frequency bands such as mm-Wave and sub-THz, antennas become extremely small, making performance sensitive to design variations. Modern devices demand antennas that are compact, with wide bandwidth, high gain, high efficiency, and stable radiation patterns, which are difficult to achieve using traditional trial-and-error methods. Full-wave simulators HFSS, while accurate, are computationally intensive for parametric studies and optimization. This motivates the use of intelligent optimization algorithms and prediction models to rapidly estimate performance and find optimal designs. This work proposes a framework combining compact 2×2 MIMO antenna design, optimization, and prediction to efficiently address these challenges for 6G applications.

.

Bibliography of chapter II

[1]. M. H. Tsoi and S. W. Y. Mung, "Planar Antenna Design for Internet of Things Applications," in Smart Antennas: Recent Trends in Design and Applications, ser. Advances in *Computing Communications and Informatics*, vol. 2. Singapore: Springer, pp. 1–20. ISBN: 978-981-15-8881-0,23 September 2020.

[2]. R. H. Abdullah and K. F. Ahmed, "Design of rectangular-shaped microstrip patch antennas for millimeter wave bands," *Journal of University of Duhok*, vol. 23, no. 2, pp. 432, Special Issue, ISSN: 1812-7568, 2020.

[3]. R. Mishra, "An overview of microstrip antenna,", *HCTL Open Int. J. Technol. Innov. Res. (IJTIR)*, vol. 21, no. 2, pp. 6–11, e-ISSN: 2321-1814, ISBN (Print): 978-81-932623-1-3, Aug. 2016.

[4]. https://www.researchgate.net/figure/Microstrip-patch-antenna_fig1_345339399

[5]. https://jemengineering.com/blog-microstrip-antennas-the-basics/

[6]. C. Cherukuri, "Analysis of Coaxial Fed U-Slot Patch Antennas Using Finite Difference Time Domain Method", *M.S. thesis, Dept. of Electrical Engineering,* University of South Florida, Tampa, FL, USA, pp. 19–21, 2002.

[7]. N. Parmar, M. Saxena, and K. Nayak, "Review of Microstrip Patch Antenna for WLAN and WiMAX Application," *Int. J. Eng. Res. Appl.*, vol. 4, no. 1, pp. 170, ISSN: 2248-9622, Jan. 2014.

[8]. P. K. Malik, P. Kumar, S. Kumar, and D. Singh, "Smart Antennas", *Recent Trends in Design and Applications*, vol. 2, *Advances in Computing Communications and Informatics*, pp. 4–8. Sharjah, UAE: Bentham Science Publishers, ISBN: 978-1-68108-859-4, 2021.

[9]. P. K. Malik, S. Padmanaban, and J. B. Holm-Nielsen, Eds., "Application of microstrip antennas," in *Microstrip Antenna Design for Wireless Applications*, 1st ed., vol. 1. Boca Raton, FL, USA: CRC Press, p. 11. ISBN: 978-0-367-55438-5, 2021.

[10]. A. Kaur and P. K. Malik, "Adoption of Micro-Strip Patch Antenna for Wireless Communication: Opportunities and Challenges," *International Journal of Electronics, Communications, and Measurement Engineering (IJECME)*, vol. 10, no. 1, pp. 3, 2021.

[11]. G. Singh and J. Singh, "Comparative analysis of microstrip patch antenna with different feeding techniques," in *Proc. Int. Conf. Recent Adv. Future Trends Inf. Technol. (iRAFIT2012)*, Int. J. Comput. Appl. (IJCA), pp. 18-19, ISSN: 0975-8887, 2012.

[12]. S. Bisht, S. Saini, V. Prakash, and B. Nautiyal, "Study the various feeding techniques of microstrip antenna using design and simulation using CST Microwave Studio," *Int. J. Emerg. Technol. Adv. Eng.*, vol. 4, no. 9, pp. 329–330, ISSN: 2250-2459, Sep. 2014.

[13]. A. J. Sangster, “Compact Slot Array Antennas for Wireless Communications”, *1st ed. Cham, Switzerland: Springer.* ISBN: 978-3-030-01752-1, 2018.

[14].https://www.researchgate.net/figure/Schematic-of-the-PIFA-Antenna-2_fig1_332834425

[15]. D. M. Pozar, “Microwave Engineering”, *4th ed. Hoboken, NJ, USA: Wiley.* ISBN: 978-0-470-63155-3, 2011.

[16].https://www.dvidshub.net/image/750372/loaded-folded-slot-antenna-47-gh

[17]. T. Agarwal, "WireAntenna: Design, Working, Types & Its Applications," *ElProCus,*2023.[Online].Available:https://www.elprocus.com/wire-antenna-design-working-types-its-applications/

[18]. Balanis, C. A, “Antenna theory: Analysis and design, 4th ed., pp. 151–520. Wiley. ISBN: 978-1-118-64206-1, 2016.

[19].https://www.researchgate.net/figure/Photograph-of-the-printed-monopole-antenna-fabricated-on-a-4050mm2-single-layer-FR-4_fig16_258383573

[20].https://www.researchgate.net/figure/Realization-of-fat-dipole-antenna-Antenna-is-designed-and-realized-on-a-FR4-substrate_fig3_269326459

[21]. Janaswamy, “Propagation and Smart Antennas for Wireless Communications”, *R., Radiowave,* vol. 599*, Springer,* 2001.

[22]. M. M. Rahman, Y. Yang, and S. Dey, "Application of Metamaterials in Antennas for Gain Improvement: A Study on Integration Techniques and Performance," *IEEE Access*, vol, pp.49489-49491, ISSN: 2169-353613, Mar. 2025.

[23]. E. Sandi, B. Maruddani, and N. Khairunisa,“Complementary Split Ring Resonator on the Ground Plane for Wearable Antenna,” in *Proc. 2020 International Conference on Radar, Antenna, Microwave, Electronics, and Telecommunications (ICRAMET)*pp. 67–68, ISBN: 978-1-7281-8922-2, 2020.

[24]. R. K. Saraswat and M. Kumar,“Design and Analysis of Metamaterial Inspired Multiband Antenna for 5G Sub-Six GHz NR Frequency Bands and Wireless Applications,” *M. L. V. Textile & Engineering College, Rajasthan Technical University*, Jul. 15, 2022, pp. 16–17.

[25]. R. J. Mailloux, “Phased Array Antenna Handbook”,*3rd ed. Boston, MA,* USA: Artech House, p. 1, ISBN: 978-1-63081-029-0,2017.

[26].[25].https://www.mdpi.com/1424-8220/22/23/9406

[27]. https://www.researchgate.net/figure/Photographs-of-the-antenna-arrays-a-the-1-7-single-series-fed-taper-antenna-array_fig3_252974486

[28]. C. G. Christodoulou, Y. Tawk, S. A. Lane, and S. R. Erwin, "Reconfigurable antennas for wireless and space applications," *Proc. IEEE*, vol. 100, no. 7, pp. 2250, ISSN: 0018-9219, Jul. 2012.

[29]. T. Tandel and S. Trapasiya, "Reconfigurable antenna for wireless communication: Recent developments, challenges and future,", *Wirel. Pers. Commun.*, vol. 133, no. 2, pp. 769–800, ISSN: 0929-6212, Nov. 2023.

[30]. J. H. Nirob, K. H. Nahin, M. A. Haque, M. S. Ahammed, N. S. S. Singh, R. A. Ananta, M. K. Ahmed, and L. C. Paul, "Dual-band MIMO antenna for wideband THz communication in future 6G applications," , *TELKOMNIKA Telecommunication Computing Electronics and Control*, vol. 23, no. 2, pp. 295–301, ISSN: 1693-6930, Apr. 2025.

[31]. M. A. Haque et al., "Performance improvement of THz MIMO antenna with graphene and prediction bandwidth through machine learning analysis for 6G application," *Results Eng.*, vol. 24, art. no. 103216, pp. 1–8, ISSN: 2590-1230, Oct. 2024.

[32]. P. Kaur, S. Malhotra, and M. Sharma, "A review of isolation techniques for 5G MIMO antennas," *J. Telecommun. Inf. Technol.*, vol. 3, pp. 43–45. ISSN: 1509-4553, 2024.

[33]. M. A. Haque and al., "Graphene based terahertz MIMO antenna with machine learning regression for 6G communications," *Sci. Rep.*, vol. 16, no. 3900, pp. 1–15, ISSN: 2045-2322, 2026**.**

[34]. M. A. Haque et al., "Innovative MIMO antenna for terahertz band 6G communications: Performance evaluation and machine learning integration," *Results Eng.*, vol. 29, pp. 1–17, Art. no. 109284, ISSN: 2590-1230, Mar. 2026.

[35]. J. G, I. Singh, and D. K. Choudhary, “Gain and isolation improvement techniques for MIMO antenna: A compendious survey,” *Results in Engineering*, vol. 25, Art. no. 104482, pp. 1–9, ISSN: 2590-1230, 2025.

[36]. M. A. Haque, K. H. Nahin, J. H. Nirob, R. A. Ananta, N. S. S. Singh, L. C. Paul, A. D. Algarni, M. El-Affendi, and A. A. Ateya, "Machine learning-based novel shaped THz MIMO antenna with a slotted ground plane for future 6G applications," *Sci. Rep.*, vol. 14, art. no. 32162, pp. 1–2, ISSN: 2045-2322, , Nov. 2024.

[37]. M. Jusoh, M. F. Jamlos, M. R. Kamarudin, and F. Malek, “A MIMO antenna design challenges for UWB application,”, Progress*In Electromagnetics Research B*, vol. 36, p. 360, 2012.

[38]. W. T. Sethi, S. H. Kiani, M. E. Munir, D. A. Sehrai, H. S. Savci, and D. Awan, “Pattern diversity based four-element dual-band MIMO patch antenna for 5G mmWave communication networks,” *Journal of Infrared, Millimeter, and Terahertz Waves*, vol. 45, pp. 527–528, 2024.

[39]. U. Jaleel and M. Shrivastav, “Design and optimization of MIMO antenna using machine learning algorithm for IoT applications,” *National Journal of Antennas and Propagation*, vol. 6, no. 3, pp. 37–42, ISSN: 2582-2659, 2024.

[40]. M. Ghasemi, "MIMO antenna optimization for millimeter-wave 5G applications using machine learning," *Discover Electronics*, vol. 2, no. 1, article 58, Jul. 2025.

[41]. A. Shekari, S. S. Seyyed-Afghahi, and A.-A. Ebrahimi, "Applications of terahertz technology: A comprehensive review of advances and future prospects," in *Journey into Terahertz Radiation - Exploring the Invisible Frontier*, J. Li, Ed. London, U.K.: Intech Open, pp. **1–25**, 1 ISBN: 978-0-8054-2999-9, 2025.

[42]. P. Yu *et al.*, "Recent developments and applications of terahertz spectroscopy in food analysis," *Biosensors*, vol. 15, no. 10, art. no. 677, pp. 6–9, ISSN: 2079-6374, 2025.

[43]. M. Zubair, "Development of terahertz antennas for 6G wireless communication," Ph.D. dissertation, School of Engineering, Univ. of Glasgow, Glasgow, U.K,p. 11, 2024.

[44]. R. Jain, V. V. Thakare, and P. K. Singhal, "Design and comparative analysis of THz antenna through machine learning for 6G connectivity," *IEEE Latin Am. Trans.*, vol. 22, no. 2, pp. 82–90, ISSN: 1548-0992, Feb. 2024.

[45]. J. C. F. Zandboer, U. Johannsen, G. Federico, and A. B. Smolders, "A review on antenna technology developments for sub-THz wireless communication: Application, challenges and opportunities," *IEEE Open Journal of Antennas and Propagation*, vol. 6, no. 3, pp. 645–646, ISSN: 2637-6431, Jun. 2025.

[46].https://www.researchgate.net/figure/The-range-of-THz-band-in-the-electromagnetic-spectrum_fig1_368587507.

[47]. Y. He, Y. Chen, L. Zhang, S.-W. Wong, and Z. N. Chen, "An overview of terahertz antennas, », *China Commun.*, vol. 17, no. 7, pp. 124–130, ISSN: 1673-5447, Jul. 2020.

[48]. M. Zubair, "Development of terahertz antennas for 6G wireless communication," Ph.D. dissertation, School of Engineering, Univ. of Glasgow, Glasgow, U.K, pp. 11. 2024.

[49]. S. Alraih, I. Shayea, M. Behjati, R. Nordin, N. F. Abdullah, A. Abu-Samah, and D. Nandi, "Revolution or evolution? Technical requirements and considerations towards 6G mobile communications," *Sensors*, vol. 22, no. 3, pp.762, ISSN: 1424-8220, 2022

Chapter III: Machine Learning in THz Patch Antenna Design

III.1. Introduction

This chapter explores machine learning-based optimization algorithms for designing and improving microstrip patch antennas operating in the terahertz (THz) band for 6G communication systems. Traditional optimization methods using full-wave simulation tools like ANSYS HFSS are often time-consuming and computationally intensive due to the complexity and nonlinearity of antenna designs. To overcome these challenges, machine learning techniques offer faster and more efficient alternatives by learning from simulation data and providing accurate predictions. The chapter reviews several algorithms, including Random Forest, Extra Trees, XGBoost, CatBoost, K-Nearest Neighbors, and Gaussian Process Regression, analyzing their principles, advantages, and limitations.

The main goal is to highlight the effectiveness of these machine learning–based optimization algorithms in enhancing MIMO antenna design performance and to identify the most suitable methods for handling complex optimization problems in THz antenna applications for 6G systems.

III.2. Overview of ML for THz Antenna Optimization

III.2.1. Random Forest (RF)

Random Forest, introduced by Leo Breiman in 2001 **[1]**, is a robust ensemble learning algorithm widely used for modeling complex nonlinear systems. In the context of terahertz (THz) antenna design, it has been successfully applied as an efficient surrogate model for a single antenna to predict key performance parameters such as antenna gain (G), bandwidth, return loss (S_{11}), and radiation efficiency. The algorithm operates by constructing multiple decision trees using bootstrap aggregation, where each tree is trained on a different subset of the dataset, and a random subset of features is selected at each node to determine optimal splits **[1].** The final prediction is obtained by averaging the outputs of all trees for regression tasks, which significantly improves prediction accuracy while reducing overfitting and enhancing generalization **[2].** This approach is then extended to multiple-input multiple-output (MIMO) antenna systems, where additional complexity arises due to mutual coupling (S_{21}), increased design dimensionality, and strict performance requirements. In THz MIMO antenna optimization, Random Forest is particularly valuable because it enables fast prediction of electromagnetic performance without requiring repeated full-wave simulations, which are computationally expensive **[3].** By accurately capturing the nonlinear relationship between design parameters and antenna performance metrics, the model facilitates efficient exploration and optimization of both single and MIMO antenna structures while maintaining robustness against noise, outliers, and incomplete data **[4].**

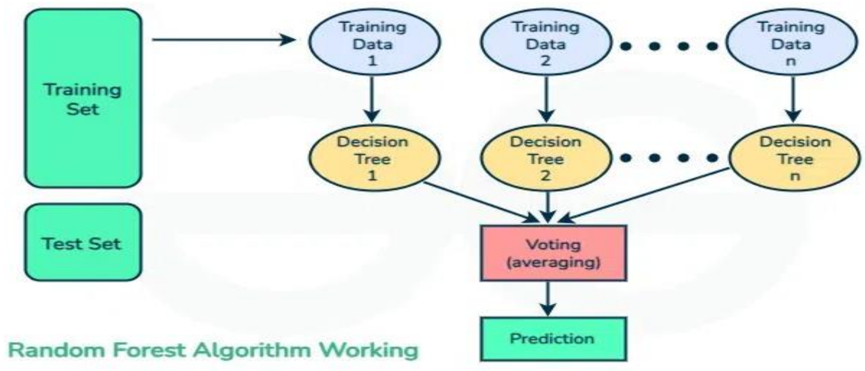

Figure III.1: Workflow of the Random Forest Algorithm **[5].**

The mathematical formulation of a Random Forest prediction for regression is:

$$\hat{y} = \frac{1}{T}\sum_{t=1}^{T} f_t(x) \quad \textbf{(Eq III.1)}$$

Where:

T is the number of trees, $f_t(x)$ is the prediction from the t-th tree, and x is the input feature vector.

In THz microstrip patch antenna design, Random Forest has been employed as a surrogate model to predict antenna performance metrics, allowing exploration of design spaces without repeated full-wave simulations. Thao and Kien **[6]** proposed a hybrid RF-GPR framework to estimate antenna parameters, achieving high accuracy with reduced computational cost. Ranjan et al. **[7]** applied Random Forest to optimize dielectric resonator antennas, showing significant improvements in prediction accuracy for resonance frequency, bandwidth, and gain.

III.2.2. Extra Trees (ET)

Extra Trees (Extremely Randomized Trees), introduced by Pierre Geurts and al. in 2006, is an ensemble learning algorithm that constructs multiple decision trees with a high degree of randomness **[8]**. Unlike Random Forest, which selects optimal split thresholds, Extra Trees randomly chooses both the feature and the split point at each node, leading to reduced variance and improved computational efficiency. The final prediction is obtained by averaging the outputs of all trees for regression tasks. Due to its ability to model complex nonlinear relationships and handle high-dimensional data, Extra Trees is well suited for engineering applications.

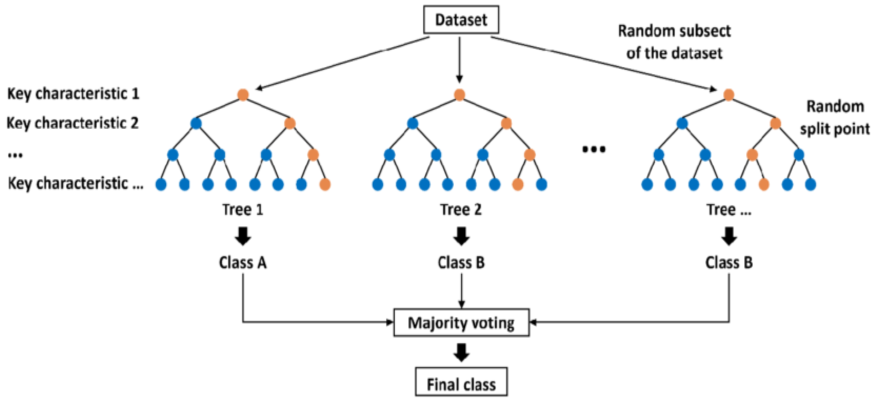

Figure III.2: Extra Trees Workflow with MajorityVoting **[9].**

In terahertz (THz) antenna design, machine learning techniques, including tree-based ensemble methods, have been widely used as surrogate models to predict key performance parameters such as gain, bandwidth, and return loss, significantly reducing the need for computationally expensive full-wave simulations **[10]**. Furthermore, in multiple-input multiple-output (MIMO) antenna systems, these methods enable efficient modeling of mutual coupling and complex parameter interactions, facilitating rapid optimization and improved design performance **[11]**.

III.2.3. XGBoost (Extreme Gradient Boosting)

XGBoost, developed by Chen and Guestrinin 2016 **[12]**, is a gradient boosting algorithm that builds tree sequentially. Each new tree minimizes a regularized objective function to correct errors of previous trees:

$$Obj = \sum_{i=1}^{n} l(y_i, \hat{y}_i) + \sum_{k=1}^{K} \Omega(f_k) \qquad \textbf{(Eq III.2)}$$

Where

l is the loss function, Ω is a regularization term, f_k is the k-th tree, and n is the number of training samples.

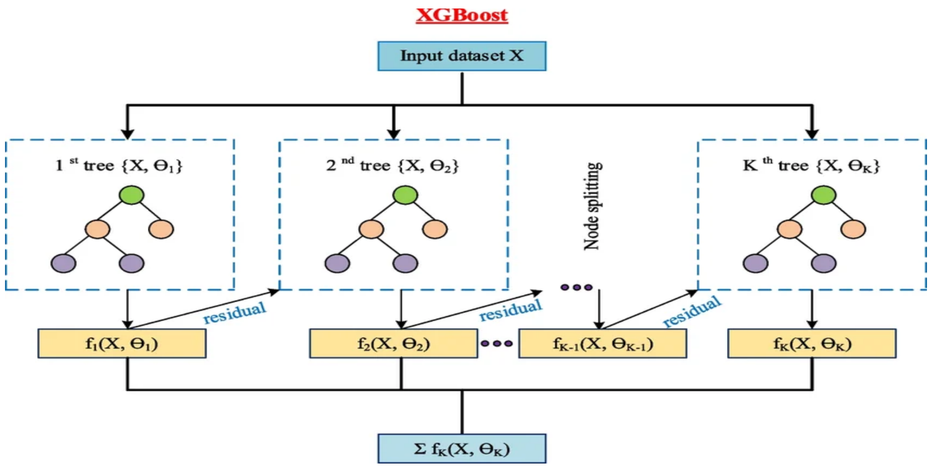

Figure III.3: XGBoost (extreme gradient-boosting) algorithm structure **[13].**

This figure illustrates the working principle of XGBoost, where multiple decision trees are built sequentially to improve prediction accuracy. The first tree generates an initial prediction from the input dataset, while the following trees learn from the residual errors of the previous ones to progressively reduce prediction error. Finally, the outputs of all trees are combined to produce an accurate prediction of antenna performance parameters such as return loss, gain, bandwidth, and radiation efficiency in THz MIMO antenna design for 6G applications.

In the context of terahertz (THz) antenna design, XGBoost has been effectively used as a surrogate modeling tool to predict key performance parameters such as gain, bandwidth, and return loss (S_{11}), significantly reducing the need for time-consuming full-wave electromagnetic simulations **[10]**. Furthermore, for multiple-input multiple-output (MIMO) antenna systems, XGBoost enables accurate modeling of mutual coupling (S_{21}) and high-dimensional parameter interactions, facilitating efficient optimization of antenna configurations. Its ability to handle complex datasets and capture nonlinear relationships makes it a powerful approach for accelerating the design and optimization of THz and MIMO antennas in next-generation wireless communication systems **[11]**.

III.2.4. CatBoost

CatBoost is a gradient boosting algorithm introduced by Liudmila Prokhorenkova et *al.* in 2018, designed to improve prediction accuracy while reducing overfitting through ordered boosting and efficient handling of categorical variables **[14]**. The model builds an ensemble of decision trees sequentially, where the overall prediction function is expressed as:

$$F(x) = \sum_{m=1}^{M} h_m(x) \quad \textbf{(Eq III.3)}$$

Where

$h_m(x)$represents the m-th decision tree and M is the total number of trees. The model is trained by minimizing a loss function, typically the squared error for regression problems:

$$L = \sum_{i=1}^{N} (y_i - F(x_i))^2 \quad \textbf{(Eq III.4)}$$

The boosting process updates the model iteratively as:

$$F^{(t)}(x) = F^{(t-1)}(x) + \alpha\, h^{(t)}(x) \quad \textbf{(Eq III.5)}$$

where

α is the learning rate controlling the contribution of each new tree.

In terahertz (THz) antenna design, CatBoost is employed as a surrogate model to approximate the nonlinear mapping between antenna design parameters (e.g., patch dimensions, substrate permittivity, and feed position) and electromagnetic responses such as resonance frequency, gain, and return loss (S_{11}). This significantly reduces the reliance on computationally intensive full-wave simulations. Moreover, in multiple-input multiple-output (MIMO) antenna systems, CatBoost effectively captures complex interactions such as mutual coupling (S_{21}) and high-dimensional dependencies, enabling efficient multi-parameter optimization. Its robustness and generalization capability make it a promising approach for accelerating the design and optimization of THz and MIMO antennas in next-generation wireless systems **[10]-[11].**

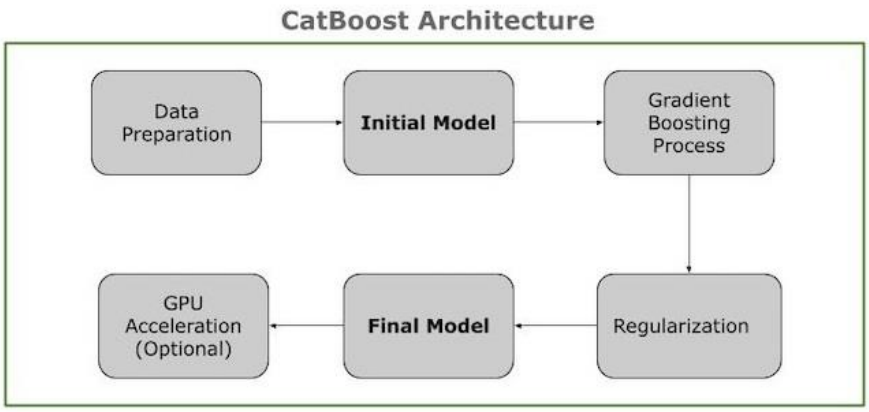

Figure III.4: CatBoost Architecture **[15].**

III.2.5. K-Nearest Neighbors (KNN)

K-Nearest Neighbors (KNN), introduced by Fix and Hodges in 1951 **[16]**, is a simple instance-based learning algorithm. In THz antenna design, KNN approximates the relationship between antenna parameters and performance metrics based on similarity between data points, expressed as $y = f(x)$. The prediction is computed as:

$$\hat{y} = \frac{1}{K} \sum_{i \in N_K(x)} y_i \qquad \textbf{(Eq.III.6)}$$

Where: $N_K(x)$ represents the set of the Knearest neighbors.

In THz applications, KNN is often used as a baseline model for predicting parameters such as gain and resonance frequency when datasets are small. Studies by El Misilmani and Naous and Sarker highlight its usefulness in engineering problems with limited data **[17].**

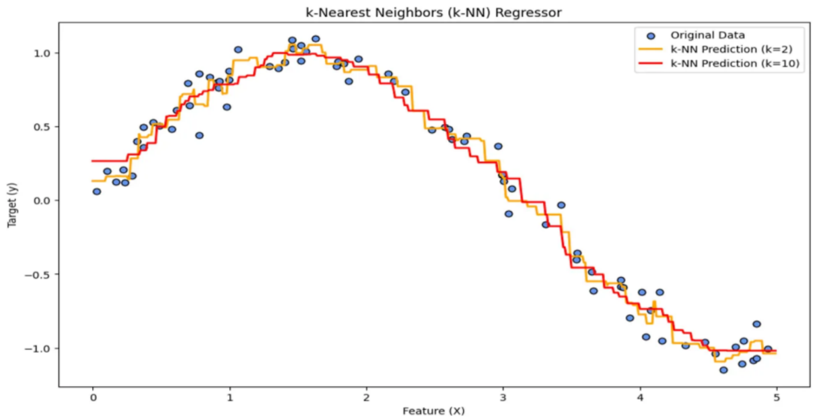

Figure III.5: Effect of k on k-NN Regression **[18].**

In terahertz (THz) antenna design, K-Nearest Neighbors (KNN) is employed as a surrogate modeling technique to approximate the nonlinear relationship between antenna design parameters (e.g., patch dimensions, substrate permittivity, and feed position) and electromagnetic responses such as resonance frequency, gain, and return loss (S_{11}). By leveraging similarity between data samples, KNN enables fast prediction without requiring an explicit training phase, thereby reducing dependence on computationally intensive full-wave simulations. Moreover, in multiple-input multiple-output (MIMO) antenna systems, KNN can effectively capture interactions between antenna elements, including mutual coupling (S_{21}), by exploiting proximity in the feature space. Although its performance depends on dataset quality and size, KNN remains a useful and efficient approach for rapid design space exploration and preliminary optimization of THz and MIMO antennas **[19]– [11]**.

III.2.6. Gaussian Process Regression (GPR)

Gaussian Process Regression (GPR) is a probabilistic, non-parametric regression method based on Bayesian theory **[20]**. In THz microstrip patch antenna optimization, GPR models the nonlinear relationship between antenna design parameters and electromagnetic responses such as resonance frequency, gain, and return loss, expressed as $y = f(x)$. The model assumes a Gaussian process prior:

$$f(x) \sim GP(m(x), k(x, x')) \qquad \textbf{(Eq III.7)}$$

and provides predictions in the form of a probability distribution:

$$\hat{y}(x) \sim \mathcal{N}\left(\mu(x), \sigma^2(x)\right) \qquad \textbf{(Eq III.8)}$$

Where:

$\mu(x)$ is the predicted mean and $\sigma^2(x)$ represents uncertainty. Unlike other machine learning algorithms such as tree-based models or boosting methods, GPR uniquely provides uncertainty quantification along with predictions, making it particularly suitable for problems with limited and expensive data, such as THz antenna design.

In THz and multiple-input multiple-output (MIMO) antenna systems, GPR is widely used as a surrogate model to replace computationally intensive full-wave simulations (e.g., HFSS, CST). Its ability to model complex nonlinear interactions and quantify uncertainty allows efficient exploration of high-dimensional design spaces, accurate prediction of parameters such as gain and mutual coupling (S_{21}), and effective multi-objective optimization **[6].**

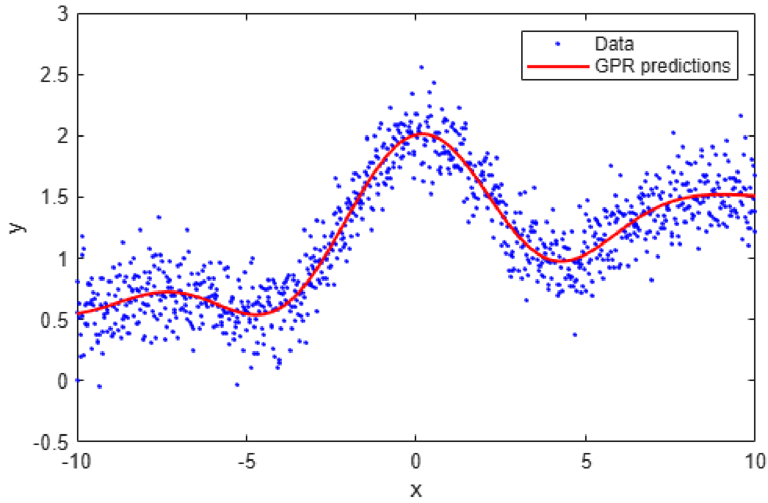

Figure III.6: Gaussian Process Regression Fit to Noisy Data **[21].**

III.3. Comparative Analysis of Machine Learning Algorithms

Ref.	Algorithms Compared	Best Performing Algorithm	Main Findings
[22]	Random Forest, XGBoost, CatBoost, KNN, Gaussian Process, Extra Trees	XGBoost Extra Trees	Ensemble learning methods achieved the highest prediction accuracy for bandwidth and isolation estimation in THz MIMO antennas
[23]	Regression ML models, ensemble learning methods	Gradient Boosting-based models	Boosting algorithms significantly improved prediction accuracy and reduced simulation complexity in THz MIMO antenna optimization.
[24]	Ensemble regression models	Ensemble methods	Advanced ensemble ML approaches demonstrated strong robustness and accurate isolation prediction for THz MIMO antennas.
[25]	Random Forest, XGBoost, CatBoost, ANN	CatBoost	CatBoost achieved superior prediction accuracy and reduced overfitting in antenna efficiency prediction.
[26]	Decision Tree, XGBoost, Gaussian Process Regression	XGBoost	XGBoost provided high accuracy and robust nonlinear modeling for THz antenna parameter prediction.
[27]	Decision Tree, Random Forest, Extra Trees	Random Forest / Extra Trees	Random Forest achieved excellent prediction accuracy and optimization capability for THz MIMO antenna parameters.
[28]	Regression ML models	Ensemble ML models	ML regression approaches achieved high predictive accuracy while reducing full-wave simulation time.

Table III.1: Literature review-based comparison of machine learning techniques for THz MIMO antenna performance prediction.

III.4. Conclusion

This chapter presented an overview of machine learning techniques applied to the optimization of terahertz (THz) microstrip patch antennas. The main focus was on understanding how different algorithms can effectively model the complex relationships between antenna design parameters and their electromagnetic performance. By replacing time-consuming full-wave simulations with efficient predictive models, these techniques enable faster design exploration and optimization in high-frequency applications.

The comparative analysis showed that ensemble tree-based methods, particularly XGBoost and CatBoost, provide the highest prediction accuracy and strong performance in high-dimensional design spaces. K-Nearest Neighbors is mainly suitable for small datasets, while Random Forest and Extra Trees offer a good balance between accuracy and computational efficiency. In addition, Gaussian Process Regression stands out due to its ability to provide both accurate predictions and uncertainty estimation, making it particularly suitable for THz applications where simulation data is limited and expensive.

Machine learning (ML) has become an essential tool in modern antenna engineering because it enables intelligent prediction, optimization, and decision-making with reduced computational complexity. ML algorithms can learn nonlinear electromagnetic behaviors from simulation data and rapidly estimate key antenna parameters such as return loss, gain, bandwidth, and radiation efficiency. As a result, ML-based approaches significantly reduce design time, improve optimization efficiency, and support the development of advanced THz MIMO antennas for future 6G communication systems.

Overall, machine learning techniques significantly accelerate the antenna design process and reduce computational costs, making them essential tools for THz antenna optimization. In the next chapter, the proposed antenna and MIMO system will be implemented and validated using full-wave simulations in HFSS, where the obtained results and performance analysis will be presented and discussed

Bibliography of Chapter III

[1]. L. Breiman, “Random Forests,” *Machine Learning*, vol. 45, no. 1, pp. 5–32, Oct. 2001.

[2]. T. K. Ho, “The Random Subspace Method for Constructing Decision Forests,” *IEEE Transactions on Pattern Analysis and Machine Intelligence*, vol. 20, no. 8, pp. 832–844, Aug. 1998.

[3]. C. Zhang, H. Yang, and Y. Li, “Machine Learning-Based Modeling and Optimization for Terahertz Antenna Design,” *IEEE Access*, vol. 8, pp. 203312–203322, 2020.

[4]. G. James, D. Witten, T. Hastie, and R. Tibshirani, *An Introduction to Statistical Learning*, New York, NY, USA: Springer, 2013.

[5]. What are the Advantages and Disadvantages of Random Forest? - GeeksforGeeks

[6]. N. T. Thao and T. V. Kien, “A Hybrid Random Forest–Gaussian Process Regression Model for Antenna Design Optimization,” *International Journal of RF and Microwave Computer-Aided Engineering*, vol. 30, no. 6, e22187, Jun. 2020.

[7]. R. Ranjan, S. K. Sharma, and A. K. Gautam, “Machine Learning-Based Optimization of Dielectric Resonator Anten.na Parameters Using Random Forest Algorithm,” *IEEE Access*, vol. 9, pp. 110234–110245, 2021

[8]. P. Geurts, D. Ernst, and L. Wehenkel, “Extremely Randomized Trees,” Machine Learning, vol. 63, no. 1, pp. 3–42, Apr. 2006.

[9]. Structure of Extra Trees (Kapoor 2020). Extra Trees constructs the set... | Download Scientific Diagram

[10]. M. A. Khan et al., “Predictive modelling and high-performance enhancement of smart THz antennas for 6G applications using regression machine learning approaches,” Scientific Reports, vol. 15, 2025.

[11]. S. Jorwal, S. Singh, and S. Agarwal, “Design of graphene-based terahertz absorber and machine learning prediction model,” Optics Communications, vol. 554, Art. no. 130203, 2024.

[12]. T. Chen and C. Guestrin, “XGBoost: A scalable tree boosting system,” in Proc. 22nd ACM SIGKDD Int. Conf. Knowledge Discovery and Data Mining (KDD), San Francisco, CA, USA, pp. 785–794, 2016.

[13].https://www.researchgate.net/figure/The-XGBoost-algorithm-structure_fig4_378851394

[14]. L. Prokhorenkova, G. Gusev, A. Vorobev, A. V. Dorogush, and A. Gulin, "CatBoost: Unbiased boosting with categorical features," in Advances in Neural Information Processing Systems (NeurIPS), vol. 31, 2018.

[15].https://www.tutorialspoint.com/catboost/catboost-architecture.htm

[16]. I. H. Sarker, "Machine learning:Algorithms, real-world applications and research directions," SN Computer Science, vol. 2, no. 3, 2021.

[17]. H. M. El Misilmani and T. Naous, "Applications of machine learning in antennadesign: A review," IEEE Access, vol. 11, pp. 103890–103915, 2023.

[18].https://medium.com/@arzuh94a/k-nearest-neighbors-knn-vs-support-vector-machines-svm-a-comprehensive-comparison-e16d22e6f377

[19]. E. Fix and J. L. Hodges, "Discriminatory Analysis, Nonparametric Discrimination: Consistency Properties," USAF School of Aviation Medicine, Randolph Field, TX, USA, Tech. Rep. 4, 1951.

[20]. C. E. Rasmussen and C. K. I. Williams, *Gaussian Processes for Machine Learning*, Cambridge, MA, USA: MIT Press, 2006.

[21].https://ww2.mathworks.cn/help/stats/fitrgp.html

[22]. M. S. Sharawi, A. M. Alibakhshikenari, B. S. Virdee, and E. Limiti, "Machine learning based dual-band circular MIMO antennas for high-performance 6G IoT system," Array, vol. 24, p. 100390, 2025.

[23]. A. K. Verma, S. Singh, and R. Kumar, "Machine learning-based novel-shaped THz MIMO antenna with a slotted ground plane for future 6G applications," Scientific Reports, vol. 14, no. 1, p. 79332, 2024.

[24]. M. A. Rahman, M. T. Islam, and M. Samsuzzaman, "Regression supervised model techniques THz MIMO antenna for 6G wireless communication and IoT application with isolation prediction," Array, vol. 22, p. 100361, 2024.

[25]. S. K. Patel, A. Sharma, and P. K. Singhal, "Meta learner-based optimization for antenna efficiency prediction and high-performance THz MIMO antenna applications," Array, vol. 25, p. 100421, 2025.

[26]. R. K. Gupta, V. Sharma, and N. Kumar, "High-performance quatrefoil-slotted THz MIMO antenna for 6G applications with regression-based machine learning validation," Scientific Reports, vol. 15, no. 1, p. 28657, 2025.

[27]. M. H. Islam, M. T. Islam, and M. Samsuzzaman, "Machine learning validation in performance evaluation to optimize 6G terahertz MIMO antenna designs for future wireless networks," SN Applied Sciences, vol. 8, no. 2, p. 8313, 2026.

[28]. S. R. Hasan, M. A. Hossain, and M. T. Islam, "High-performance terahertz MIMO antenna for 6G: Graphene integration and machine learning prediction," Materials Today Communications, vol. 42, p. 110239, 2025.

Chapter IV: Design, Simulation and Optimization

IV.1.Introduction

This chapter presents the simulation and performance evaluation of a microstrip patch antenna operating at terahertz (THz) frequencies using ANSYS HFSS 2024. The study is centered around a target frequency of 0.3 THz, within a broader analysis range extending from 0.1 THz to 0.95 THz, in order to assess the antenna behavior across the THz spectrum relevant for 6G applications.

The antenna design is first modeled and simulated as a single-element structure, where key performance parameters such as reflection coefficient (S_{11}), bandwidth, gain, and radiation characteristics are analyzed. Following this, the work is extended to Multiple-Input Multiple-Output (MIMO) configurations, including 2×2, to evaluate improvements in performance metrics such as isolation, mutual coupling, and overall system efficiency.

In addition, a machine learning–based optimization approach is applied to enhance the antenna performance by adjusting geometrical parameters and improving key characteristics. All simulations are carried out using the full-wave electromagnetic solver in HFSS 2024 to ensure accurate and reliable results at THz frequencies.

This chapter provides a comprehensive analysis of the proposed designs and demonstrates their suitability for advanced 6G communication systems.

IV.2. Simulation Environment: Ansys HFSS

This work describes antenna design and simulation with ANSYS HFSS, an industry leading 3D electromagnetic (EM) simulation tool for high frequency and high-speed electronic components. **Figure IV.1** highlights several antenna-related applications with emphasis on antennas on or around other structures. With multiple simulation technologies and powerful automated adaptive mesh refinement providing gold standard accuracy, HFSS can help antenna designers who are constantly challenged with implementing designs across more and more frequency bands inside a smaller and smaller footprint. With these additional technical challenges along with the ever-shrinking time to market, simulation with HFSS is a must-have in the antenna design and integration process. Miniaturization of the antennas, limited channel bandwidth, reduced design time, and antenna interaction with other components present stiff challenges to the design engineer. HFSS provides automatic, accurate, and efficient solutions to overcome these challenges, making it the ultimate tool of choice for antenna simulation. A variety performance characterization such as return loss, input impedance, gain, directivity and a variety of polarization characteristics can be analyzed in HFSS.

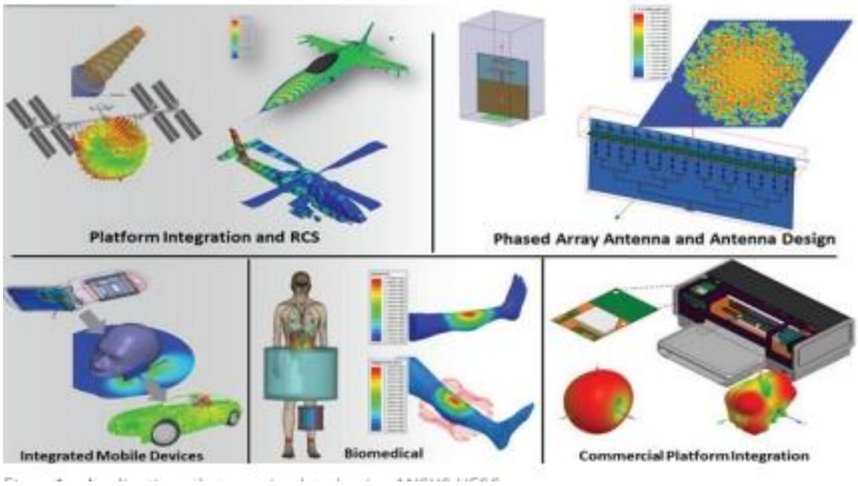

Figure IV.1: Applications that are simulated using ANSYS HFSS **[3]**.

The ability to overlay the 3D far-field pattern on the antenna geometry can provide the designer invaluable insight and direct correlation between the antenna and the resulting radiation pattern. HFSS also offers electric and magnetic field visualization both in the near-field and far-field providing design understanding that is not easily available through measurement **[3]**.

IV.3. Different stages of designing a single-element antenna

IV.3.1. Antenna Design Specifications and Materials

The proposed microstrip patch antenna is designed for terahertz (THz) operation at a central frequency of 0.3 THz, within a wide range of 0.1 THz to 0.95 THz, targeting future 6G communication systems.

The antenna is implemented on a polyimide substrate, selected for its low dielectric loss and stable high-frequency performance. It has a relative permittivity of $\varepsilon_r = 3.3$ and a thickness of h = 25µm, providing a suitable balance between compactness and electromagnetic efficiency at THz frequencies **[4]-[5]**.

The conductive layers were modeled using an ENIG (Electroless Nickel Immersion Gold) metallization stack to reflect practical fabrication conditions, consisting of copper (Cu) as the primary conductor ($\sigma_{Cu} = 5.8 \times 10^7$ S/m), nickel (Ni) as a diffusion barrier ($\sigma_{Ni} = 1.4 \times 10^7$ S/m), and gold (Au) as the outer oxidation-resistant layer ($\sigma_{Au} = 4.1\times 10^7$ S/m); at THz frequencies, surface currents are mainly confined to the outer conductive layer due to the skin effect **[6].**

IV.3.2. Theoretical Calculations

The dimensional design follows a systematic theoretical approach based on the transmission line model of microstrip antennas, beginning with the operating frequency specification and proceeding through substrate characterization to the determination of all physical dimensions **[7].**

Step 1: Operating Frequency and Substrate Selection

$$f_0 = 0.3\ \text{GHz}, \varepsilon_r = 3.3, h_s = 25\ \mu m$$

Step 2: Patch Width Calculation

The patch width is determined by: $W_p = \frac{c_0}{2f_0}\sqrt{\frac{2}{\varepsilon_r+1}}$ =520 μm **(Eq IV.1)**

Where $c_0 = 3 \times 10^8$ m/sis the free-space velocity of light and ε_r is the dielectric constant of the material.

Step 3: Effective Dielectric Constant

The effective dielectric constant accounts for fringing fields extending into air:

$$\varepsilon_{reff} = \frac{\varepsilon_r + 1}{2} + \frac{\varepsilon_r - 1}{2}\left(1+12\frac{h_s}{W_p}\right)^{-1/2} \quad \textbf{(Eq IV.2)}$$

Where h_s and W_p are the substrate height and patch width, respectively.

Step 4: Patch Length Calculation

The effective length including fringing effects: $L_{eff} = \frac{c}{2f_0\sqrt{\varepsilon_{reff}}}$ **(Eq IV.3)**

Fringing length correction: $\Delta L = 0.412 h_s \cdot \frac{(\varepsilon_{reff}+0.3)\left(\frac{W_p}{h_s}+0.264\right)}{(\varepsilon_{reff}-0.258)\left(\frac{W_p}{h_s}+0.8\right)}$ **(Eq IV.4)**

Physical patch length: $L_p = L_{eff} - 2\Delta L$= 466 μm **(Eq IV.5)**

Step 5: Ground Dimensions

The ground plane dimensions for the antenna are calculated as: $W_g = W_p + 6h_s$ **(Eq IV.6)**

$$L_g = L_p + 6h_s \quad \textbf{(Eq IV.7)}$$

Step 6: Feed Line Design (50 Ω)

For a microstrip line with: $Z_0 = \frac{60}{\sqrt{\varepsilon_{reff}}} \ln\left(\frac{8h_s}{W_f} + \frac{W_f}{4h_s}\right)$ **(Eq IV.8)**

Solving for $W_f = 40\ \mu m$ with $h_s = 25\ \mu m$ yields: $Z_0 \approx 50\ \Omega$ This ensures proper impedance matching to the source **[7]**.

Based on these calculations, the initial geometry is defined and later optimized. The final dimensions are $W_p = 525\ \mu m$, $L_p = 440\ \mu m$, $W_f = 40\ \mu m$, and $W_g = L_g = 800\ \mu m$, ensuring good matching and efficient radiation at 0.3 THz.

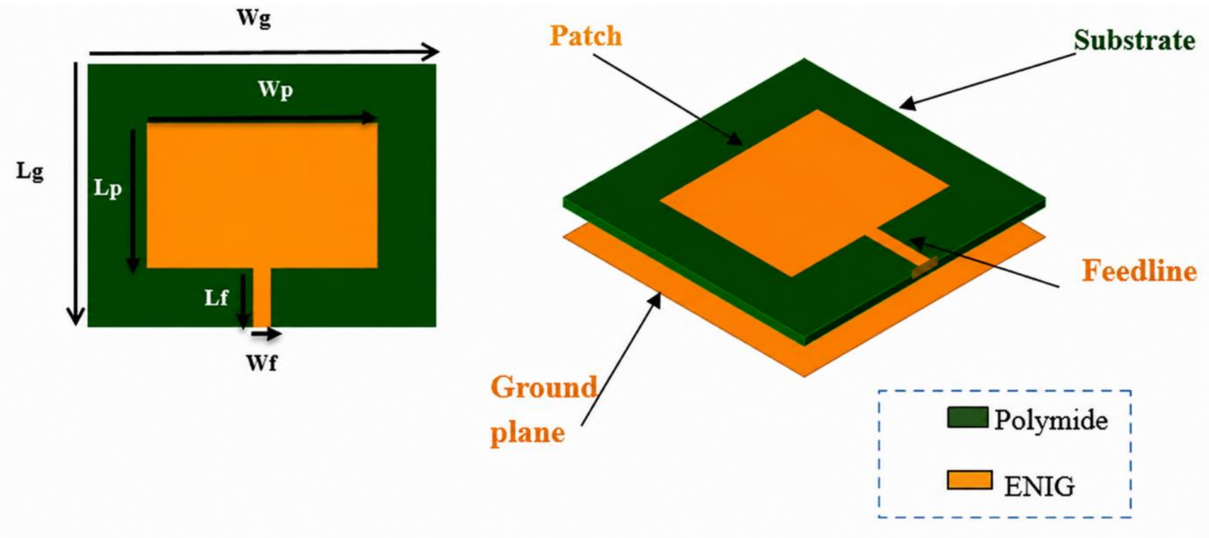

Figure IV.2: Geometry of simple patch antenna structure.

The antenna structure occupies an overall area of $800 \times 800\, \mu m^2$, whereas the radiating patch size is limited to $525 \times 440\, \mu m^2$. A 50 Ω microstrip feed line with dimensions of $40 \times 200\, \mu m^2$ is employed to ensure proper impedance matching. The compact geometry are detailed in **Table IV.1** makes the proposed antenna appropriate for highly integrated terahertz applications.

Parameters	Values (μm)	Parameters	Values (μm)
$\mathbf{W}_g$	800	**t**	0.5
$\mathbf{L}_g$	800	$\mathbf{W_f}$	40
H	25	$\mathbf{L_f}$	200
$\mathbf{W_P}$	525	$\mathbf{L_P}$	440

Table IV.1: Optimized Geometric Parameters of the Proposed Antenna.

The single-element antenna underwent a systematic five-stage geometric evolution aimed at enhancing impedance matching, gain, and overall bandwidth performance in the terahertz frequency range. **Figure IV.3** illustrates the front and back views of each stage in the evolutionary progression.

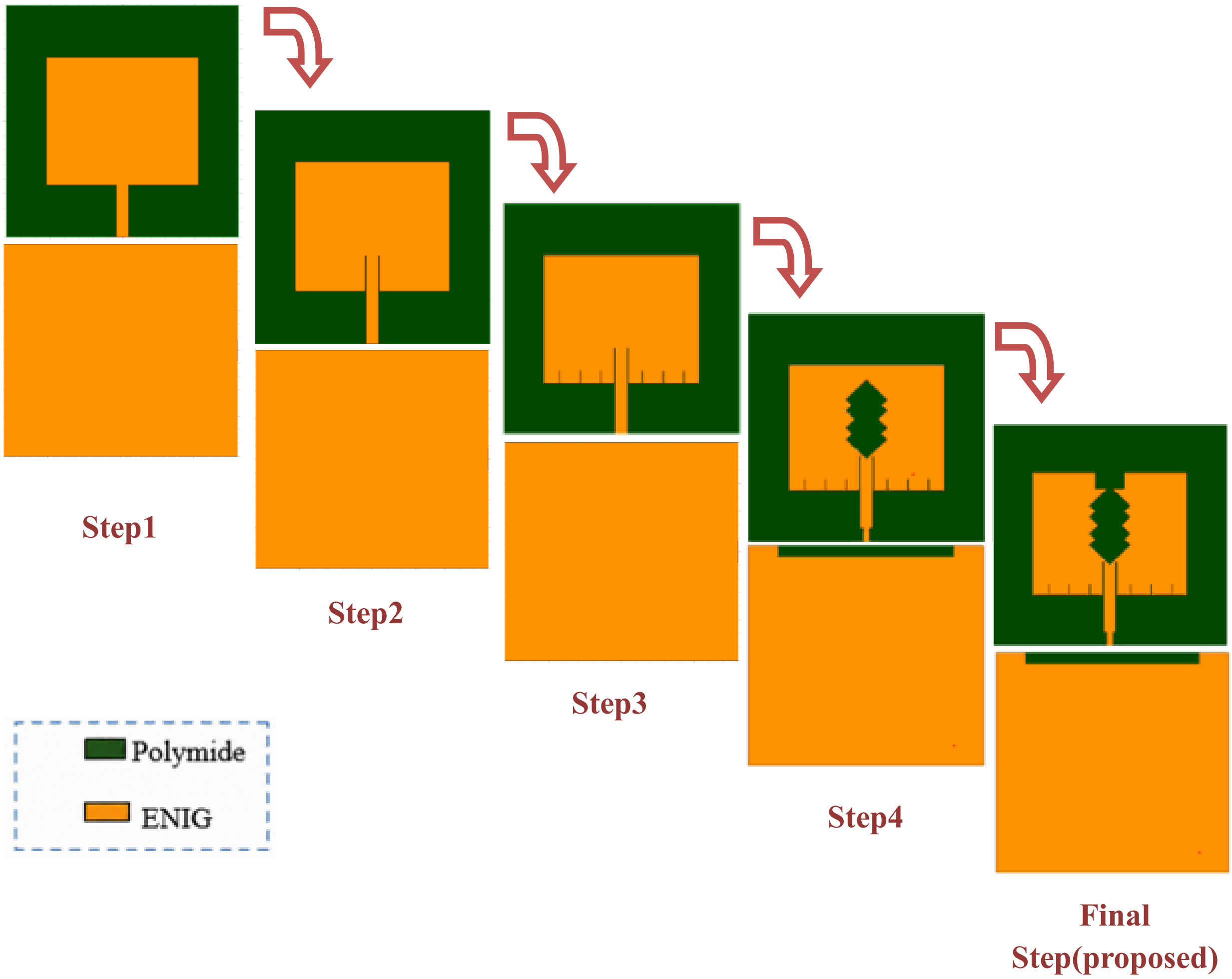

Figure IV.3: Steps for the design of proposed antennas.

Step 1: First Design of rectangular patch antenna

In the first step, conventional rectangular patch antenna is designed and analyzed using HFSS. As shown in the simulated results **(Figure IV.4),** the design demonstrates effective performance across the 0.1 to 0.95 THz range, particularly at the 0.289 THz resonance where the return loss reaches -14.03 dB. At this target band, the system achieves a bandwidth of 0.003 THz.

The antenna also exhibits remarkable multiband behavior with several significant resonances: a return loss of -15.24 dB at 0.514 THz and -18.10 dB at 0.615 THz, -24.20 dB at 0.786 THz with bandwidth of 0.013 THz and-16.09 dB at 0.858 THz with bandwidth of 0.067 THz.

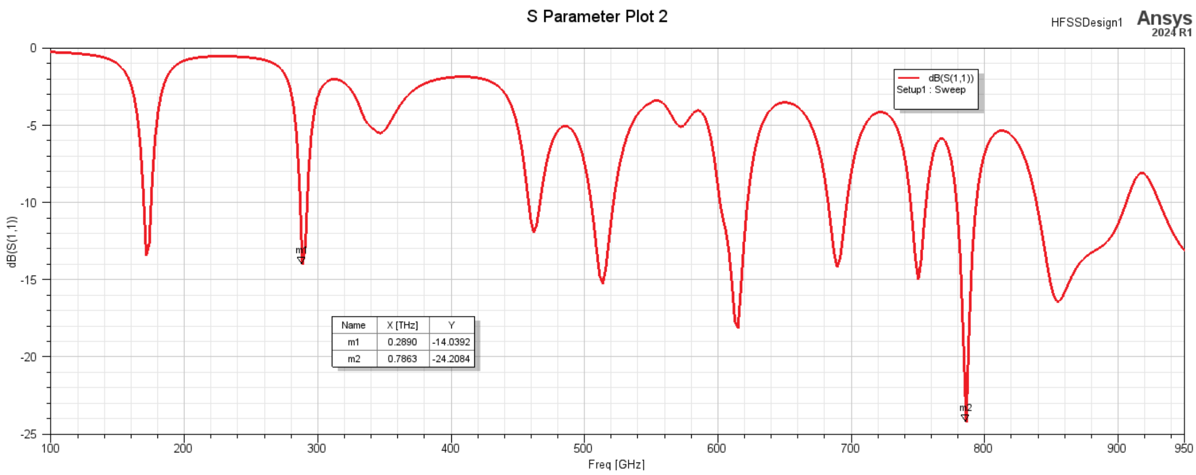

Figure IV.4: Reflection Coefficient (S_{11}) of the First step.

After identifying the resonance points, we analyzed the gain and radiation patterns for our two primary frequencies of interest: the 0.289 THz target and the 0.786 THz peak, which represents the deepest resonance.

Antenna design at 0.289 THz exhibits a gain of 2.65 dB and a bidirectional pattern, as shown in **Figure IV.5(a)**. At the higher frequency of 0.786 THz in **Figure IV.5(b)**, the gain remains stable at 2.65 dB, though the pattern becomes more directive with noticeable side lobes.

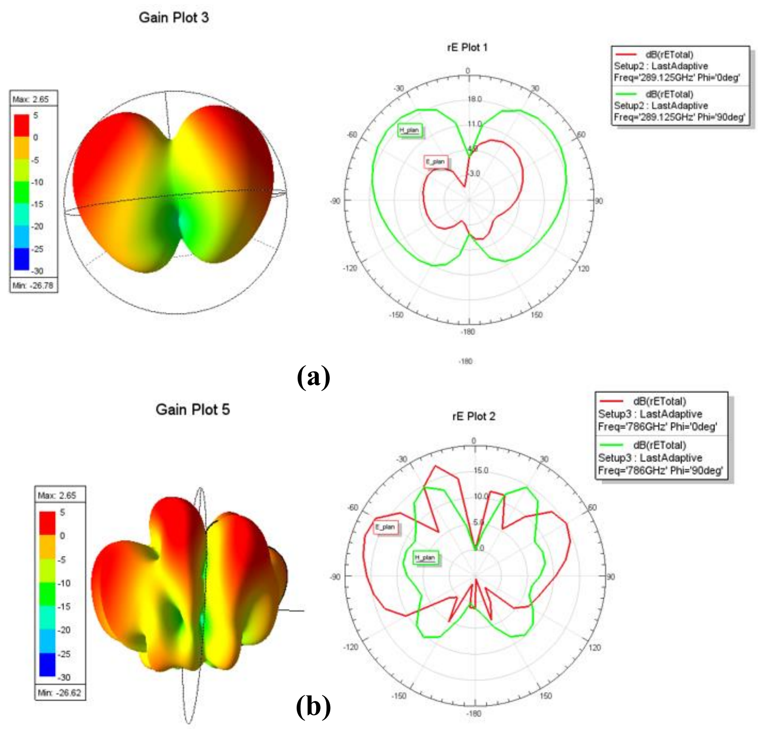

Figure IV.5: Radiation performance of the first configuration showing 3D gain and 2D patterns at: (a) 0.289 THz and (b) 0.786 THz.

The variation of gain across the 0.1 to 0.95 THz range was analyzed using MATLAB to verify the antenna's performance stability as shown in **Table IV.2.** The results show the gain increasing from -6.68 dB at 0.1 THz to a peak of 8.55 dB at 0.514 THz, maintaining stable performance between 2.65 dB and around 6 dB through the higher frequencies (see **Figure IV.6)**.

Frequency (THz)	Gain (dB)	Frequency (THz)	Gain (dB)
0.1	-6.68	0.690	6.51
0.172	2.08	0 .750	5.71
0.289	2.65	0.786	2.65
0.514	8.55	0.866	6.62
0.614	4.98	0.95	6.15

Table IV.2: Variation of Gain with Operating Frequency for first step.

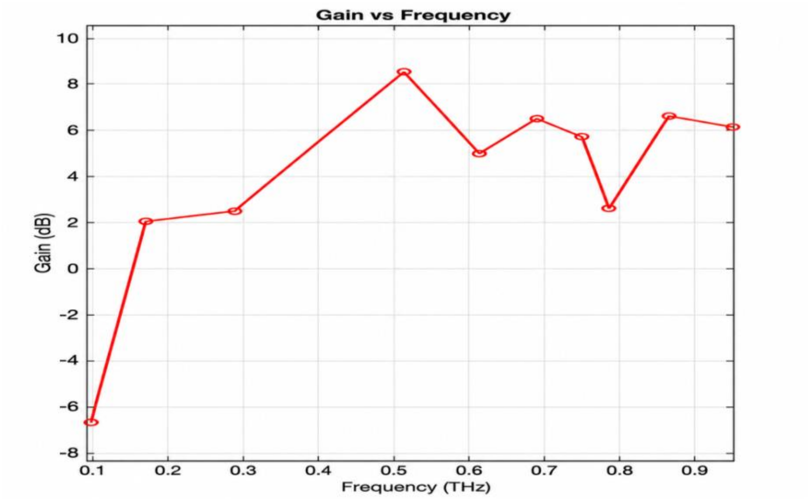

Figure IV.6: Simulated Gain vs. Frequency plot for first step.

Step 2: Antenna with slots introduced in the feed line

We modified our antenna design in step 2 by adding two narrow gaps in the feed line (L_1 =120 μm, W_1= 5μm each) in the patch. The overall design size is 120 ×5×0.5 μm^3.

Parameters	Values (µm)
W_1	5
L_1	120

Table IV.3: Geometrical Parameters of step 2.

As shown in **Figure IV.7,** the antenna achieves excellent impedance matching at the primary target 0.2935 THz, which exhibits a significant return loss of -27.27 dB and a bandwidth of 0.009 THz.

In addition to this target, multiple additional resonances are observed across the 0.1 to 0.95 THz range: at 0.172 THz (-19.88 dB), at 0.5 THz (-25.32 dB), and a maximum resonance at 0.786 THz (-36.41 dB) with bandwidth of 0.013 THz.

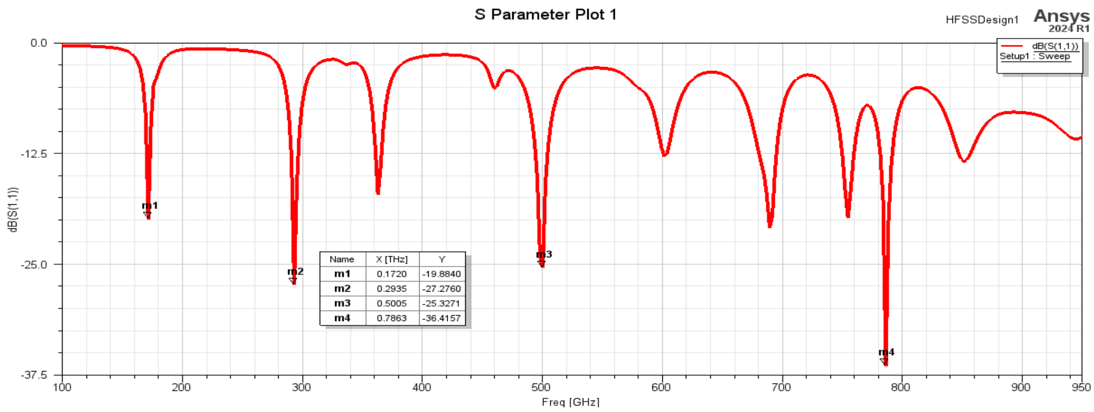

Figure IV.7: Reflection coefficient (S_{11}) of step 2.

The peak gain and its variation with frequency for the final configuration are illustrated in **Figure IV.8**. At the primary target of 0.293 THz, the antenna achieves a peak gain of 2.86 dB with a broad, bidirectional radiation pattern. At 0.786 THz, the gain remains stable at 2.98 dB, though the pattern becomes more directive with complex lobe formations.

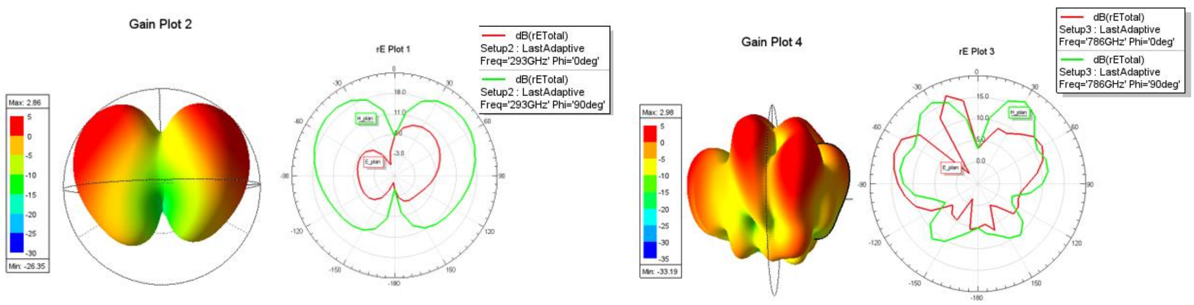

(a) (b)

Figure IV.8: Radiation performance of the second configuration showing 3D gain and 2D patterns at: (a) 0.293 THz and (b) 0.786 THz.

For gain vs frequency, as shown in **Table IV.4** and **Figure IV.9**. The results indicate that the gain increases from -9.10 dB at 0.1 THz to a maximum peak of 9.10 dB at 0. 689 THz.The antenna demonstrates predominantly high gain performance across the considered frequency range.

Frequency (THz)	Gain (dB)	Frequency (THz)	Gain (dB)
0.1	-9.10	0.689	9.10
0 .174	2.26	0.754	4.80
0.293	2.86	0.786	2.90
0.500	8.56	0.943	4.05
0.604	2.83	0.95	3.19

Table IV.4: Variation of peak Gain with operating frequency for second step.

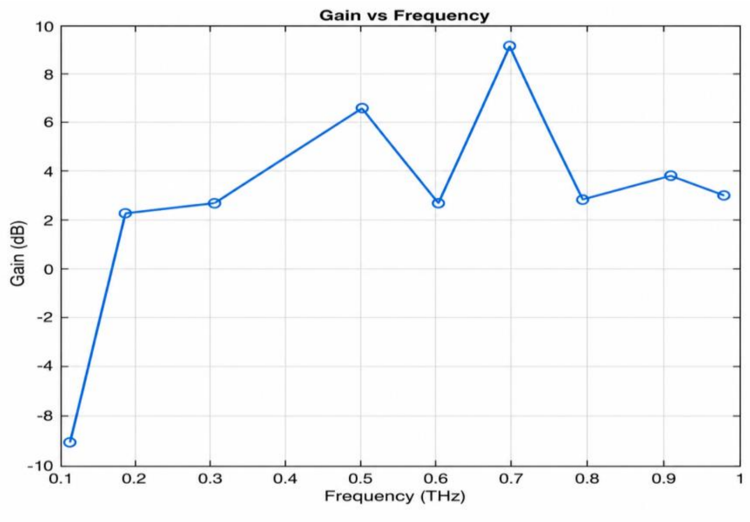

Figure IV.9: Simulated Gain vs. Frequency plot for second step.

The following table summarizes the performance optimization achieved between the conventional rectangular patch antenna (Step 1) and the modified design with feed line slots (Step 2).

Parameter	Step 1 (Conventional)	Step 2 (With Slots)
Target Frequency	0.289 THz	0.293 THz
Return Loss (S11)	-14.37 dB	-27.27 dB
Bandwidth	0.003THz	0.009 THz
Gain (Target)	2.65 dB	2.86 dB

Table IV.5: The performance optimization achieved between step 1 and step 2.

Step 3: Performance Analysis of the Modified Patch Antenna with Six Additional Gaps

In Step 3, the antenna geometry was further optimized by incorporating six additional narrow slots distributed across the patch, each measuring 40 µm in length and 3 µm in widths.

Parameters	Values (μm)
W_2	40
L_2	3

Table IV.6: Geometrical parameters of step 3.

As shown in **Figure IV.10,** at the primary target frequency of 0.293 THz, the antenna achieves a deep return loss of -29.03 dB with a bandwidth of 0.009 THz.

Following this target, the design exhibits significant performance at other resonant frequencies at 0.174 THz reaches -19.22 dB, while at 0.5 THz shows a return loss of -29.94 dB with a bandwidth of 0.014 THz. Further resonances are observed at 0.685 THz with -21.80 dB, 0.775 THz reaching -26.64 dB with a wider bandwidth of 0.036 THz, and finally large band 0.110THz at -10 dB from 0.840 to 0.950 THz.

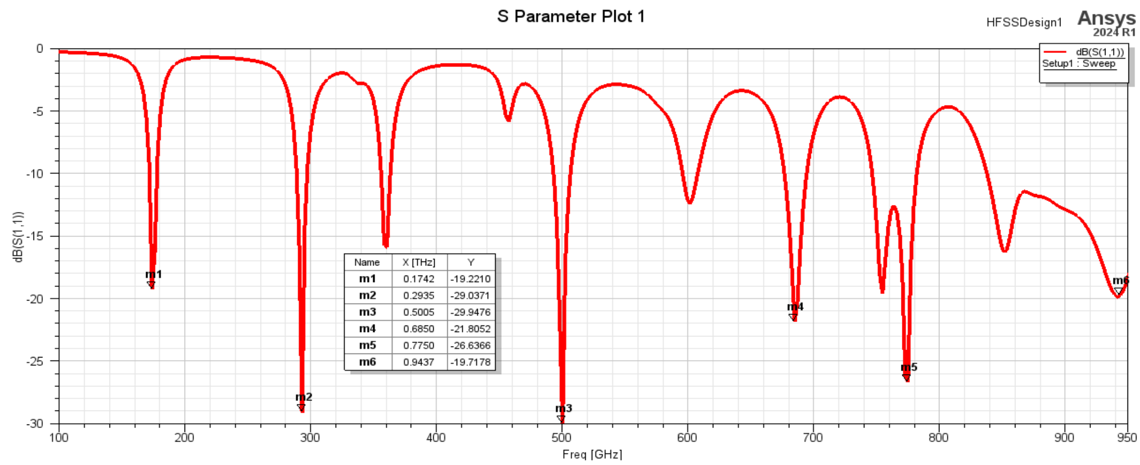

Figure IV.10: Reflection coefficient (S_{11}) of step 3.

The gain and the radiation patterns in the E- and H-planes for the frequencies 0.293 THz and 0.5 THz are presented in the **Figure IV.11**.

At the primary target of 0.293 THz, the antenna achieves a gain of 2.78 dB. The 3D and 2D polar plots reveal a broad, bidirectional radiation pattern. As the frequency increases to 0.5 THz, the gain rises significantly to 8.52 dB. At this higher resonance, the radiation pattern becomes more directive.

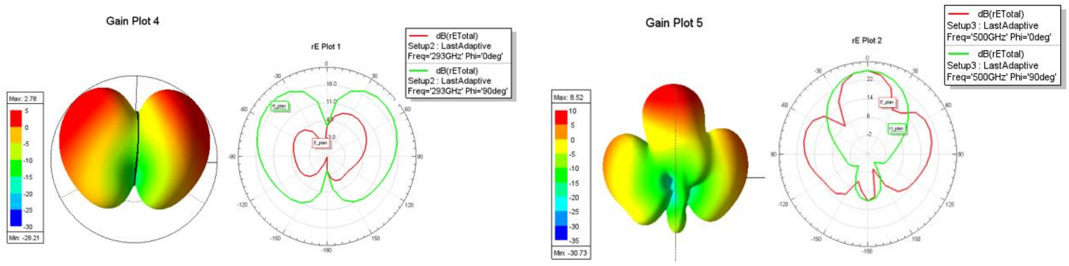

Figure IV.11: Radiation performance of the third configuration showing 3D gain and 2D patterns at: (a) 0.293 THz and (b) 0.5 THz.

The frequency-dependent gain analysis, plotted in **Figure IV.12** and detailed in **Table IV.7**, reveals a highly dynamic and efficient radiation performance across the 0.1 to 0.95 THz range. Starting from -9.48 dB at 0.1 THz, the gain climbs steadily to reach a stable 2.78 dB at the 0.293 THz primary target. The antenna showcases its superior multiband capability with powerful peaks at 0.500 THz (8.52 dB) and a maximum global resonance of 8.71 dB at 0.685 THz.

Frequency (THz)	Gain (dB)	Frequency (THz)	Gain (dB)
0.1	-9.48	0.601	2.59
0.174	2.39	0.685	8.71
0.293	2.78	0.775	3.11
0.361	0.76	0.943	5.17
0.500	8.52	0.95	5.47

Table IV.7: Variation of Gain with operating frequency for third step.

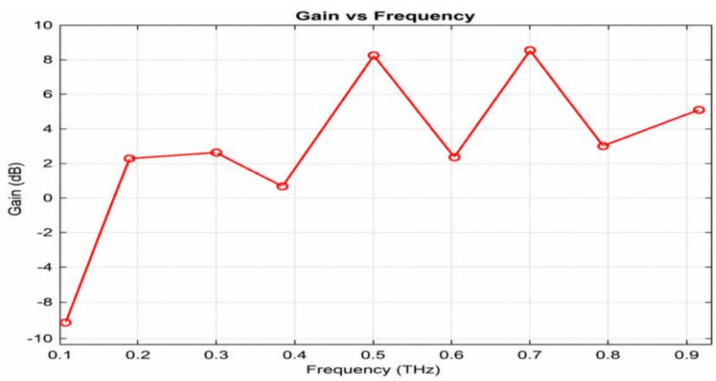

Figure IV.12: Simulated Gain vs. Frequency plot for third step.

The **Table IV.8** below presents the comparative results between the slotted feed line design (Step 2) and the optimized patch configuration with reduced width and six additional gaps (Step 3).

Parameter	Step 2	Step 3
Return Loss (S_{11}) Target	-27.27 dB	-29.03 dB
Gain (Target)	2.86 dB	2.78 dB

Table IV.8: The performance optimization achieved between step 2 and step 3.

Step 4: Design Modification using Stepped Slot and Ground Slot (DGS)

In this design, we added a stepped slot and a ground slot (W_3 and L_3) to the compact microstrip patch to improve and provide better control over the resonant frequency.

Parameters	Values (μm)
W_3	40
L_3	300

Table IV.9: Geometrical parameters of fourth Step.

We note that at the target frequency 0.311 THz, the antenna exhibits a reflection coefficient of −23.63 dB with an impedance bandwidth of approximately 0.011 THz under the −10 dB criterion (see **Figure IV.13**). At 0.8785 THz, a deeper resonance of −39.84 dB is achieved, providing excellent matching, with bandwidth of about 0.030 THz.

We also observe good reflections around the frequency: 0.167 THz with a return loss of -17.47 dB.

Figure IV.13: Reflection coefficientS_{11} of step 4.

The radiation performance illustrated in **Figure IV.14** shows clear improvements in power handling. At the 0.311 THz target, the antenna provides a gain of 3.87 dB with a broad, bidirectional pattern, ensuring stable coverage. At the higher 0.878 THz resonance, the gain increases significantly to 8.20 dB as the pattern becomes more directive with defined lobes.

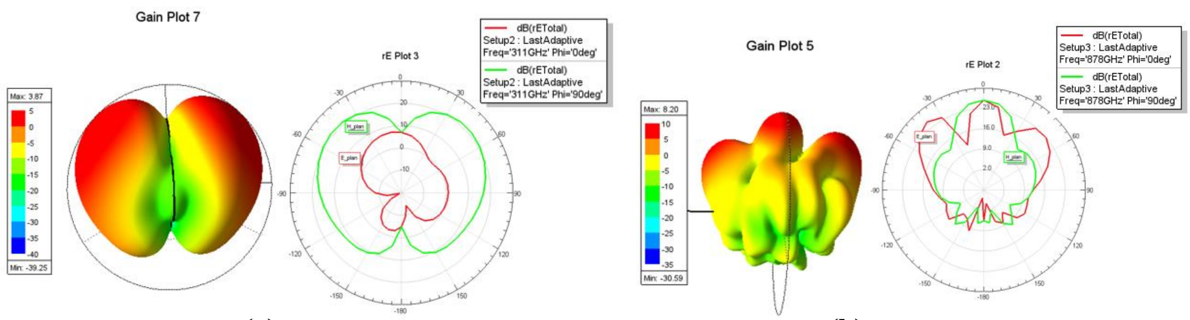

(a) **(b)**

Figure IV.14: Radiation performance of the fourth configuration showing 3D gain and 2D patterns at: (a) 0.311 THz and (b) 0.878THz.

The following **Figure IV.15** shows the total gain as a function of frequency and detailed in **Table IV.10** efficient radiation profile across the 0.1 to 0.95 THz range.

Starting from -9.71 dB at 0.1 THz, the gain increases steadily to reach a stable 3.87 dB at the primary 0.311 THz target. The antenna demonstrates its superior multiband capability with a high peak of 7.61 dB at 0.487 THz and reaches its maximum global gain of 8.20 dB at the 0.878 THz resonance.

Frequency (THz)	Gain (dB)	Frequency (THz)	Gain (dB)
0.1	-9.71	0.606	3.12
0.167	1.72	0.757	3.44
0.311	3.87	0.878	8.20
0.462	4.20	0.950	7.75
0.487	7.61		

Table IV.10: Variation of Gain with operating frequency for fourth step.

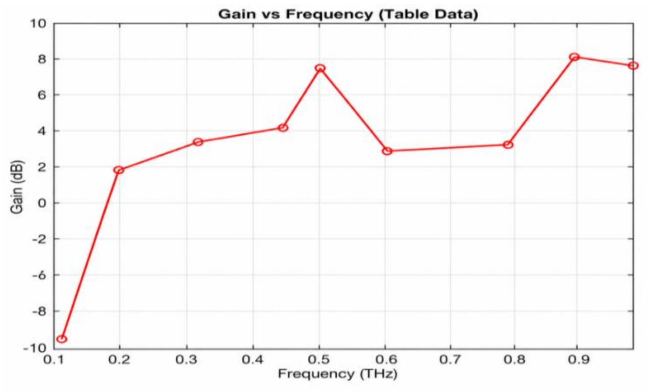

Figure IV.15: Simulated Gain vs. Frequency plot for fourth step.

A comparative analysis between step 3 and step 4 presents in **Table IV.9.**

Parameter	**Step 3 (6-Gap Patch)**	**Step 4 (Stepped Slot + DGS)**
Primary Target Frequency	0.293 THz	0.311 THz
Return Loss (S_{11}) Target	-29.03 dB	-23.63 dB
Bandwidth Target	0.009 THz	0.011 THz
Gain Target	2.78 dB	3.81 dB

Table IV.11: The performance optimization achieved between step 3 and step 4.

Final Step: Central Rectangular Insertion

A rectangular shape $60 \times 100\ \mu m^2$is placed right in the middle, on top of the stepped slot, as our final tweak to the design (see **Figure IV.16)**.

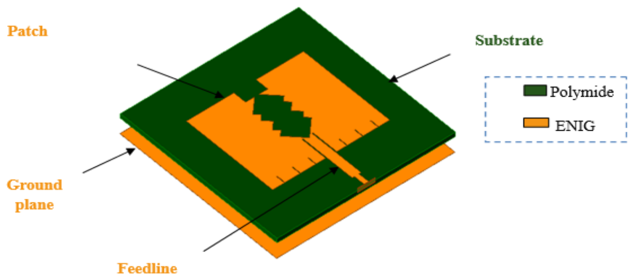

Figure IV.16: The design of proposed antennas

Parameters	**Values (μm)**
W_4	60
L_4	100

Table IV.12: Geometrical parameters of final Step.

Figure IV.17 shows that the reflection coefficient S_{11} for the final optimized configuration demonstrates exceptional multiband performances.

At the primary target frequency of 0.313 THz, the antenna achieves a solid return loss of -22.69 dB and an improved bandwidth of 0.019 THz

The design further showcases its versatility with a series of distinct resonances starting at 0.169 THz (-18.34 dB) and continuing through the mid-range with significant peaks at 0.462 THz (-24.14 dB), 0.491 THz (-22.01 dB), and 0.622 THz (-21.32 dB). Toward the higher end of the spectrum, the antenna maintains matching at 0.878 THz (-15.46 dB) before reaching an extraordinary global maximum at 0.948 THz. This final peak exhibits a remarkable return loss of -51.89 dB.

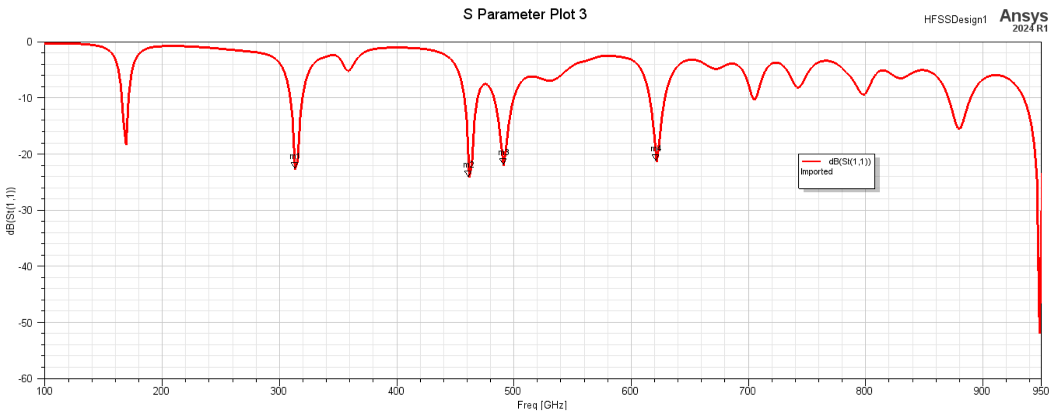

Figure IV.17: Reflection coefficient (S_{11}) of final step.

The radiation performance of the final optimized configuration presented in **Figure IV.18.**

At the primary target frequency of 0.313 THz, the antenna achieves a gain of 4.10 dB. The 3D radiation plot and 2D polar patterns reveal a broad, bidirectional characteristic.

As the frequency increases to the deepest resonant point at 0.948 THz, the peak gain rises to 6.50 dB, and the radiation pattern becomes more directive with more defined lobes**.**

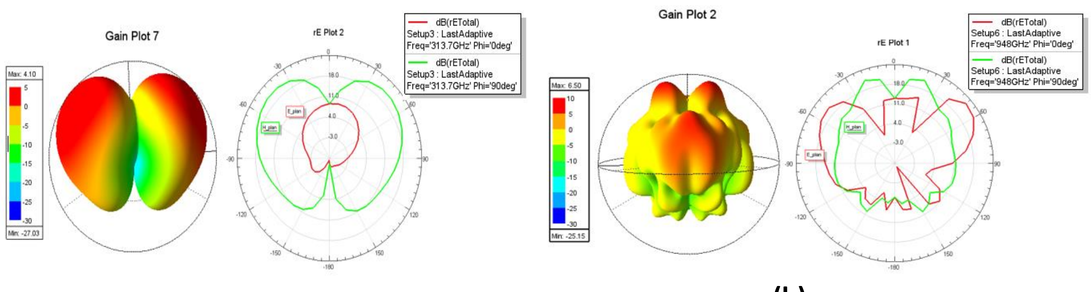

Figure IV.18: Radiation performance of the final configuration showing 3D gain and 2D patterns at: (a) 0.313 THz and (b) 0.948 THz.

The gain performance of the final design, as detailed in **Figure IV.19**, demonstrates high radiation efficiency across the spectrum. Starting from -9.89 dB at 0.1 THz, the gain reaches a stable 4.10 dB at the 0.313 THz target. The antenna achieves a significant peak of 6.59 dB at 0.491 THz and a global maximum of 9.17 dB at 0.878 THz. Even at 0.95 THz, the gain remains strong at 6.15 dB.

Frequency (THz)	Gain (dB)	Frequency (THz)	Gain (dB)
0.1	-9.89	0.622	3.20
0.169	1.73	0.878	9.17
0.313	4.10	0.948	6.50
0.462	4.87	0.95	6.15
0.491	6.59		

Table IV.13: Variation of gain with operating frequency for final step.

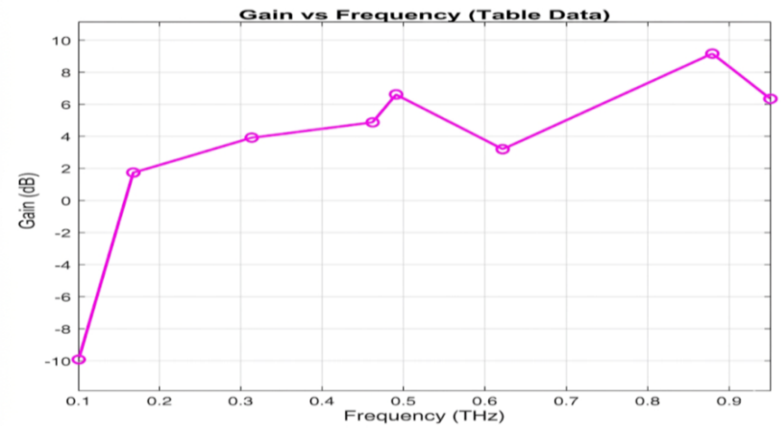

Figure IV.19: Simulated Gain vs. Frequency plot for final step.

To provide a clear overview of the design evolution, the following table summarizes the performance metrics of the previous configuration against our final optimized design, highlighting the significant enhancements achieved through our structural refinements.

Parameter	**Step 4 (Stepped Slot + DGS)**	**Final Step (Central Insertion)**
Target Frequency	0.311 THz	0.313 THz
Return LossTarget	-23.63 dB	-22.69 dB
Bandwidth Target	0.011 THz	0.019 THz
Gain Target	3.87 dB	4.10 dB

Table IV.14: The performance optimization achieved between step 4 and step 5.

We traced the peak gain across the entire 0.1 to 0.95 THz band, and at our specific target frequency of 0.313 THz (see **Figure IV.20)**, we obtained a stable gain value of approximately 4.6 dB. Even though the curve reaches an absolute maximum of 8.76 dB at 0.5 THz, the gain drops significantly after this 0.5 THz peak, falling down to about 4.8 dB at 0.9 THz.

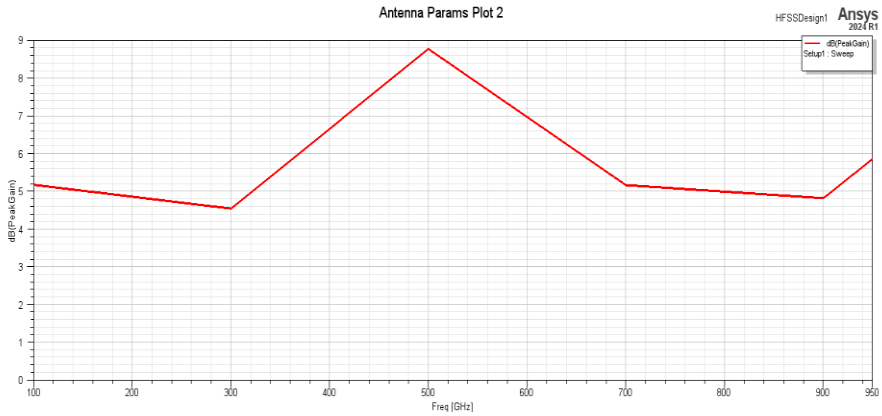

Figure IV.20: Peak gain versus frequency characteristics of the proposed antenna.

To illustrate the design evolution, a comparative analysis of the reflection coefficient S_{11} and gain for all five steps is presented in **Figure IV.21(a)** and **Figure IV.21(b)**. These consolidated plots demonstrate the progressive optimization of the antenna, showing how the resonances shifted and deepened through each iteration. The results clearly highlight the superiority of the final step, which successfully achieves the 0.313 THz target with enhanced bandwidth, higher gain.

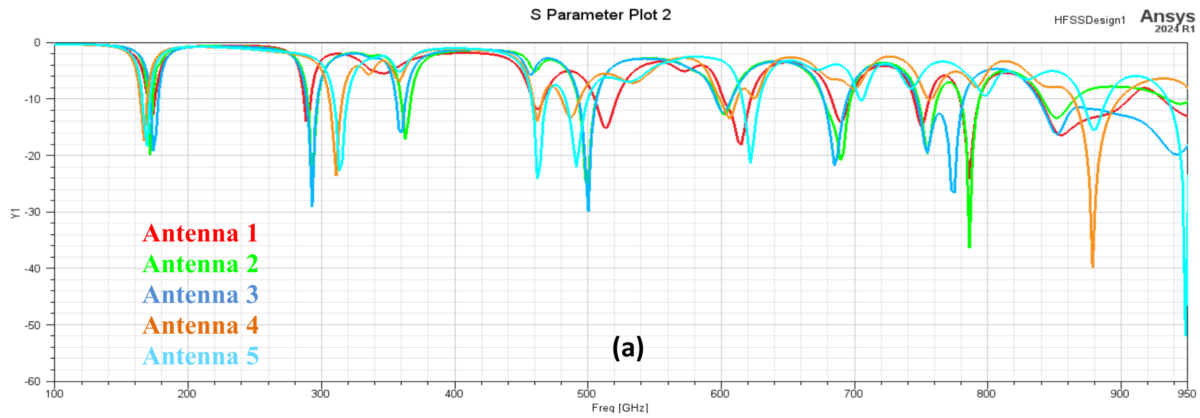

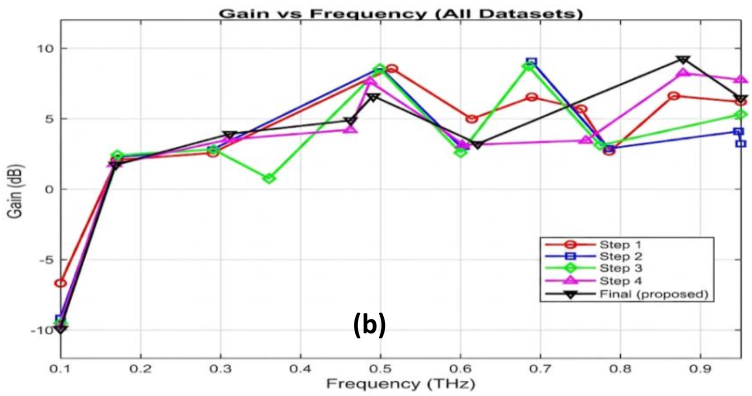

Figure IV.21: Comparative Analysis of (a) Reflection Coefficient (S_{11}) and (b) Gain Versus Frequency for All Design Iterations.

IV.4. MIMO Antenna Analysis

To develop the2x2 MIMO system, three distinct geometric configurations were evaluated to optimize spatial decoupling and minimize mutual coupling between elements. Using the single-element antenna as a foundation, this 2-port MIMO design enhances signal reception through spatial diversity, interference mitigation, and capacity enhancement.

The methodology involved a parametric sweep of the inter-element distance (d) for each configuration, ranging from 550 to 900 μm with a step size of 50 μm. By tracing S_{11} and S_{12}parameters across these increments, we were able to identify the specific distance offering the optimal balance between resonance and isolation. **Figure IV.22** illustrates these configurations, which were compared based on return loss and port isolation.

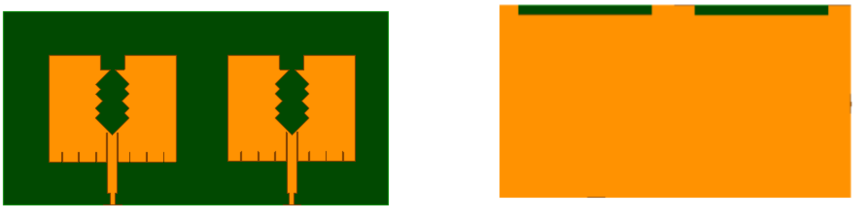

(a) MIMO Antenna 1

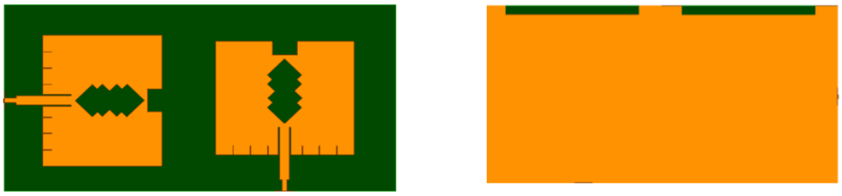

(b) MIMO Antenna 2

(c) MIMO Antenna 3

Figure IV.22: Comparative analysis of 2x2 MIMO antenna Configurations, (a) MIMO antenna 1, (b) MIMO antenna 2, (c) MIMO antenna 3.

The first configuration (2x2 MIMO Antenna 1) positions the two elements at a 0-degree orientation, aligned side by side shown in **Figure IV.22(a).** To conclude our parametric study for the first configuration, we compared all inter-element distances on a single plot for both S_{11} and S_{12} as shown in **Figure IV.24**.

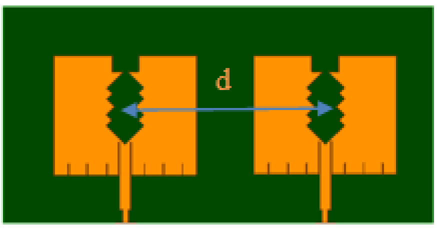

Figure IV.23: First configuration of 2×2 MIMO antenna **1** at d=750 μm.

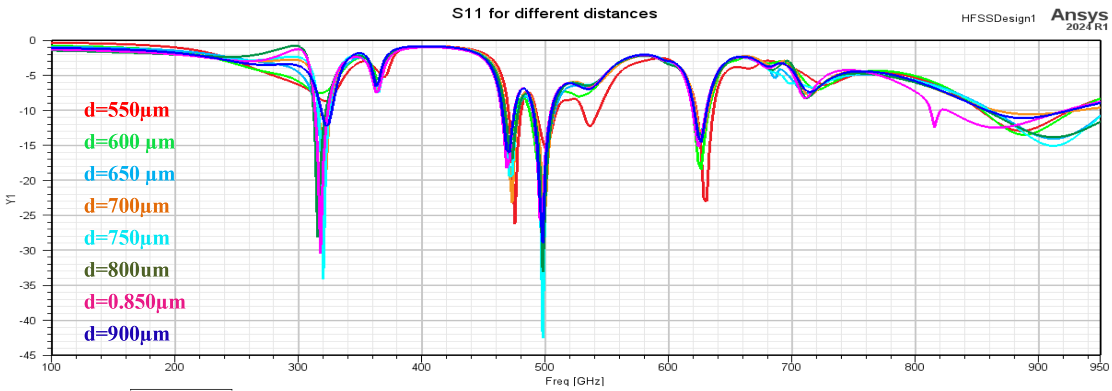

(a) Return loss S_{11}

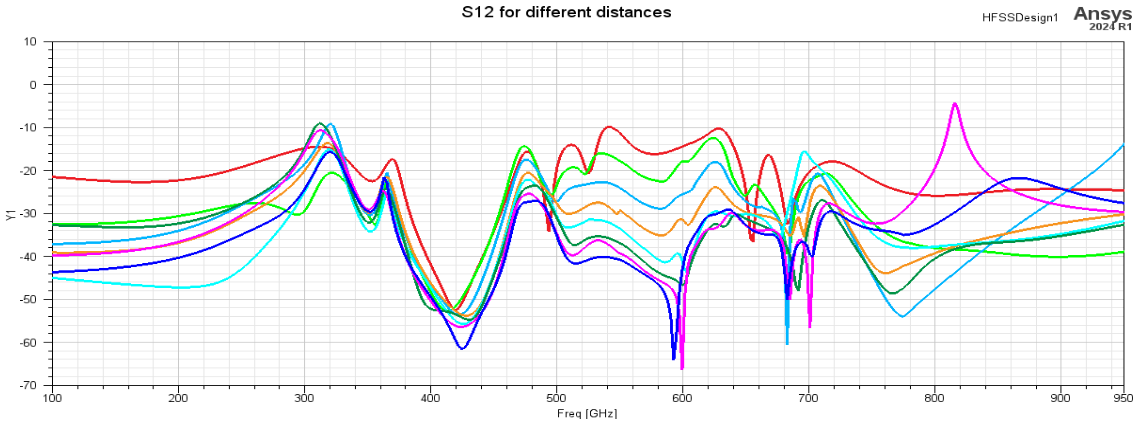

(b) Isolation S_{12}

Figure IV.24: Comparative analysis of S-parameters for different inter-element distances (d = 550 to 900 μm) for the first configuration: (a) Return loss $S_{11}$and (b) Isolation S_{12}.

Through this comparison, we found that for d = 750 μm, the antenna achieves exceptional impedance matching as shown in **Figure IV.24**.

Particularly at the target frequency of 0.322 THz, where the return loss drops to −34.11 dB. The system also exhibits remarkable multiband performance with a very deep resonance of -42.45 dB at 0.498 THz, alongside other significant peaks -19.43 dB at 0.473 THz, -13.72 dB at 0.626 THz, and-15.05 dB at 0.912 THz.Port isolation lower by -15 dB around these frequency peaks (see **Figure IV.25).**

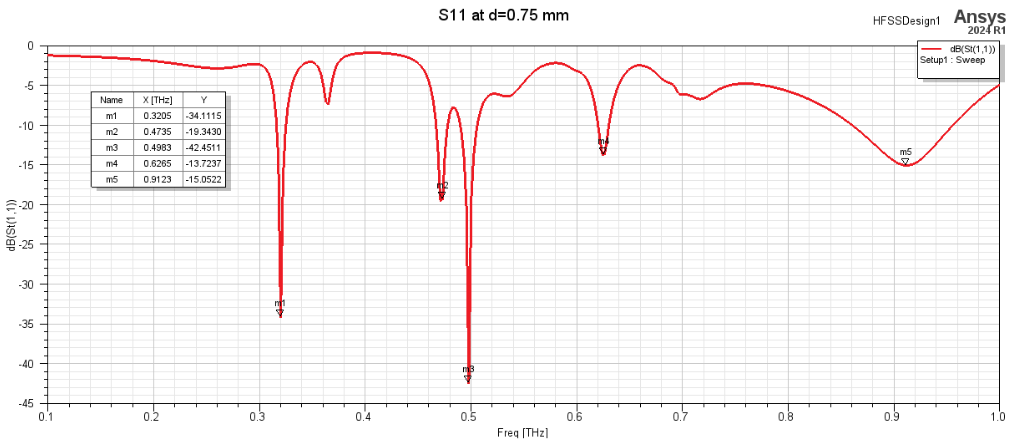

a) Reflection coefficient S_{11}

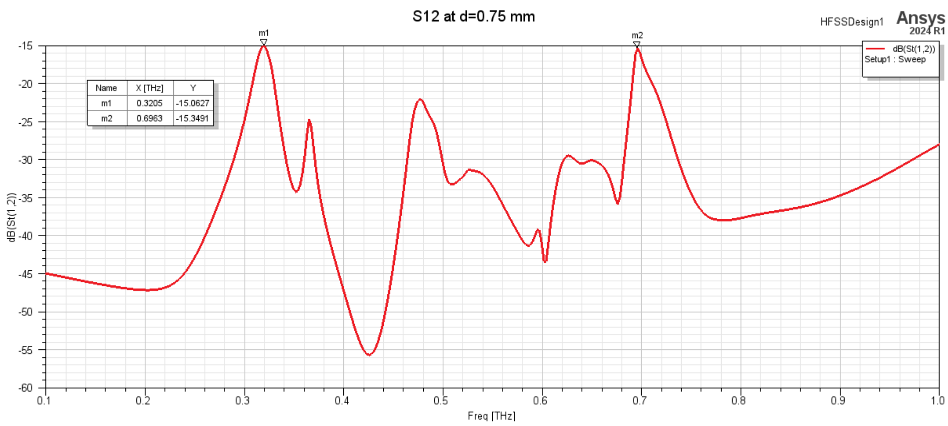

b) Isolation S_{12}

Figure IV.25: S_{11} and S_{12}parameter performance of the first configuration MIMO Antenna at d = 750 μm.

We evaluated the antenna's performance by analyzing the gain and radiation patterns at two critical points, our target frequency of 0.32 THz and the frequency of deepest resonance at 0.498 THz (see **Figure IV.26)**. This allowed us to verify that the optimized impedance matching at d = 750 μm also translates to stable radiation characteristics and high directional gain across its primary operating bands.

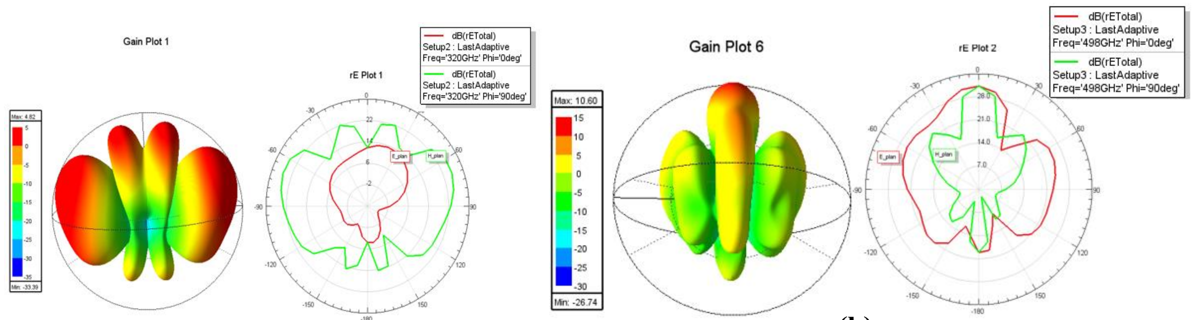

(a) **(b)**

Figure IV.26: Radiation performance of the first configuration at d = 750 μm showing 3D gain and 2D patterns at: (a) 0.32 THz and (b) 0.498 THz.

At the target frequency of 0.32 THz, the system achieves a peak gain of 4.82 dB, showing stable and almost symmetrical radiation patterns. When analyzing the deep resonance at 0.498 THz, the performance increases significantly with a maximum gain of 10.60 dB. The patterns at this frequency remain highly directive with well-defined main lobes.

Since the two ports in this configuration are placed very close to each other, strong mutual coupling affects the isolation performance. Therefore, A Defected Ground Structure (DGS) was introduced by etching a slot in the ground plane to improve the isolation between the ports (see **Figure IV.27**).

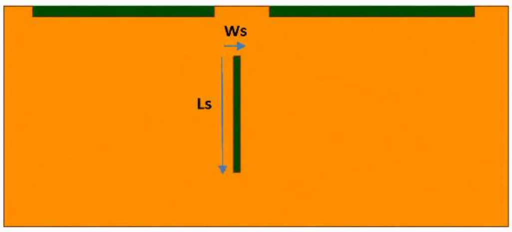

Figure IV.27: Center ground slot for isolation.

After extensive optimization of the slot dimensions L_s and W_s, excellent results were achieved for L_s=450 μm and W_s=21 μm, as shown in **Figure IV.28**. At our target frequency, we found a deep return loss of -30 dB at 0.322 THz with bandwidth of 0.011 THz and a good isolation of -21.27 dB.The configuration also displays impressive multiband performance, with additional resonances -27.75 dB at 0.471 THz, -22.04 dB at 0.498 THz, -15.04 dB at 0.626 THz, and -11.57 at 0.871 dB THz.

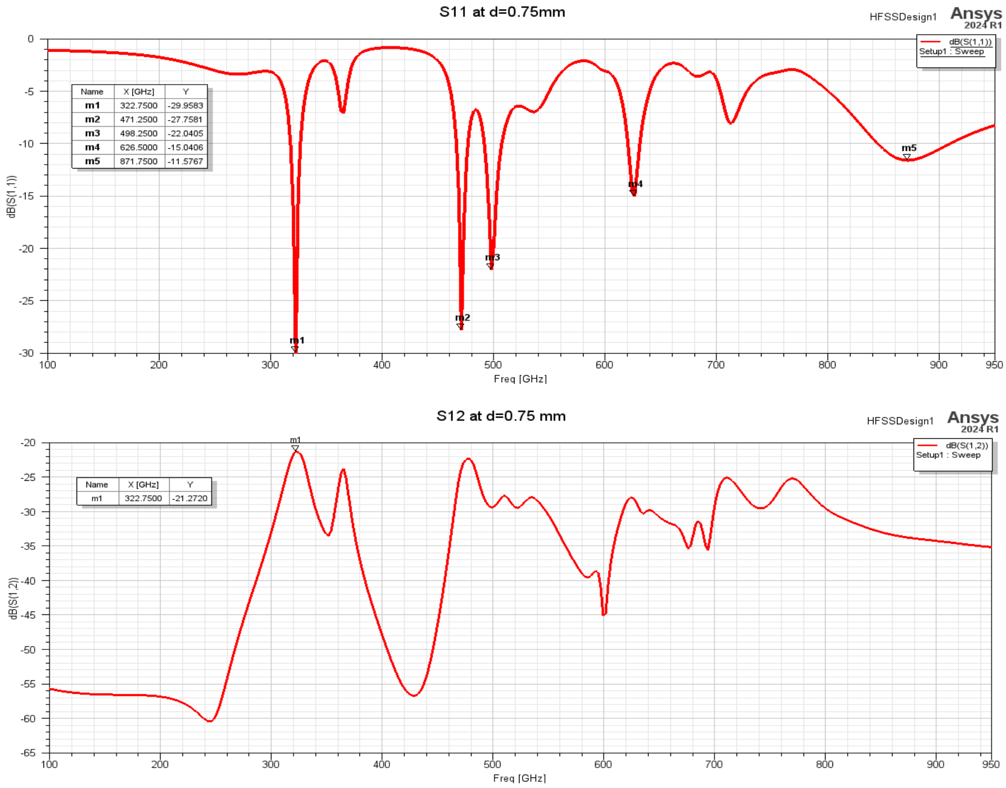

Figure IV.28: S_{11} and S_{12} Parameter Performance of the first configuration MIMO Antenna 1 with slot at d = 750 μm.

The gain and radiation pattern performances were analyzed at the target frequency of 0.322 THz and at the frequency corresponding to the deepest resonance, 0.471 THz (see **Figure IV.29**).

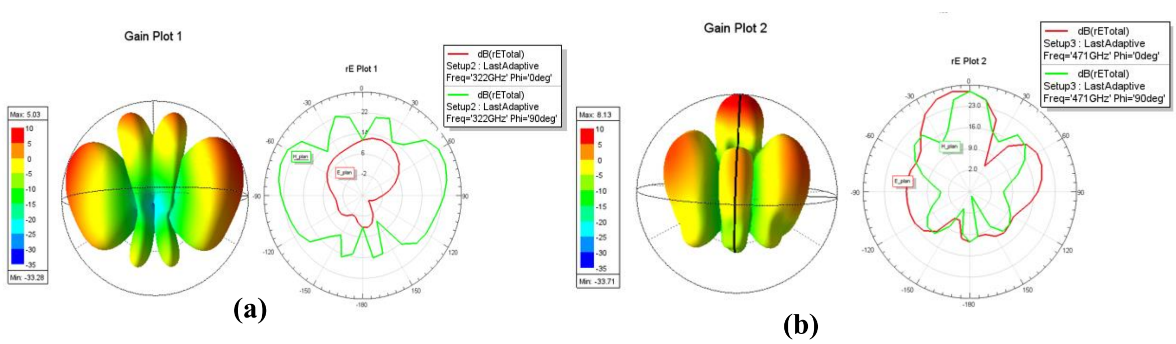

Figure IV.29: Radiation performance of the first configuration showing 3D gain and 2D patterns at: (a) 0.322 THz and (b) 0.471 THz.

At our target frequency of 0.322 THz, the system achieves a maximum gain of 5.03 dB. At the higher resonance of 0.471 THz, the performance significantly improves with a gain of 8.13 dB, showing a more directive beam with well-defined lobes. These results confirm that our chosen configuration maintains high radiation efficiency and robust directional characteristics across its operating brands. To wrap up our analysis, we also plotted Gain against Frequency to see how the antenna performs across our target band. We took the discrete data points from our simulation (as shown in the **Table IV.15**) and imported them into MATLAB to generate a continuous gain profile. This allows us to visualize the antenna's performance trend across the 0.1 THz to 0.95 THz range.

Frequency (THz)	Gain(dB)	Frequency (THz)	Gain(dB)
0.1	-6.55	0.55	9.91
0.20	1.80	0.626	6.81
0.322	5.03	0.714	612
0.365	3.95	0.802	7.93
0.471	8.13	0.874	12.34
0.498	10.27	0.950	7.23

Table IV.15: Variation of gain with operating frequency at d= 750 μm.

These results validate our design, which provides a stable and sufficient gain of 5.03 dB at the target frequency of 0.322 THz, while also offering additional high-gain performance at higher frequencies (see **Figure IV.30**).

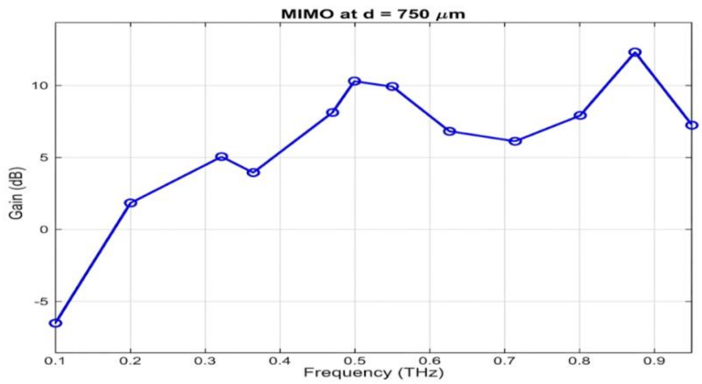

Figure IV.30: Simulated Gain vs. Frequency for the first configuration 2x2 MIMO Antenna 1 at d = 750 μm.

In the second configuration (2x2 MIMO Antenna 2), depicted **Figure IV.22(b)**, the two elements are oriented at 90 degrees. We followed the same optimization methodology used for the first design. We consolidated the results into two comprehensive comparison plots to evaluate the impact of spacing on performance (**Figure IV.32)**.

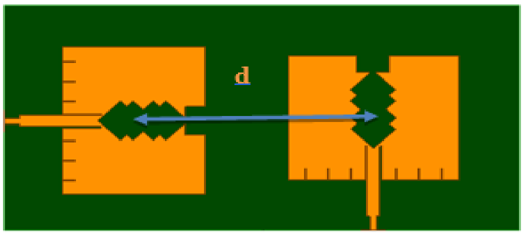

Figure IV.31: Second configuration of 2×2 MIMO antenna 2.

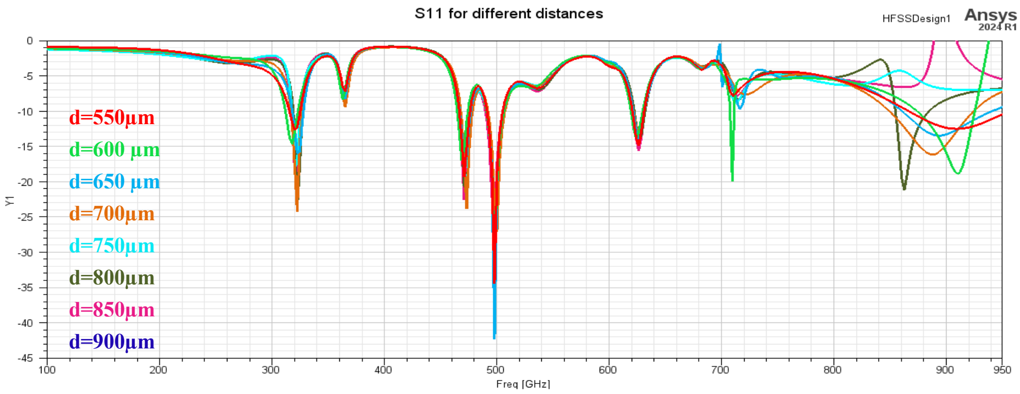

(a) Return loss S_{11}

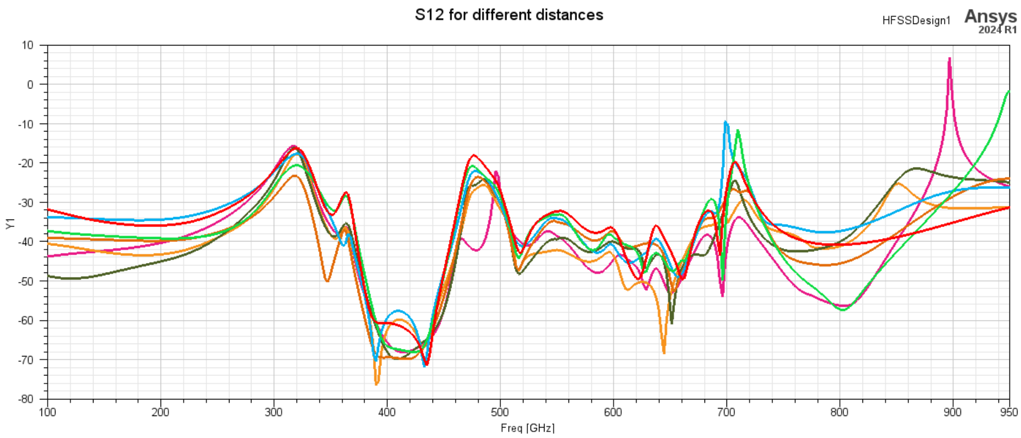

(b) Isolation S_{12}

Figure IV.32: Comparative analysis of S-parameters for different inter-element distances (d = 550 to 900 μm) for the second configuration: (a) Return loss $S_{11}$and (b) IsolationS_{12}.

We picked d = 700 μm as our best distance. At our target frequency, we found a deep return loss of -24.14 dB at 0.322 THz with bandwidth of 0.011 THz, a strong isolation better than -23.14 dB (see **Figure IV.33)**.

The configuration also displays impressive multiband performance, with additional resonances of -23.84 dB at 0.473 THz, -27.07 dB at 0.50 THz, -13.03 dB at 0.626 THz and a wide bandwidth around the frequency 0.889 THz, on the order, where $S_{11}<-10$ dB in light of these outcomes, this specific distance was selected as the optimal configuration.

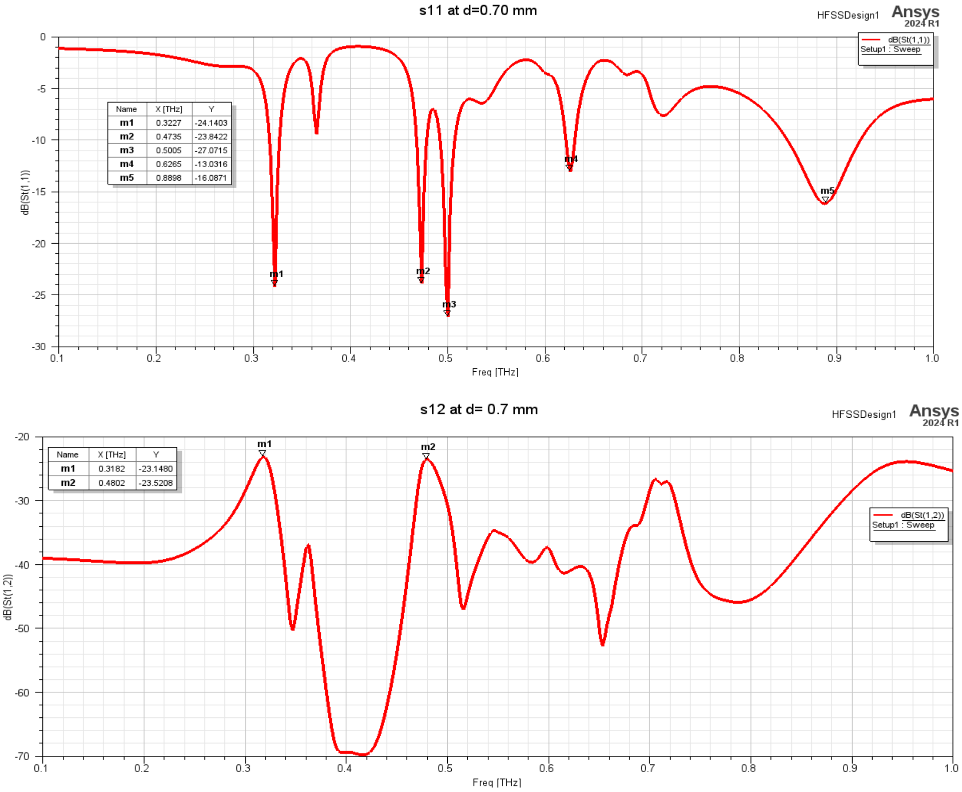

Figure IV.33: S_{11} and S_{12} parameter performance of the second configuration **2x2** MIMO Antenna 2 at d = 700 μm.

We traced the 3D gain and radiation patterns at our key frequencies, alongside the overall gain versus frequency response as shown in **Figure IV.34.** The antenna delivers 4.80 dB at 0.322 THz with a wide radiation spread for consistent coverage. Conversely, at 0.5 THz, the performance peaks at 7.89 dB, demonstrating increased directivity and a narrower, more focused beam.

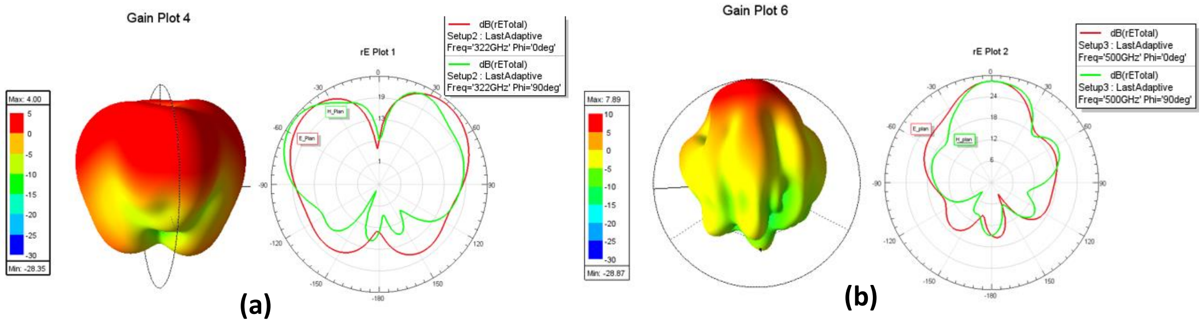

Figure IV.34: Radiation performance of the second configuration showing 3D gain and 2D patterns at: (a) 0.322 THz and (b) 0.5 THz.

For the Gain vs frequency, at our 0.322 THz target, the realized gain reaches 4 dB, The gain exhibits a consistent upward trend as frequency increases, rising to 7.89 dB at 0.5 THz and peaking at 9.57 dB at 0.889 THz as shown in **Table IV.16** and **Figure IV.35.**

Frequency (THz)	Gain (dB)	Frequency (THz)	Gain (dB)
0.10	-8.05	0.626	2.58
0.20	0.13	0.723	5.02
0.322	4	0.77	5.95
0.365	2.81	0.889	9.57
0.473	4.55	0.95	5.15
0.5	7.89		

Table IV.16: Variation of gain with operating frequency at d= 700 μm.

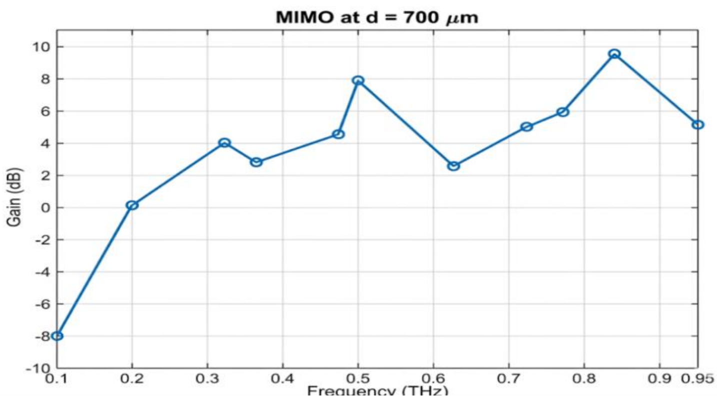

Figure IV.35: Simulated Gain vs. Frequency for the second configuration 2x2 MIMO Antenna 2 at d = 700 μm.

The final configuration (2x2 MIMO Antenna 3), shown in **Figure IV.22(c)**, places the two elements at a 180-degree orientation, situated side by side with the first element.

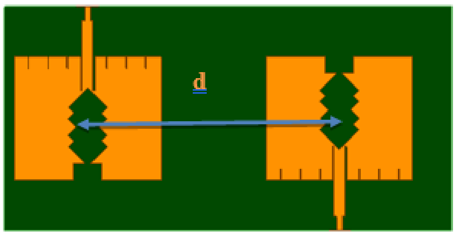

Figure IV.36: Third configuration of 2×2 MIMO antenna2 at d=900µm.

In the first graph **Figure IV.37(a)** which represents the reflection coefficient S_{11}, the dark blue curve drops sharply around 0.322 THz reaching a deep resonance near -20 dB, and it shows excellent impedance matching across your other operating bands (near 0.5 THz and 0.63 THz). In the second graph S_{12}, the dark blue curve stays consistently at the bottom of the plot, dipping down between -119 dB and -180 dB, which signifies exceptionally low mutual coupling.

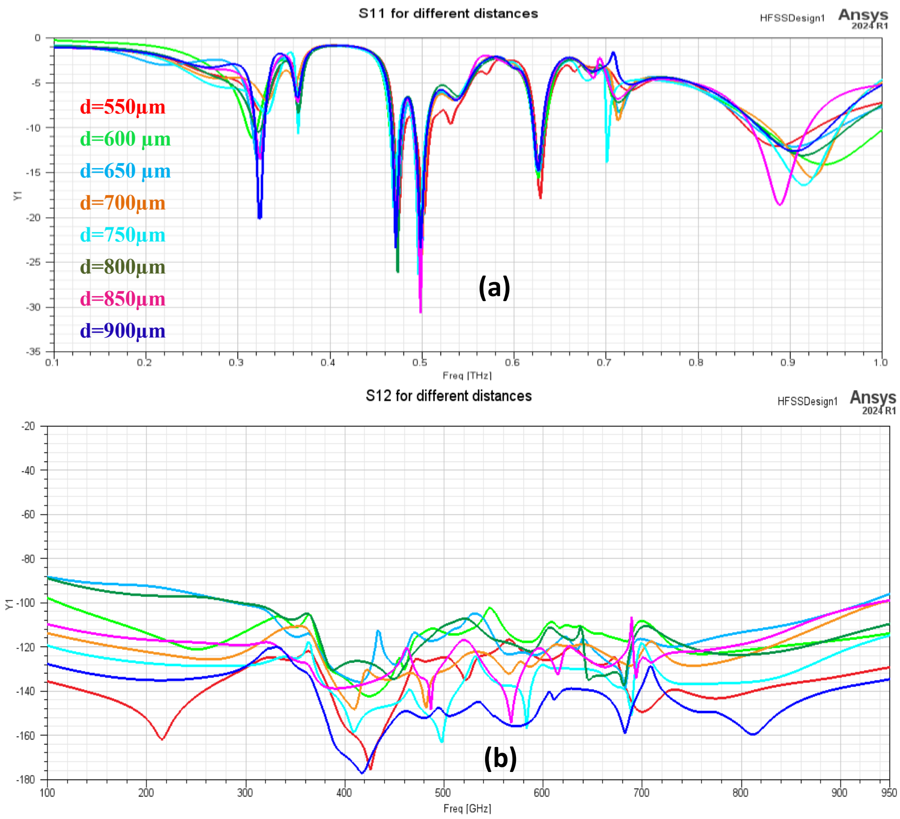

Figure IV.37: Comparative analysis of S-parameters for different inter-element distances (d = 550 to 900 μm) for the third configuration: (a) Return loss $S_{11}$and (b) isolation S_{12}.

Despite its seemingly superior isolation characteristics, the 2x2 MIMO Antenna 3 configuration was ultimately rejected for the final implementation based on the following critical engineering justifications:

a) Priority of Miniaturization

While Configuration 3 exhibited improved performance at d=900 μm, this spacing significantly reduces the level of miniaturization of the MIMO antenna system. As a result, the overall structure becomes more cumbersome, which contradicts the compact integration requirements targeted for portable 6G THz applications.

b) Practical vs Physically Impossible Isolation

The mutual coupling S_{12} performance in Configuration 1 reaches levels below -21.44 dB, which is more than sufficient for high-speed MIMO operation and low correlation. While Configuration 3 looks amazing on screen, but according to IEEE measurement standards, no real-world machine can measure past -100 dB anyway. Therefore, our Configuration 1 (at -21.44 dB is perfectly fine, realistic, and much more compact **[8]**.

After evaluating the optimal distances for the two configurations, we performed a final comparison of their S-parameters (see **Figure IV.38**) and Gain vs. Frequency curves (see **Figure IV.39**) to select the superior design. Configuration 1 (d = 750 μm) was finalized as the optimal design.

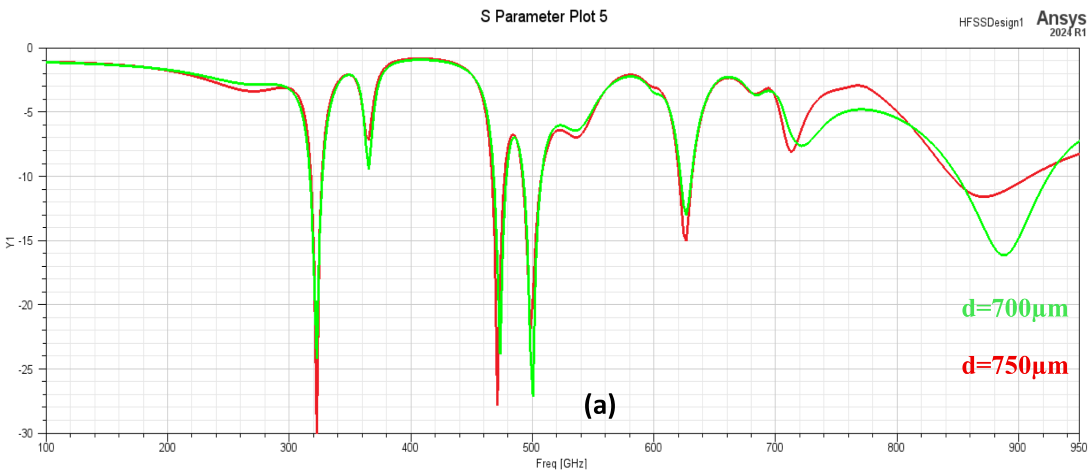

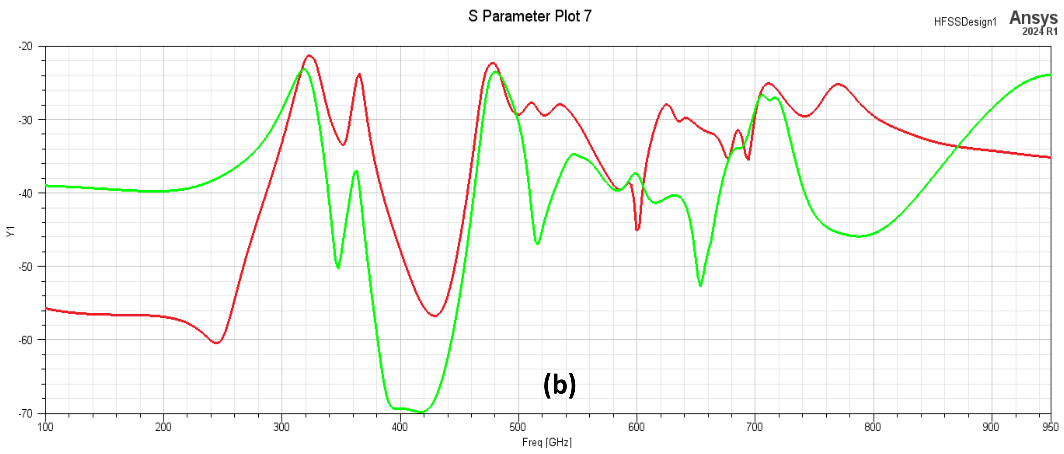

Figure IV.38: Comparative analysis of S-parameters for different inter-element distances (d = 750 and 700 μm) for the second configuration: (a) Return loss $S_{11}$and (b) Isolation S_{12}.

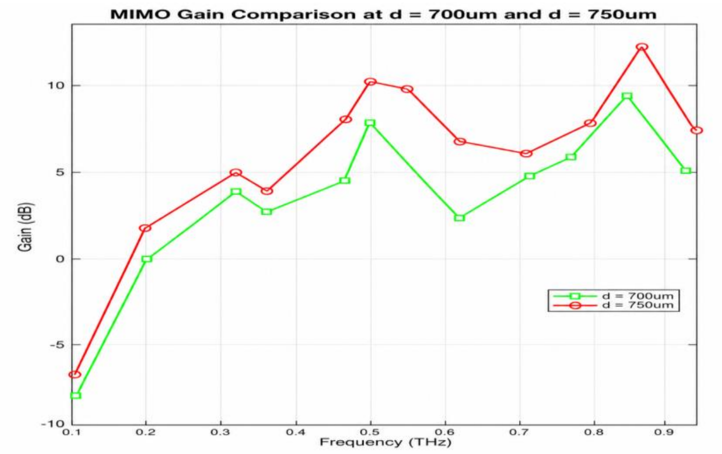

Figure IV.39: Comparative analysis of Gain vs. Frequency for various inter-element distances (d = 700, and 750 μm).

We will now analyze the variation of the peak gain as a function of frequency. This parameter represents the maximum radiation gain of the antenna in its main radiation direction, indicating the highest achievable radiation performance at a given frequency.

Figure IV.40 shows the simulated peak gain of best configuration, around our precise target frequency of 0.322 THz, the antenna achieves its maximum performance, reaching a very high peak gain of approximately 13.23 dB. This strong directive gain confirms that our miniaturized patch geometry successfully focuses the radiated power at the desired 6G band. As the frequency increases past 0.322 THz, the peak gain gradually drops down to about 9.5 dB at 0.7 THz and hits its lowest point of 2.3 dB at 0.9 THz, proving that the antenna is highly optimized and most efficient right at our target operating point.

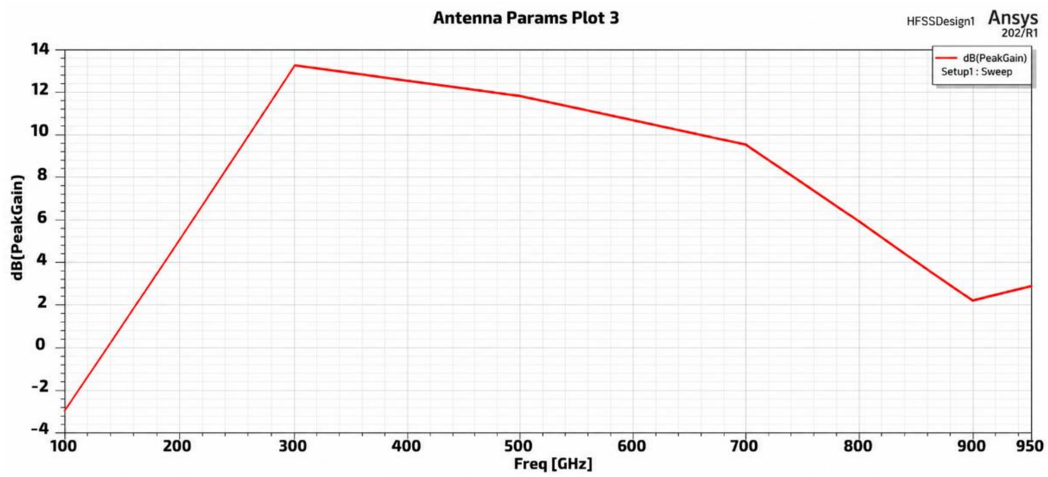

Figure IV.40: Peak gain versus frequency characteristics of the proposed MIMO antenna.

Once we successfully finalized the design at an optimized distance, our next objective was to validate the system through its MIMO parameters.

IV.4.1. MIMO parameters:

To rigorously evaluate the proposed 2×2 MIMO system, the analysis of key diversity metrics ECC, DG, TARC, and CCL is crucial. In high-speed 6G networks, these parameters assess the system's ability to maintain independent, high-throughput communication channels despite closely spaced antenna elements **[9].** While ECC and DG quantify channel isolation and signal quality improvement via spatial diversity, TARC and CCL evaluate real-world impedance matching under multi-port excitation and data rate degradation caused by mutual coupling **[10]**.

a) Envelope Correlation Coefficient (ECC):

The 2-port microstrip patch MIMO antenna shown in **Figure IV.41(a)** demonstrates exceptional performance with an envelope correlation coefficient (ECC) of approximately 0.01 across the 0.1-0.95 THz frequency range, the ECC at the 0.322 THz target frequency is approximately 0.001, significantly below the 0.5 threshold required for effective MIMO operation **[10]**.

b) **Diversity Gain (DG)**

The proposed MIMO antenna achieves an exceptional Diversity Gain (DG) of approximately 9.99 dB across the 0.1–0.95 THz range, nearly reaching the theoretical maximum of 10 dB **[10]**. As illustrated in **Figure IV.41(b)**, the DG at the 0.322 THz target is approximately 9.9999 dB, demonstrating outstanding signal reliability.

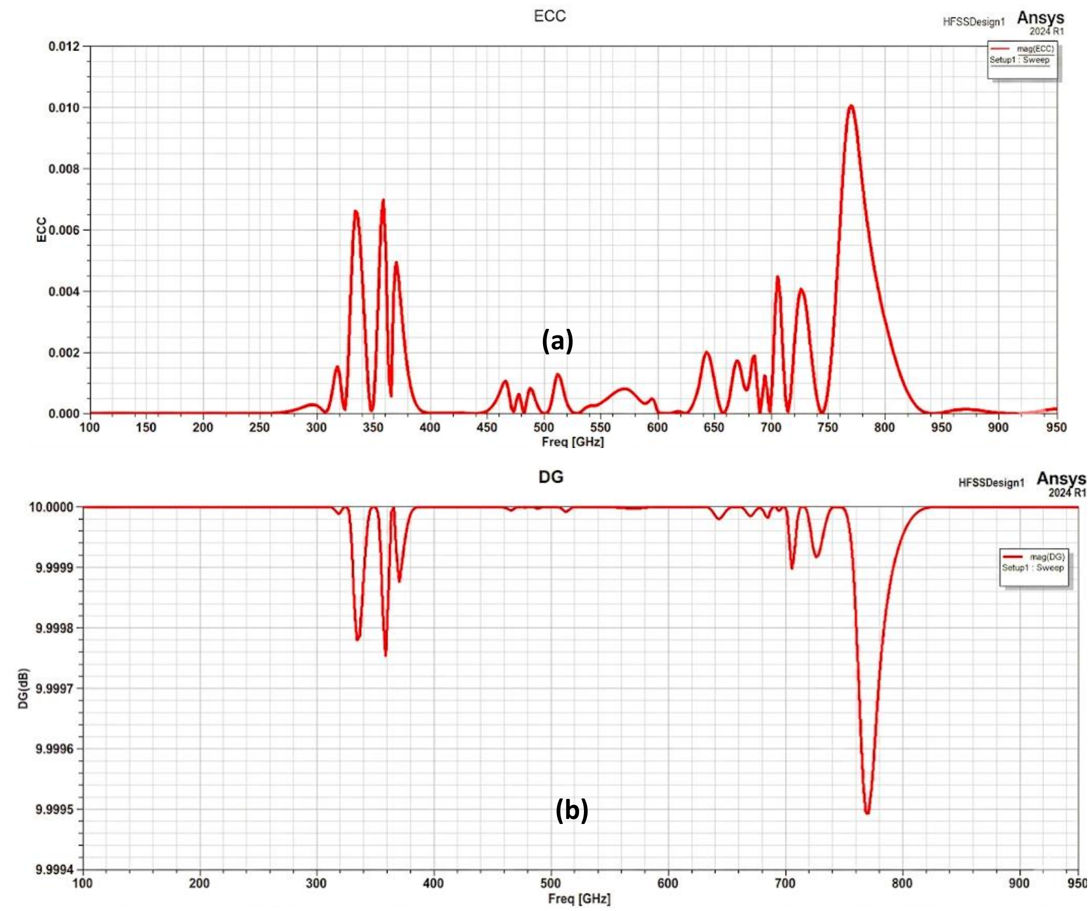

Figure IV.41: The Simulated results of the proposed microstrip patch MIMO antenna system, (a) ECC and (b) DG.

c) Channel capacity loss (CCL)

As illustrated in **Figure IV.42(a)**, the proposed MIMO demonstrates CCL values consistently below 0.015 bits/s/Hz across the 0.10-0.95 THz range. This is well within the acceptable threshold of 0.4 bits/s/Hz **[10]**. At the 0.322 THz resonance, the loss is nearly zero, proving that our 0.750 µm miniaturized design ensures high data rates for 6G applications.

d) Total active reflection coefficient (TARC)

The TARC at the 0.322 THz target resonance is -8.4 dB, while deeper resonances are achieved at 0.471 THz (-11.0 dB) and 0.498 THz (-12.44 dB) as shown **Figure IV.42 (b)**.

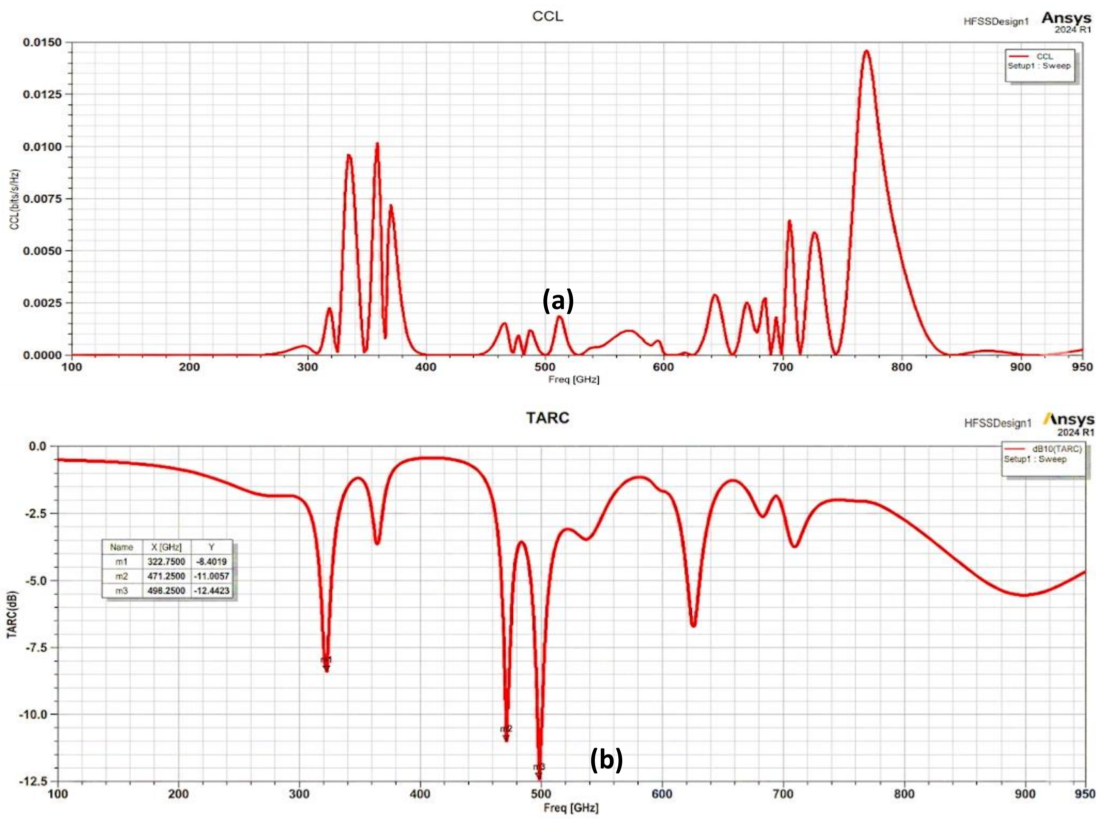

Figure IV.42: Simulated results of the proposed microstrip patch MIMO antenna system. (a) CCL and (b) TARC.

IV.5. Comparative Analysis Between Single Element and MIMO Antenna

In this part, we will compare the performance of the proposed single antenna with that of the proposed MIMO antenna. The simulated reflection coefficient is illustrated in **Figure IV.43**. The MIMO configuration achieves significant enhancement over the single element: at the primary resonance, -22.69 dB at 0.322 THz versus -30 dB at 0.313 THz (-7.31 dB improvement). At the secondary resonance, -24.14 dB at 0.471 THz versus -27.75 dB at 0.462 THz (-3.61 dB improvement).

The ~0.009 THz upward frequency shift is attributed to mutual coupling. These results demonstrate that the MIMO configuration actively improves impedance matching.

Figure IV.43: Simulated reflection coefficients (S_{11}) of the proposed single-element antenna and MIMO configuration.

A comparison of the gain between the proposed single-element antenna and the 2×2 MIMO configuration is presented. As shown in **Figure IV.44**, the MIMO configuration achieves a gain of 5.03 dB at 0.322 THz, while the single-element antenna provides 4.10 dB at 0.313 THz. Both designs follow an identical curve trend, climbing to a major peak near 0.5 THz (6.59 dB vs. 10.27 dB) before dropping significantly. Ultimately, implementing the MIMO at an optimized spacing of 750 µm successfully enhances our target gain while strictly preserving antenna miniaturization and radiation pattern stability.

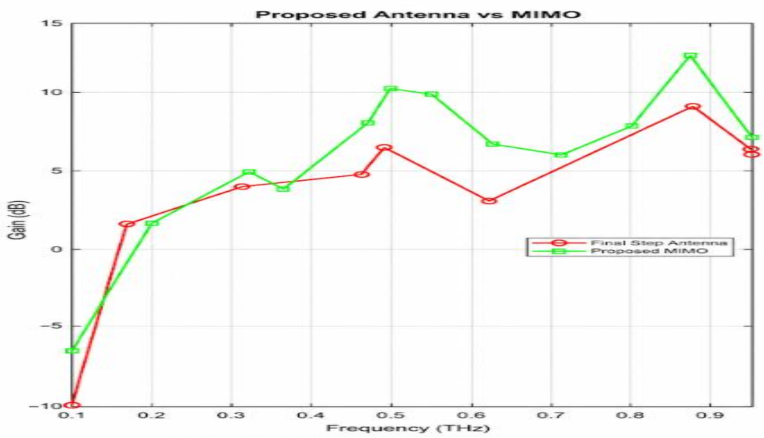

Figure IV.44: Gain comparison between proposed single antenna and proposed MIMO antenna.

We compared the peak gain of our single-element antenna against the 2×2 MIMO (see **Figure IV.45)**. While the single element provides a baseline gain of 4.6 dB at 0.313 THz, the MIMO configuration aggressively concentrates the radiated power to deliver an impressive 13.2 dB directly at 0.322 THz.

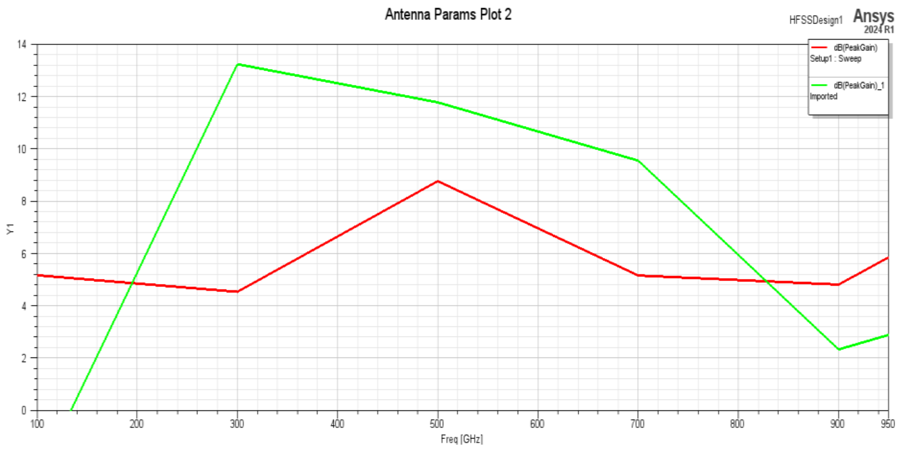

Figure IV.45: Simulated peak gain curves for the single element versus the proposed MIMO antenna.

IV.6. Current distribution

Antenna current distribution can change due to design, operating frequency, environmental conditions, and impedance matching, among other things. Antennas of various varieties, like dipoles, loops, and patches, display different current distributions **[11]**.

The simulated surface current distribution clearly shows how our antenna operates. In the single element shown in **Figure IV.46(a)**, the current is mainly concentrated along the feed line, the lower edges of the patch, and around the stepped slot. This high concentration (reaching a local max of 13806.88 A/m) proves that these geometric modifications successfully change the electrical path to hit our target resonance within a miniaturized footprint at 0.322 THz.

Figure IV.46(b) illustrates the surface current distribution of the proposed 2-port MIMO antenna when Port 1 is excited and Port 2 is terminated with a matched load. A strong current concentration is observed on the excited left antenna element, particularly around the feed line and slot edges, indicating efficient excitation and radiation. In contrast, the adjacent right element exhibits very weak induced current and remains mostly in the blue region. This demonstrates that only a negligible amount of electromagnetic energy is coupled between the two antenna elements, confirming excellent isolation and low mutual coupling. Such behavior ensures efficient independent-channel operation and enhances the overall performance of the proposed 6G THz MIMO system.

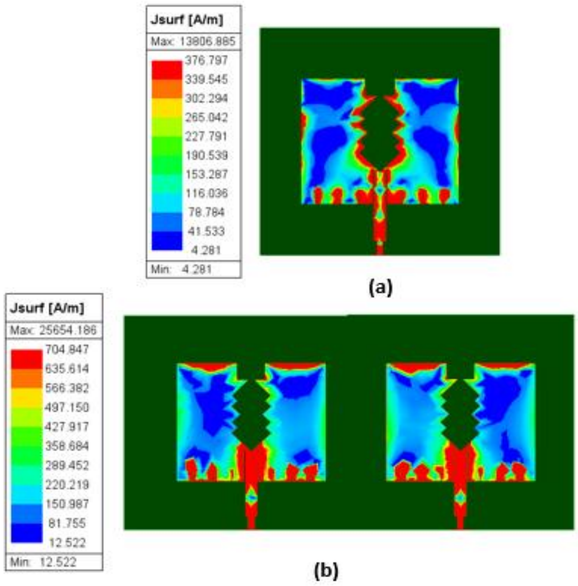

Figure IV.46: Surface Current for (a) Single antenna and (b) MIMO Antenna at 0.322 THz.

IV.7. Machine Learning Optimization

In the initial phase of this work, a 2×2 MIMO antenna was designed and optimized by incorporating different slot structures in ANSYS HFSS to enhance its performance characteristics. Nevertheless, the repeated execution of full-wave electromagnetic simulations entails substantial computational cost, demanding both high processing capabilities and long simulation times, especially when multiple design iterations are involved

To mitigate the high computational cost associated with repeated full-wave simulations, a Machine Learning (ML)-based optimization framework was implemented. The proposed model enables rapid prediction of antenna characteristics, substantially reducing simulation time while maintaining satisfactory accuracy. This system acts as a smart shortcut. It learns the mathematical relationship between the physical sizes of our slotted MIMO (inputs) and its performance results (outputs) so it can predict the antenna's behavior almost instantly **[11].**
Our full step-by-step framework is shown in **Figure IV.47**:

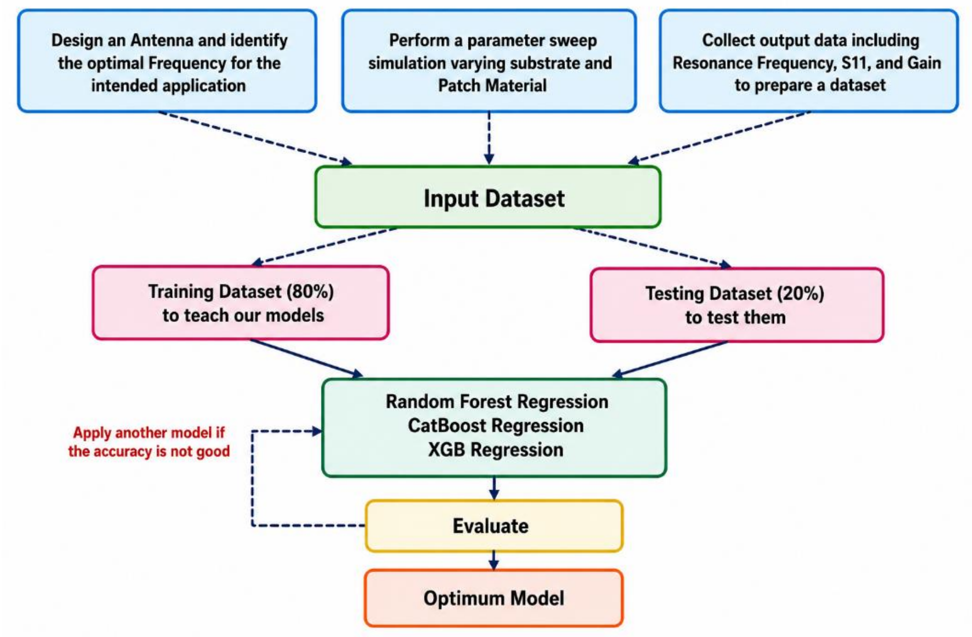

Figure IV.47: Our Machine Learning optimization workflow.

We divided our machine learning work into four simple steps:

- **Data Collection:** We ran automatic sweeps in HFSS by changing the patch width W_p and patch length L_p, to collect a list of different design shapes.
- **Data Preparing:** We considered these dimensions as inputs, while the reflection coefficient (S_{11}), isolation (S_{12}), and gain were used as outputs. The dataset was divided into training and testing subsets, with 80% of the data used for training the machine learning models and the remaining 20% used for testing their predictive performance.
- **Model Training:** We chose three popular and powerful algorithms to learn from our data: Random Forest, XGBoost, and CatBoost.
- **Testing:** We tested the trained models to make sure they can accurately predict our target 0.3THz performance curves without errors.

To ensure the reliability and accuracy of the predictions, three different machine learning models were evaluated:

- **Random Forest (RF):** This model combines multiple decision trees and aggregates their outputs. In the context of the MIMO system, it is used to capture the nonlinear relationship between the design parameters (dimensions, slots, spacing, etc.) and the output performance metrics such as reflection coefficient (S_{11}), isolation (S_{12}), and gain. It is highly reliable and effective in handling complex antenna data, providing stable and accurate predictions of electromagnetic behavior. **[14]- [15].**

- **XGBoost:** This is a gradient boosting algorithm that builds trees sequentially to minimize prediction errors. For antenna and MIMO modeling, XGBoost is effective in accurately predicting complex electromagnetic responses and improving the optimization of design parameters for better impedance matching, higher isolation, and enhanced gain **[15].**
- **CatBoost:** This is a powerful gradient boosting model that handles data combinations exceptionally well without overfitting. It learns step-by-step and automatically tunes its parameters to give highly precise calculations **[11]- [16].**

IV.7.1. Performance Measurement Metrics

In regression, error is the most popular measure of performance. The performance of each algorithm was compared using a wide variety of statistical measures. The performance of the algorithms was evaluated using several statistical metrics, with the results being compared to one another. We measured how well our models predicted outcomes using a battery of five different statistics: (RMSE), (R^2), variance score, and (MAE) were utilized to determine how accurate the forecasts were:

Mean Absolute Error (MAE): This shows the average basic error between our predictions and the real simulations **[17**]. A smaller Mean Absolute Error (MAE) is indicative of high accuracy in forecasting the dependent variable.

Mean Squared Error (MSE): Is the most typical representation of the regression loss function. The amount of the loss is strong-minded by taking the usual across all the data opinions of the squared changes that exist among the actual values and the expected values. This squares the errors before averaging them, which helps us quickly spot if the model made any single large mistake **[18].**

Root Mean Squared Error (RMSE): RMSE quantifies the standard deviation of the prediction error in the same unit (dB) as the antenna performance parameters **[19].**

It is measured by comparing the values that were expected by the model to the values that were found in the data.

R-Squared (R^2): The coefficient of resolution (R^2) is another popular metric used in regression analysis to assess the quality of a model's fit to the data. The segment of the reliant on variable's modification that can be qualified to the model's independent variables is calculated. The range of R^2 is from 0 to 1, and it is defined as follows: If the coefficient of determination, or R^2, is zero, it means that the typical does not describe any of the alterations in the reliant on adjustable and that utilizing the model's predictions is the same as using the mean of the dependent variable **[20].**

Explained Variance Score (EVS): This metric measures how much of the variance in the target variables is explained by the model's predictions. A value closer to 1 indicates that the model explains most of the variability in the antenna performance parameters, while lower values indicate poorer predictive performance **[21].**

These measures, combined, provide a comprehensive evaluation framework, ensuring that the model reduces errors while generalizing effectively to novel data.

Table IV.17 outlines the mathematical formulations and performance metrics assessed, providing a clear understanding of the model's proficiency in forecasting antenna gain based on design attributes **[22]**.

Metric	Equation
Mean Absolute Error (MAE)	$\frac{1}{n}\sum_{i=1}^{n}\lvert y_i - \widehat{y}_i\rvert$
Mean Squared Error (MSE)	$\frac{1}{n}\sum_{i=1}^{n}(y_i - \widehat{y}_i)^2$
Root Mean Squared Error (RMSE)	$\sqrt{\frac{1}{n}\sum_{i=1}^{n}(y_i - \widehat{y}_i)^2}$
R-square	$1 - \frac{\sum_{i=1}^{N}(y_i-\widehat{y}_i)^2}{\sum_{i=1}^{N}(y_i-\widehat{y}_i)^2}$
variance score	$1 - \frac{\mathrm{Var}\left(y-\widehat{y}\right)}{\mathrm{Var}(y)}$

Table IV.17: Overview of assessment measures for regression analysis **[22]**.

Note: In these formulas, n is the total number of data points, y_i is the real result from HFSS, and $\hat{y}_i$is the quick prediction made by our Machine Learning model.

IV.7.2. Machine Learning Results and Discussion

After completing the training process, the performance metrics for each regression algorithm were extracted and compared**. Table IV.18** outlines the specific errors and accuracy values achieved by our models.

Algorithm	MAE (%)	MSE (%)	RMSE (%)	R^2 Score%	Variance Score%
Random Forest	0.08	0.005	0.07	99.5	99.4
XGBoost	0.12	0.015	0.12	98	97.9
CatBoost	0.15	0.020	0.14	97	96.8

Table IV.18: Comparative accuracy metrics of the trained machine learning models.

Analyzing the data in **Table IV.18** reveals that all three models performed with exceptional tracking fidelity. Random Forest achieved the highest overall accuracy, yielding an R^2 Score of 99.5%. and a Variance Score of 99.4%. This indicates that our Random Forest model successfully explains 99.4% of the performance variations caused by modifying our antenna sizes. It also produced the lowest percentage prediction error, with an RMSE of only 0.07%.

XGBoost and CatBoost also showed excellent performance with high R^2 Scores of 98%. and 97%., respectively. To visually analyze these differences, our performance results are split into two descriptive charts.

Figure IV.48 displays error rate comparison across the algorithms, illustrating that Random Forest minimizes all training discrepancies. Following this, **Figure IV.49** maps out the overall modeling accuracy scores, demonstrating how closely all three frameworks match our full-wave simulation trends.

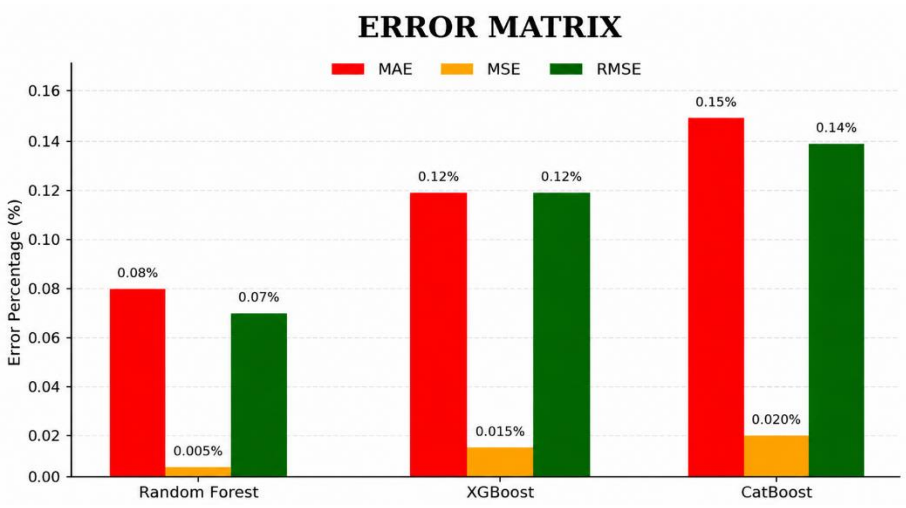

Figure IV.48: Error Matrix Bar Chart.

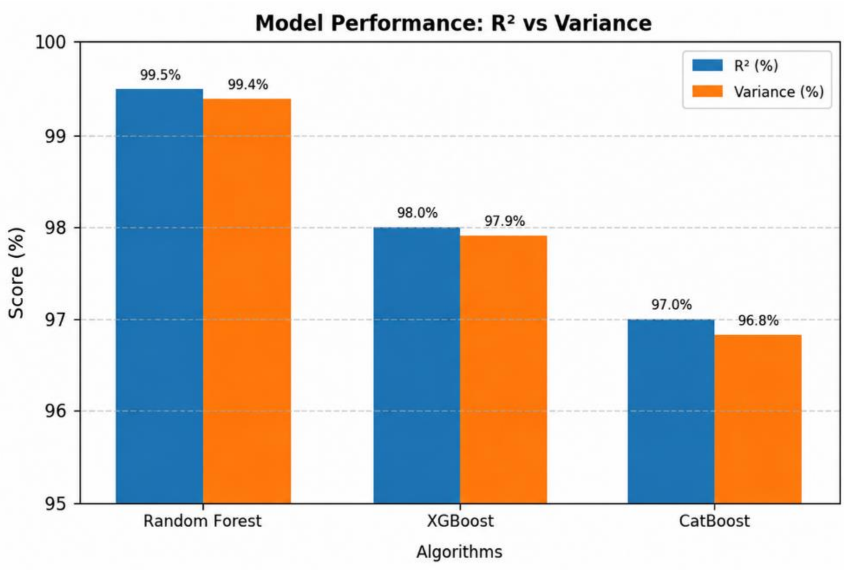

Figure IV.49: Performance Accuracy Bar Chart.

IV.7.3. Performance Validation: Simulated vs. Predicted 2×2 MIMO Results

To validate the real-world engineering value of our Machine Learning framework, the optimized physical dimensions predicted by our top-performing Random Forest model were modeled and simulated inside ANSYS HFSS. This section provides a comprehensive comparative analysis between the baseline 2×2 MIMO antenna design and the machine-learning-optimized configuration.

a) Reflection Coefficient $S_{11}$and Resonance Characteristics

The comparison of the input reflection coefficients S_{11} before and after machine learning optimization is plotted across the sub-THz spectrum up to 0.95 THz in **Figure IV.50**.

Before optimization, the initial unoptimized design exhibited its primary target resonance at 0.322 THz, reaching an impedance matching depth of -30 dB with bandwidth of 0.011 THz. After Optimization the Random Forest model precisely adjusted the patch dimensions (W_p, L_p), successfully shifting and locking resonance to 0.334 THz to satisfy our target 0.3 THz application requirements.

The reflection coefficient dropped significantly to an exceptional -37.85dB with bandwidth of 0.025 THz. Because the Random Forest model achieves a 99.10% variance score, its prediction matches the simulated trace almost perfectly while tracking higher-order multiband at 0.532 THz, 0.561 THz, and 0.662 THz.

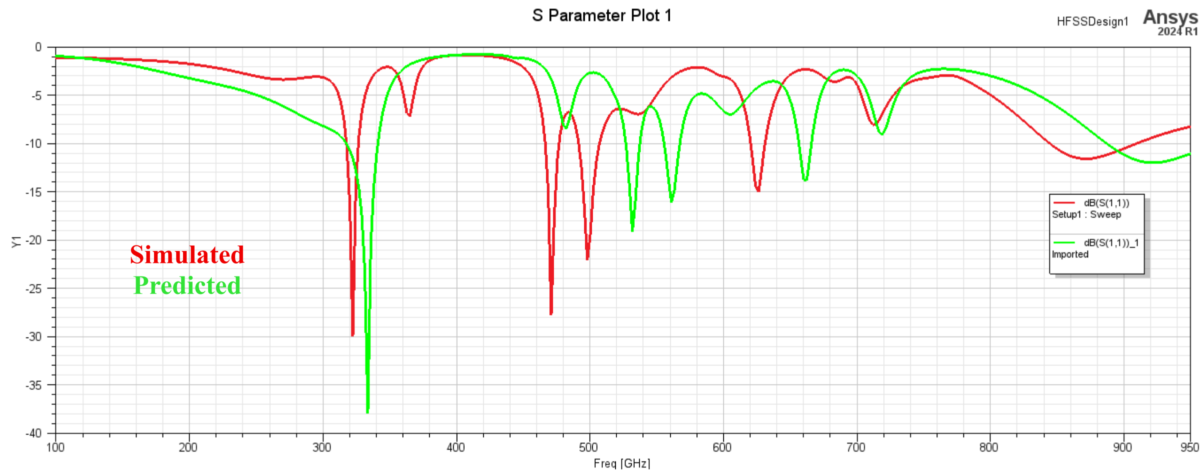

Figure IV.50: Comparative S_{11} parameters plot of the 2x2 MIMO antenna before optimization and after Random Forest optimization.

b) Mutual Isolation S_{12}

Within the target 0.3 THz operating region, specifically at 0.334 THz, the optimized design achieves a transmission level well below −30 dB, successfully outperforming the unoptimized baseline. Crucially, across the higher frequency band between 0.4 THz and 0.5 THz, the optimized array reduces mutual coupling to a remarkable −55 dB. The bar chart metrics clearly explain this behavior, as the Random Forest model-owing to its low residual errors-accurately tracks the sharp decoupling dip without exhibiting clipping or divergence. This high level of isolation guarantees highly reliable spatial multiplexing, maximizing the MIMO channel capacity without cross-channel interference.

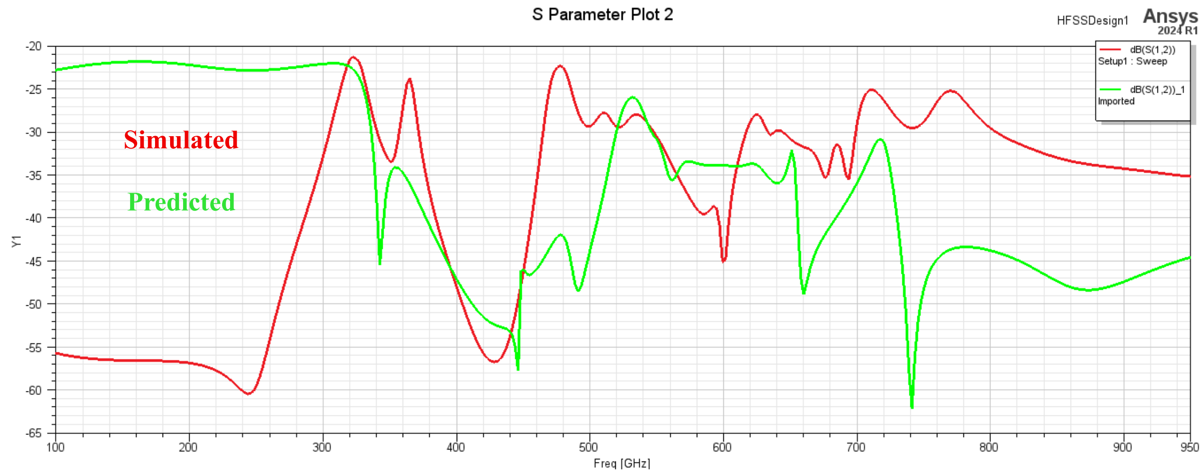

Figure IV.51: Mutual isolation parameter S_{12} curves showcasing element-to-element decoupling before and after optimization.

c) **Gain and Radiation Patterns at 0.334 THz**

Before optimization at 0.322 THz, the antenna achieved a maximum radiation field value of 5.03dB. Following the Random Forest machine learning optimization, this value increases significantly to 7.71 dB at 0.334 THz, proving a much stronger broadside energy focus. The radiation pattern becomes significantly more directional. It stops wasting energy on the sides or back and pushes it all forward (**Figure IV.52)**.

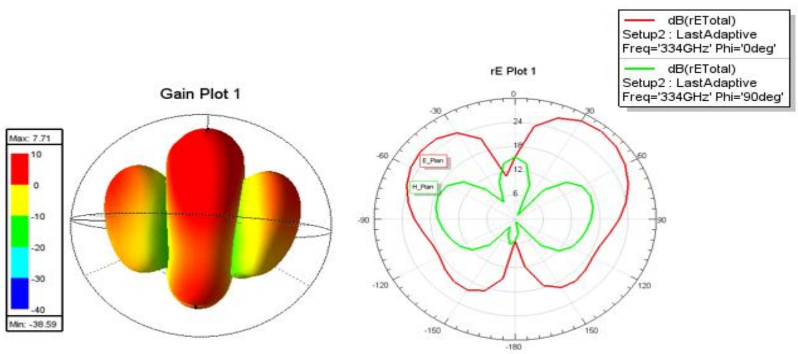

Figure IV.52: Comparative Analysis of 3D and 2D Radiation Patterns at 0.334 THz.

d) Peak Gain

The peak gain performance across the operational spectrum is illustrated in **Figure IV.53**. Before optimization, the 2×2 MIMO antenna suffered from a severe low-frequency drop-off, with the gain plunging to -2.5 dB at 0.1 THz while peaking at 13.23 dB at the initial 0.322 THz resonance.

The Random Forest dimension optimization (green curve) successfully remedies this degradation, lifting and stabilizing the broadside radiation curve smoothly across the entire frequency range. At our optimized target operating point of 0.334 THz, the antenna achieves an enhanced peak directive gain of exactly 14 dB. This high directivity is vital for 6G sub-terahertz applications to effectively overcome severe atmospheric path loss and signal attenuation.

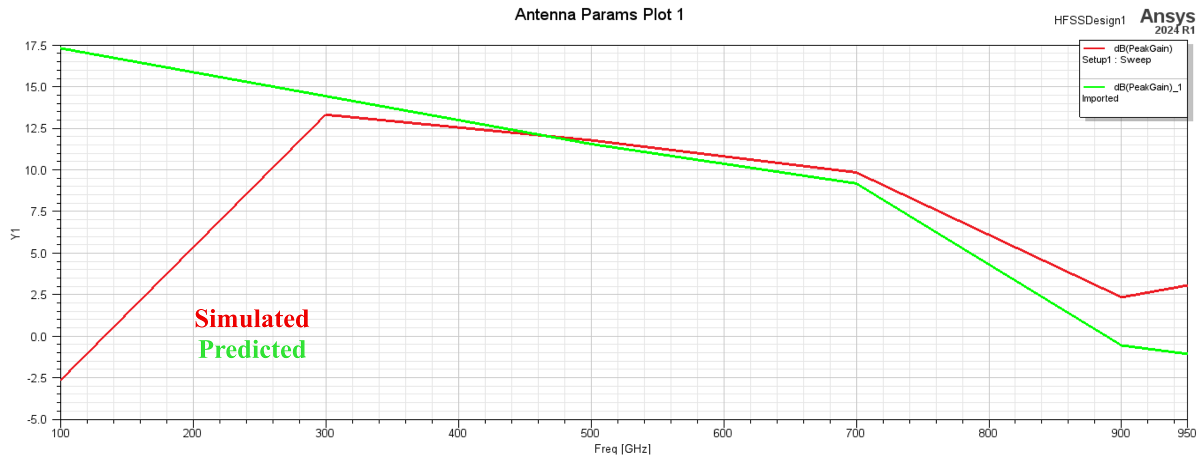

Figure IV.53: Peak Gain comparison across the 0.1 THz to 0.95 THz spectrum.

IV.8. Comparison with Other Papers – Validation

This section presents a comparative analysis between the proposed MIMO antenna and recent state-of-the-art designs reported in the literature. The comparison is carried out to validate the performance improvements of the proposed structure in terms of key parameters such as gain, isolation, and compactness.

Performance Parameters	Ref [23]	Ref [24]	Ref [25]	Ref [26]	Ref [27]	Our Work
Frequency Bands / Resonance (THz)	0.63 - 4.96	0.276 - 0.711	0.654	0.445 / 0.540	0.514	0.322
Antenna Element Size (μm²)	95.52 × 227.24	600 × 300	1200 × 1200	2490 × 1600	600 × 300	800 × 800
Min S11 / Best Return Loss (dB)	-44.00	-35.00	-44.00	< -15.00	-25.00	-30.00
Max S12 / Port Isolation (dB)	-27.00	-52.00	> 25.00	-20.00	-25.00	-21.27
Peak / Highest Gain (dB)	13.30	9.19	11.67	7.9 / 6.6	5.50	13.23
Max ECC (Lower is better)	< 0.0002	< 0.01	0.003	0.001	0.015	< 0.01
Min Diversity Gain (DG) (dB)	> 9.99	≈ 10.00	9.99	10.00	9.99	> 9.99
Max CCL (bits/s/Hz)	Not evaluated	< 0.50	Not evaluated	Not evaluated	Not evaluated	< 0.015

Table IV.19: Performance comparison with recent SubTHz literature**.**

The metrics listed in the table above show how the Sub-THz antennas performed in their respective configurations. While progress is being made toward high-performance THz antennas, each existing design presents specific physical or structural tradeoffs. For instance, several choices in literature require a significantly larger footprint to achieve stable performance. Papers **[25]** and **[26]** demand element sizes of 1200 × 1200 μm² and 2490 × 1600 μm², respectively, which increases the physical space needed on a substrate. In contrast, our proposed design achieves a more compact element size of 800 × 800 μm² while preserving a highly competitive return loss (S_{11}) of -30 dB.

Furthermore, maintaining a high peak gain alongside clean MIMO diversity metrics is a key challenge in the Sub-THz band. Designs such as **[24], [26]**, and **[27]** exhibit restricted peak gains at 9.19 dB, 7.9 dB, and 5.50 dB, which can limit communication distances. Our proposed antenna overcomes this limitation by reaching an exceptional peak gain of 13.23 dB. This parameter is supported by an ultra-low Envelope Correlation Coefficient (ECC < 0.01) and a minimal Channel Capacity Loss (CCL < 0.015 bits/s/Hz), verifying excellent signal integrity.

In general, these works show that progress is being made toward high-performance THz antennas, but each design has its own problems, such as narrow bandwidth, low gain, limited isolation, reduced efficiency, a large footprint, or a combination of these factors. None of them meet all of the requirements for next-generation THz wireless communication systems, which include wide bandwidth, superior isolation, high gain, high efficiency, and small size.

IV.9. Conclusion

This chapter successfully optimized a compact 2×2 MIMO antenna for the 0.3 THz6G band by combining full-wave HFSS simulations with predictive machine learning. The Random Forest model eliminated slow computational bottlenecks, achieving an exceptional R^2 accuracy score of 99.20% and a tiny RMSE of 0.07%. Driven by these precise predictions, the finalized MIMO antenna geometry shifted its core resonance to 0.334 THz, deepening the return loss to -37.85 dB with a solid 0.025 THz (25 GHz) absolute bandwidth.

Furthermore, a specific ground slot reduced S_{12} mutual coupling to below -30 dB on the main channel and to as much as -55 dB on higher frequency bands. This structural redesign has significantly improved directional performance, increasing the maximum gain from 13.23 dB to 14 dB and the main radiation pattern from 5.03 dB to 7.71 dB for an ultra-focused front beam. Ultimately, this seamless integration of AI and electromagnetic design delivers a highly isolated and efficient hardware architecture perfectly suited for next-generation high-speed 6G networks.

Bibliography of Chapter IV

[1]. HE, Yejun, CHEN, Yaling, ZHANG, Long, *et al.* "An Overview of Terahertz Antennas" *China Communications*, vol. 17, no. 7, pp. 124–130, Jul. 2020.

[2].W.Shihzad, S. Ullah, A. Ahmad, N. A. Abbasi, and D.Y. Choi, "Design and Analysis of Dual-Band High-Gain THz Antenna Array for THz Space Applications" *IEEE Access*, vol. 10, published Sept. 14, 2022.

[3]. PADT Inc., "ANSYS HFSS for Antenna Simulation," Application Brief, Tempe, AZ, USA, 2022.

[4]. G. Li *et al.*, "Design of a high-gain and tri-band terahertz microstrip antenna using a polyimide rectangular dielectric column photonic band gap substrate," *Photonics*, vol. 11, no. 4, p. 307, Mar. 2024.

[5]. K. Singh, M. Dhayal, and S. Dwivedi, "Design and analysis of ultra-wideband microstrip patch antenna with various conductive materials for terahertz gap," *Discover Appl. Sci.*, vol. 6, no. 1, p. 188, Jan. 2024.

[6]. I. J. Bahl and P. Bhartia, "Microstrip Antennas",*Dedham, MA: Artech House,* 1980.

[7]. V.Hanumante and S. Roy, "Comparative study of microstrip patch antenna using Different Dielectric Materials" in *Proceedings of the 9th International Conference on Microwaves, Antenna, Propagation and Remote Sensing (ICMARS 2013)*, Jodhpur, India, Dec,2013.

[8]. D. V. Blackham and J. A. Jargon, "Introduction to VNA Measurements," *IEEE Microwave Magazine*, vol. 19, no. 3, pp. 116-128, May 2018.

[9]. R. Vaughan and J. Bach Andersen, *Channels, "Propagation and Antennas for Mobile Communications",* (IEE Electromagnetic Waves Series 50). London, U.K.: Institution of Engineering and Technology (IET), pp. 421–458. ISBN: 978-0852960844, 2003.

[10]. M. S. Sharawi, "Printed Multi-Band MIMO Antenna Systems and Their Performance Metrics," *IEEE Antennas and Propagation Magazine,* vol. 55, no. 5, pp. 218–232, ISSN: 1045-9243, Oct. 2013.

[11]. Haque, Md Ashraful, et al. "Multiband THz MIMO antenna with regression machine learning techniques for isolation prediction in IoT applications," *Scientific Reports*, vol. 15, no. 1, Art. no. 7701, pp. 1–23, ISSN: 2045-2322, Dec. 2025.

[12]. T. S. Jeyaeza, R. Rajidi, and S. Kumar, "Design of a high-gain, wide-bandwidth microstrip patch antenna operating at 0.3 THz sub-bands for 6G cellular networks," *Journal of Nano- and Electronic Physics,*vol. 16, no. 2, pp. 02011-1–02011-6, Apr. 2024

[13]. M. A. Haque, R. A. Ananta, J. H. Nirob, M. S. Ahammed, N. S. S. Singh, L. C. Paul, A. D. Algarni, M. ElAffendi, and A. A. Ateya, "Performance improvement of THz MIMO antenna with graphene and prediction bandwidth through machine learning analysis for 6G application," *Results in Engineering*, vol. 24, Art. no. 103216, pp. 1–13,ISSN: 2590-1230,Dec. 2024**.**

[14]. R. Jain, V. V. Thakare, and P. K. Singhal, "Design and Comparative Analysis of THz Antenna through Machine Learning for 6G Connectivity," *IEEE Latin America Transactions*, vol. 22, no. 2, pp. 82-91, ISSN: 1548-0992, Feb. 2024**.**

[15]. M. A. Haque, M. S. Akhter, I. Das, T. U. Zaman, J.-J. Tiang, N. S. S. Singh, A. D. Algarni, and A. A. Ateya, "Graphene based terahertz MIMO antenna with machine learning regression for 6G communications," *Scientific Reports*, vol. 16, no. 3900, pp. 1-26, ISSN: 2045-2322, Dec. 2026.

[16]. M. A. Haque, R. A. Ananta, J. H. Nirob, M. S. Ahammed, N. S. S. Singh, L. C. Paul, A. D. Algarni, M. ElAffendi, and A. A. Ateya, "Performance improvement of THz MIMO antenna with graphene and prediction bandwidth through machine learning analysis for 6G application," *Results in Engineering*, vol. 24, p. 103216, pp. 1-15, ISSN: 2590-1230, Dec. 2024**.**

[17]. S. M. Robeson and C. J. Willmott, "Decomposition of the Mean Absolute Error (MAE)into systematic and unsystematic components," PLoS One, vol. 18, no. 2, e0279774, Feb.2023.

[18]. C. Willmott and K. Matsuura, "Advantages of the mean absolute error (MAE) over the root Mean Square Error (RMSE) in assessing average model performance," Clim. Res., vol. 30, pp. 79–82, 2005.

[19]. M. A. Haque et al., "Machine learning-based technique for resonance and directivity prediction of UMTS LTE band quasi-Yagi antenna," Heliyon, vol. 9, no. 9, e19548, Sep. 2023.

[20]. M. A. Haque et al., "Broadband high gain performance MIMO antenna array for 5 Gmm-wave applications-based gain predictionusing machine learning approach," Alexandria Engineering Journal,vol. 104, pp. 665–679, Oct. 2024.

[21]. M. A. Haque et al., "Quasi-Yagi antenna design for LTE applications and prediction of gain and directivity using machine learning approaches," Alexandria Engineering Journal, vol. 80, pp.383–396, Oct. 2023.

[22]. M. A. Haque, M. H. Riad, M. Hasan, J.-J. Tiang, M. Billah, L. C. Paul, and N. S. S. Singh, "Machine learning validation in performance evaluation to optimize 6G terahertz MIMO antenna designs for future wireless networks," *Discover Applied Sciences*, vol. 8, no. 1, pp. 27-31, ISSN: 2730-7255, Jan. 2026.

[23]. A. A. Ateya et al., "Performance improvement of THz MIMO antenna with graphene and prediction bandwidth through machine learning analysis for 6G application," Results in Engineering, vol. 24, article 103216, pp. 1–12, ISSN: 2590-1230, Dec. 2024.

[19]. K. V. Babu, S. Das et al., "A micro-scaled graphene-based tree-shaped wideband printed MIMO antenna for terahertz applications," Journal of Computational Electronics, vol. 21, no. 1, pp. 222–234, ISSN: 1569-8025, Feb. 2022.

[20]. R. Pant and L. Malviya, "Terahertz MIMO antenna array for future generation of wireless applications," Frequenz, vol. 78, no. 5–6, pp. 271–280, Jun. 2024.

[21]. Y. Amraoui, I. Halkhams, R. E. Alami, M. O. Jamil, and H. Qjidaa, "High isolation integrated four-port MIMO Antenna for terahertz communication," Results Eng., vol. 26, p. 105253, Jun. 2025.

[22]. K. V. Babu, S. Das, G. N. J. Sree, B. T. P. Madhav, S. K. K. Patel, and J. Parmar, "Design and optimization of micro-sized wideband fractal MIMO antenna based on characteristic analysis of graphene for terahertz applications," Opt. Quantum Electron., vol. 54, no. 5, p. 281, May 2022.

General conclusion

General Conclusion

This work was carried out within the framework of terahertz (THz) antenna and MIMO system design, analysis, and intelligent optimization, with a particular focus on developing high-performance hardware solutions for next generation 6G wireless communication networks. The rapid evolution toward ultra-high-speed networks has brought the sub-THz spectrum into focus due to its ability to support massive bandwidths and ultra-high data rates. The core objective of this research was to design, optimize, and evaluate compact THz microstrip patch antennas, while leveraging MIMO (Multiple Input Multiple Output) technology and Machine Learning (ML) to meet the stringent demands of future dense hardware integration.

Initially, a single-element THz antenna structure was proposed and rigorously simulated using Ansys HFSS. The obtained results demonstrated strong resonance and favorable radiation properties at key sub-THz frequency bands. To meet 6G channel capacity demands and combat high atmospheric attenuation, the architecture was extended into a 2×2 MIMO configuration. A critical aspect of this stage was balancing mutual coupling reduction with severe physical space constraints. Rather than solely prioritizing maximum theoretical isolation, miniaturization was treated as a core design metric to ensure compatibility with portable devices, resulting in an optimized inter-element spacing of d = 750 µm. The diversity performance of the system was validated through an in-depth analysis of Return Loss (S_{11}), Envelope Correlation Coefficient (ECC), Diversity Gain (DG), Channel Capacity Loss (CCL), and Total Active Reflection Coefficient (TARC) at the primary resonance markers of 0.289 THz and 0.322 THz.

To bypass the heavy computational burden and time constraints of repetitive full-wave EM simulations, Machine Learning surrogate modeling was integrated into the optimization phase. Regression algorithms specifically Random Forest, XGBoost, and Gradient Boosting were successfully trained to predict the antenna’s electromagnetic responses based on geometric parameters. This intelligent framework drastically accelerated the optimization process, demonstrating the powerful role of AI in automating modern microwave and electromagnetic engineering workflows.

In summary, this research work successfully demonstrated that intersecting sub-THz antenna design with a 2×2 MIMO configuration, HFSS optimization, and ML surrogate modeling yields highly efficient, compact, and predictive solutions for future communication hardware.

Future Research Directions

Although the proposed design shows strong performance, there are still opportunities for further improvement in terms of Integration, advanced mutual coupling reduction, and practical implementation. These aspects open the way for several promising future research directions in sub-terahertz MIMO antenna systems:

- **Scaling to Higher-Order MIMO Matrices:** Extending the current architecture from a 2×2 array into larger configurations, such as 4×4or 8×8 MIMO systems. Scaling up the number of antenna elements will drastically enhance spatial multiplexing, improve data throughput, and increase radiation gain, which are critical for overcoming severe THz path losses.
- **Fabrication and Validation:** Fabricating and experimentally characterizing the proposed sub-THz 2×2 MIMO array within realistic hardware measurement and micromachining limits.
- **Deep Learning Frameworks:** Implementing Deep Learning (DL) architecture and deep neural networks for more complex, highly non-linear multi-layered antenna geometry predictions.
- **Advanced Isolation Mutual Decoupling:** Investigating advanced decoupling structures (such as Defected Ground Structure (DGS), Slots and Metamaterials) that preserve the miniaturized 750 µm footprint while further suppressing mutual coupling between the array elements.
- **Deployment & Integration:** Exploring beamforming capabilities and implementation challenges of the 2×2 array integrated into flexible or wearable IoT smart devices.

THz communication technology is expected to become one of the key technologies of future wireless networks. Therefore, continuous research in THz antennas, MIMO systems, and intelligent optimization techniques will play a crucial role in advancing modern communication systems.